A Surface Water–Energy Balance model for urban Land Surface Temperature and Surface Urban Heat Island analysis: the cases of Milano and Amsterdam.

A Thesis Submitted in Partial Fullfilment of the Requirements for the Degree of Doctor of Philosophy in **Sustainable Development and Climate Change**

XXXVIII cycle

PhD candidate: **Sonia Morgese**

Supervisor: Prof. **Daniele Bocchiola**, Politecnico di Milano

Co-Supervisor: Prof. **Miriam Coenders-Gerrits**, Technische Universiteit Delft

Chair of the Doctoral Program: Prof. **Mario Martina** , IUSS Pavia

Academic Year 2025–2026

Contents

Acknowledgment

I would like to express my sincere gratitude to all the people who made the achievement of this milestone possible.

First thanks go to my supervisor, with whom I had already worked during my Master's thesis, for validating my methodological approach and for involving me from the very beginning in the research activities of Climate-LAB, a multi-disciplinary laboratory at Politecnico di Milano dedicated to the study of climate change impacts on hydrology across different environments, including pastures, avalanches, glaciers, and urban heat islands.

I would also like to thank my colleagues at Climate-LAB, with whom I shared scientific results and discussions, as well as field missions, hostels, conferences, and travels that enriched both my professional and personal experience. I am equally grateful to the PhD students and researchers from other universities with whom we collaborated in synergy throughout these three years.

Special thanks go to my co-supervisor for hosting me at TU Delft and for initiating a collaboration from scratch, for introducing me to a new research group, and for his continuous support and guidance during my visit.

Finally, I would like to thank the IUSS Pavia and all those involved in making this doctoral program possible. Communication was not always easy and challenges inevitably arose, as is to be expected in such an ambitious project. I am grateful to have been part of a national PhD program, which gave me the opportunity to engage with diverse research communities and scholars from different backgrounds and doctoral paths, all united by the same overarching goal—the one that motivated my decision to pursue a PhD: to study **Climate Change** and contribute to the promotion of **Sustainable Development**.

Abstract

This PhD thesis develops a physically based framework to quantify Land Surface Temperature (LST) in urban environments and to investigate the Surface Urban Heat Island Intensity ($SUHII$) at intra-urban scale. The analysis focuses on spatial contrasts within cities, comparing different urban and peri-urban typologies, including historical centers, residential and industrial areas, and surrounding rural environments.

The proposed approach relies on a physically based representation of the coupled surface water and energy balance at the soil–atmosphere interface, hereafter referred to as the Surface Water Energy Balance ($SWEB$) framework. The model explicitly links soil moisture dynamics to latent and sensible heat fluxes, providing a physically consistent representation of LST variability under different land cover and climatic conditions.

Surface Urban Heat Islands (SUHI) are areas where LST are higher than in surrounding rural regions. The difference in LST between paved and blue/green area is quantified by the Surface Urban Heat Island Intensity ($SUHII$). This occurs because paved surfaces absorb more energy (due to lower albedo) and have reduced evapotranspiration, as they cannot retain water like vegetated areas or water bodies.

The $SWEB$ model was calibrated and validated in two pilot cities characterized by different climatic and urban features: Milano and Amsterdam. For Milano, simulations were conducted at daily scale on a 500 m $\times$ 500 m grid, covering the period 2010–2022 and including climate projections up to 2100 under multiple scenarios. Short-term (2040–2050), mid-term (2065–2075), and long-term (2090–2100) horizons were considered. For Amsterdam, the analysis focused on the historical city center enclosed by the Singelgracht canal system, using a finer spatial resolution (100 m $\times$ 100 m) and an hourly temporal scale for the period 2020–2024. In both case studies, the relationship between LST and urban blue–green infrastructure was investigated to assess the cooling potential of nature-based solutions.

Meteorological forcing was derived from automatic weather stations, while soil properties and land-cover information were obtained by integrating satellite data with local urban planning datasets. In the Milano domain, vegetation was represented through a Vegetated Fraction (VF), whereas in Amsterdam land cover was described using built-up, green, and water fractions (B_f, G_f, W_f). Satellite-derived LST was used for model calibration, employing MODIS data for Milano and Landsat 8 imagery for Amsterdam. In the Amsterdam case study, additional calibration was performed using radiometric LST estimates derived from flux-tower observations located in the city center.

Milano During summer, average LST values reach 35.37 °C, with mean differences of approximately 3.7 °C between paved and green surfaces and peaks exceeding 4.5 °C. Model results confirm the cooling role of urban vegetation, showing that an increase in green cover of 10% ($VF = +0.1$) corresponds to a mean LST reduction of about 0.23 °C. Summers characterized by an increased frequency of heatwave events, such as 2015 and 2022, exhibit anomalously high surface temperatures, with mean summer LST values approximately 4 °C higher than the multi-year average. These findings highlight the sensitivity of urban thermal conditions to both land-cover composition and extreme climatic events.

Amsterdam Flux-tower measurements indicate an average LST of approximately 20 °C, with daytime values (08:00–19:00) reaching 23.99 °C and nighttime values averaging 16.97 °C. During daytime, built-up areas exhibit higher surface temperatures ($LST_b = 24.56$ °C) compared to green areas ($LST_g = 22.83$ °C) and water bodies ($LST_w = 20.34$ °C). The resulting mean $SUHII$ is +1.72 °C relative to green areas and +4.21 °C relative to water bodies, while the built-up effect reaches approximately +3 °C. Although stronger LST contrasts are observed between urban and rural environments, substantial thermal variability is also detected within the dense urban fabric, emphasizing the relevance of blue–green infrastructure for local heat mitigation.

Future Projections Climate projections indicate a substantial modification of urban thermal conditions throughout the XXI century. For Milano, under the best-case scenario (SSP1–2.6), summer LST is projected to decrease by up to −2.66 °C by 2100, while $SUHII$ remains relatively high (+1.55 °C). Conversely, under the worst-case scenario (SSP5–8.5), LST is projected to increase by +3.98 °C, accompanied by a reduced $SUHII$ (+0.51 °C). This apparent attenuation of $SUHII$ arises from prolonged drought and heatwave conditions, which

limit soil moisture availability and reduce the cooling efficiency of vegetated surfaces. These results underline the central role of water availability in regulating urban thermal dynamics. Consistently, the Amsterdam case study shows that urban water bodies, characterized by LST values approximately 4 °C lower than surrounding built-up areas, significantly contribute to local cooling by reducing sensible heat fluxes.

Overall, this thesis provides a quantitative and physically based framework for assessing urban LST and $SUHII$, offering a transferable tool to support urban planning, climate adaptation, and mitigation strategies under current and future climate conditions.

Keywords: Surface Urban Heat Island; Land Surface Temperature; Water–Energy Balance; Urban Climate; Mitigation; Future Projections; Green Areas; Water Bodies; Urban Planning.

Abstract in Italiano

Questa tesi di dottorato sviluppa un framework fisicamente basato per quantificare le temperature superficiali (Land Surface Temperature, LST) in ambienti urbani e per analizzare l'Intensità dell'Isola di Calore Urbana Superficiale (Surface Urban Heat Island Intensity, $SUHII$) alla scala intra-urbana. L'analisi si concentra sui contrasti spaziali all'interno delle città, confrontando diverse tipologie urbane e peri-urbane, inclusi centri storici, aree residenziali e industriali, e gli ambienti rurali circostanti.

L'approccio proposto si basa su una rappresentazione fisicamente consistente del bilancio idrico ed energetico accoppiato, applicato alla superficie, all'interfaccia suolo - atmosfera, di seguito denominato modello Surface Water Energy Balance ($SWEB$). Il modello collega esplicitamente la dinamica dell'umidità del suolo ai flussi di calore latente e sensibile, fornendo una rappresentazione fisicamente coerente della variabilità della LST in differenti condizioni di copertura del suolo e climatiche.

Il modello $SWEB$ è stato calibrato e validato in due città pilota caratterizzate da condizioni climatiche e assetti urbani differenti: Milano e Amsterdam. Per Milano, le simulazioni sono state condotte a scala giornaliera su una griglia di 500 m $\times$ 500 m, coprendo il periodo 2010–2022 e includendo proiezioni climatiche fino al 2100 sotto diversi scenari. Sono stati considerati orizzonti di breve termine (2040–2050), medio termine (2065–2075) e lungo termine (2090–2100). Per Amsterdam, l'analisi si è concentrata sul centro storico racchiuso dal sistema dei canali della Singelgracht, utilizzando una risoluzione spaziale più fine (100 m $\times$ 100 m) e una scala temporale oraria per il periodo estati 2020–2024. In entrambi i casi studio, è stata analizzata la relazione tra LST e infrastrutture blu–verdi urbane al fine di valutare il potenziale di raffrescamento delle NBS.

Le forzanti meteorologiche sono state derivate da stazioni meteorologiche automatiche, mentre le proprietà del suolo e le informazioni sulla copertura del suolo sono state ottenute integrando dati satellitari con dataset locali di pianificazione urbana. Nel bacino di Milano, la vegetazione è stata rappresentata

tramite il parametro Vegetated Fraction (VF), mentre ad Amsterdam la copertura del suolo è stata descritta utilizzando le frazioni di superficie edificata, verde ed idrica (B_f, G_f, W_f). Le LST derivate da satellite sono state utilizzate per la calibrazione del modello, impiegando dati MODIS per Milano e dati Landsat 8 per Amsterdam. Nel caso di studio di Amsterdam, è stata inoltre effettuata una calibrazione aggiuntiva utilizzando stime radiometriche di LST derivate da osservazioni della flux tower localizzata nel centro città.

Milano Durante l'estate, i valori medi di LST raggiungono 35.37 °C, con differenze medie di circa 3.7 °C tra superfici pavimentate e aree verdi e picchi superiori a 4.5 °C. I risultati del modello confermano il ruolo mitigante della vegetazione urbana, mostrando che un incremento del 10% della copertura verde ($VF = +0.1$) corrisponde a una riduzione media della LST di circa 0.23 °C. Estati caratterizzate da una maggiore frequenza di eventi di ondata di calore, come il 2015 e il 2022, presentano temperature superficiali anomalmente elevate, con valori medi estivi di LST circa 4 °C superiori alla media estati 2010-2022. Questi risultati evidenziano la sensibilità delle condizioni termiche urbane sia alla composizione della copertura del suolo sia agli eventi climatici estremi.

Amsterdam Le misure della flux tower indicano un valore medio di LST di circa 20 °C, con valori diurni (08:00–19:00) pari a 23.99 °C e valori notturni medi di 16.97 °C. Durante il periodo diurno, le aree edificate mostrano temperature superficiali più elevate ($LST_b = 24.56$ °C) rispetto alle aree verdi ($LST_g = 22.83$ °C) e ai corpi idrici ($LST_w = 20.34$ °C). L'intensità media della $SUHII$ risulta pari a +1.72 °C rispetto alle aree verdi e a +4.21 °C rispetto ai corpi idrici, mentre l'effetto dell'edificato raggiunge valori prossimi a +3 °C. Sebbene i contrasti di LST siano più marcati tra ambienti urbani e rurali, una notevole variabilità termica è rilevata anche all'interno del tessuto urbano denso, sottolineando l'importanza delle infrastrutture blu–verdi per la mitigazione locale del calore.

Proiezioni future Le proiezioni climatiche indicano una significativa modifica delle condizioni termiche urbane nel corso del XXI secolo. Per Milano, nel best case scenario (SSP1–2.6), le LST estive sono previste diminuire fino a 2.66 °C entro il 2100, mentre la $SUHII$ rimane relativamente elevata (+1.55 °C). Al contrario, nel worst case scenario (SSP5–8.5), le LST sono previste aumentare di 3.98 °C, con aggiunta una riduzione della $SUHII$ (+0.51 °C). Questa apparente attenuazione della $SUHII$ è attribuibile a condizioni prolungate di siccità e ondate di calore, che limitano la disponibilità di umidità del suolo e riducono

l'efficienza di raffrescamento delle superfici vegetate. Tali risultati evidenziano il ruolo centrale della disponibilità idrica nella regolazione della dinamica termica urbana. Coerentemente, l'esperienza del caso studio di Amsterdam mostra che i corpi idrici urbani, caratterizzati da valori di LST circa 4 °C inferiori rispetto alle aree edificate circostanti, contribuiscono in modo significativo al raffrescamento locale riducendo i flussi di calore sensibile.

Nel complesso, questa tesi fornisce un modello quantitativo e fisicamente basato per la valutazione delle LST urbane e della $SUHII$, offrendo uno strumento easy-to-use a supporto della pianificazione urbana e delle strategie di adattamento e mitigazione climatica in condizioni climatiche attuali e future.

Parole chiave: Isola di Calore Urbana Superficiale; Land Surface Temperature; Bilancio Water-Energy; Clima Urbano; Mitigazione; Proiezioni Future; Aree Verdi; Corpi Idrici; Pianificazione Urbana.

Chapter 1

Introduction, Motivation and State of art

1.1 Introduction

Cities host more than 50% of world population, and they contribute to up to 85% of world energy consumption [**1.1**]. The IPCC Sixth Assessment Report (AR6) acknowledges that urbanization, also linked to rising incomes and consumption, challenges climate change resilience. Due to rapid global urbanization, average temperatures in cities have risen, more than in the outskirts. The temperature difference between urban and rural areas is commonly referred to the Urban Heat Island (UHI) phenomenon. The foundations of the UHI topic can be traced back to Howard [**1.2**], a pioneer of urban climate, who first documented a difference in air temperature of approximately 1.58 °C between urban and rural areas of London in the early XIX century, in the aftermath of industrialization. The formal conceptualization of the UHI phenomenon was later introduced by Balchin and Pye [**1.3**], who recognized that most major cities are affected by this effect. Traditionally, UHI has been defined in terms of near-surface air temperature (T_a), typically measured at about 2 m above ground level. However, the advent of satellite-based thermal remote sensing in the second half of the XX century enabled a fundamental shift in the observation of urban thermal environments. In particular, thermal infrared (TIR) sensors (approximately 10–12 μm) made it possible to retrieve Land Surface Temperature (LST), representing the radiometric temperature of the Earth's surface, including soil, vegetation, water, and built-up materials. Unlike air temperature, LST directly reflects the thermal response of different surface materials to radiative forcing, capturing spatial heterogeneity at much finer scales. This distinction led Rao [**1.4**] to identify systematic dif-

ferences in LST between urban and rural areas and to introduce the concept of the Surface Urban Heat Island (SUHI). The SUHI framework represents a major advancement over the traditional UHI approach, as it allows for a more detailed and spatially explicit characterization of urban thermal patterns. While UHI (based on T_a) provides information on atmospheric conditions relevant to human thermal comfort, SUHI (based on LST) captures the physical properties and energy balance of urban surfaces, making it particularly suitable for analyzing land cover effects, urban morphology, and mitigation strategies such as nature-based solutions. SUHI describes the spatial manifestation of enhanced surface temperatures associated with urbanization. Rao [**1.4**] reported the first satellite-based observations of the SUHI phenomenon in the eastern United States. Since then, continuous advancements in remote sensing and spatial analysis have significantly increased both the availability and the accuracy of LST data, making SUHI studies a dominant component of contemporary urban climate research. Primary causes of SUHI stem from land cover differences between urban, and rural areas [**1.5**]. The magnitude of SUHI phenomenon is quantified through the Surface Urban Heat Island Intensity ($SUHII$) [**1.6**]. $SUHII$ is defined as the difference in LST between fully urbanized surfaces (i.e., areas characterized by 100% built-up cover, including impervious surfaces and infrastructure) and cooler urban components, such as vegetated areas (e.g., parks and gardens) and water bodies. Thus, to detect SUHI, it's necessary to examine the LST. In the most critical urban zones, featuring high shares of paved surfaces, and large anthropogenic heat release, higher LST values are observed, when compared against greener areas.

Urban surfaces exhibit heterogeneous structures that strongly influence both hydrological and energy fluxes. From a hydrological perspective, impervious surfaces limit water infiltration and storage, enhancing runoff and reducing water availability for evaporative cooling, with effects depending on precipitation intensity and duration [**1.7**]. In terms of energy balance, net radiation is partitioned into sensible and latent heat fluxes. Sensible heat (H) flux directly increases air temperature through heat transfer, whereas latent heat (LE) flux is associated with phase changes of water (e.g., evaporation ET) and does not directly raise temperature. Urban areas, characterized by low albedo and limited moisture availability, tend to favor sensible heat flux, leading to higher surface temperatures, while latent heat flux is reduced.

These processes, water and energy budgets, are closely coupled, as soil moisture availability controls evaporation and regulates the partitioning of energy

fluxes.

Overheating of cities can have significant impacts, e.g. with increased mortality [**1.8**, **1.9**], deterioration of living environment, and further increased energy consumption [**1.10**, **1.11**]. Studies at urban scale both targeting European and Asian cities, and based on the use of *LST* satellite images, confirmed significant positive correlation among *LST* and impervious surface density [**1.12**, **1.13**, **1.14**]. Therefore, scientists search for strategies to mitigate SUHI effectively [**1.15**], e.g. by increasing green areas [**1.16**, **1.17**], by reducing anthropogenic heat [**1.18**, **1.19**, **1.20**], and by using highly reflective (high albedo), lowly warming materials [**1.21**, **1.22**].

Green areas play a key role in dampening the effects of SUHI, as given by their natural cooling effect [**1.23**, **1.24**]. From a practical stand point, urban design henceforth needs adequate consideration of impending climate change, otherwise potentially making the environment thermally worse [**1.25**]. Biodiversity has also a positive role on perceived soothing properties, and self-reported benefits from urban and peri-urban green areas [**1.26**], even improving mental health [**1.27**]. Urban green and blue spaces are widely recognized as effective strategies for mitigating urban heat stress and enhancing the outdoor thermal environment [**1.17**, **1.28**, **1.29**]. These spaces are characterized by land surfaces dominated by vegetation and/or water bodies. Examples of urban green spaces include small neighborhood parks, large city parks, urban forests, gardens, street trees, as well as green roofs and facades [**1.30**]. Their cooling effects are primarily driven by two mechanisms: evapotranspiration and shading. Evapotranspiration refers to the process through which water is transported within plants and subsequently evaporates from their aerial parts, dissipating radiative energy as latent heat and thereby maintaining cooler foliage [**1.31**, **1.32**]. In suburban areas, where built-up is sparser, there is an important contribution of vegetation evapotranspiration [**1.33**]. Shading, on the other hand, reduces air temperature by intercepting solar radiation—trees act as natural barriers that absorb and reflect radiant energy [**1.34**]. In the case of blue spaces, the dominant cooling mechanism, particularly for static water bodies, is evaporation [**1.35**]. For dynamic water bodies, such as rivers and canals, thermal behavior is additionally shaped by flow characteristics as well as meteorological conditions [**1.36**]. For instance, some studies [**1.37**] demonstrated that an urban river in the United Kingdom was capable of reducing air temperature by up to 1 °C.

During heat wave (HW) days, the energy budget is unbalanced toward sensible heat, causing a greater increase in *LST* and in perceived air temperatures. The

majority of the net radiation converts itself into sensible heat [**1.38**], resulting in a significant increase in LST during HW period.

The projections of climate variables in the future is also crucial to develop effective strategies for climate change reduction on the society, and ecosystems. Global climate models are important tools to mimic present climate patterns, as well as for predicting future climate change under scenarios of societal development, and greenhouse gasses [**1.39**]. Recently, IPCC delivered the results of the CMIP6 [**1.40**], providing multi-model climate projections based on alternative greenhouses emissions' scenarios.

1.2 Motivation

The aim of this research is to develop a model for the assessment of Land Surface Temperature (LST). The model is characterized by the following features: it is physically based and semi-distributed; it relies on the representation of water and energy budgets; it adopts a spatial resolution suitable for capturing heterogeneity in urban properties; and it estimates LST as a function of climatic variables and urban configuration. Understanding LST patterns allows to evaluate how different land covers may mitigate soil heating under the same climate conditions. The final aim is to assess the mitigation effects of blue and green infrastructures in urban contexts, focusing on two major European cities, Milano and Amsterdam, and to explore future projections of LST and $SUHII$ under changing climate scenarios.

An increasing number of cities, including Milano and Amsterdam, are adopting guidelines for the implementation of Nature-Based Solutions (NBS), with the goal of fostering sustainability, enhancing environmental quality, and reducing the prevalence of impervious surfaces and gray infrastructures, which have expanded significantly as a result of rapid urbanization. This study does not seek to design new NBS or propose landscape-oriented solutions. Instead, it aims to evaluate, from an engineering perspective, the role of urban greenery and its capacity to mitigate the increase in LST driven by ongoing global warming. The proposed methodology relies on a combined water–energy model, which is particularly suited to providing a deeper understanding of complex energy-driven phenomena such as the Surface Urban Heat Island (SUHI). In this regard, Water–Energy Nexus approaches are increasingly being recognized and applied.

Based on the objectives of this thesis, the following research questions have been formulated to guide the investigation. They aim to explore the magnitude

and drivers of the urban heat island phenomenon in Milano and Amsterdam, as well as its potential implications for policy and planning:

- How pronounced is the $SUHII$ effect in Milan and Amsterdam?
- To what extent does land use contribute to the development of its own SUHI?
- How do the two cities compare in terms of SUHI intensity and dynamics?
- What insights can climate projections provide for understanding future $SUHI$ scenarios?
- Which data and outputs can offer meaningful information for stakeholders and policymakers?

Starting from these research questions, the thesis addresses them through a structured workflow of research activities:

- An in-depth investigation of urban climate processes is conducted by adopting a water–energy nexus approach, aimed at capturing the interactions between hydrological and thermal dynamics.
- Within this framework, a Surface Water–Energy Balance ($SWEB$) model is developed, with a specific focus on LST and related indicators, including $SUHII$.
- A long-term analysis is performed for two major European cities. Milano (2010–2022) is used as a pilot case to test and refine the model framework, which is subsequently applied to Amsterdam (2020–2024), accounting for city-specific characteristics.
- A comparative analysis between Milano and Amsterdam is carried out to assess the role of green spaces—and, in the case of Amsterdam, blue–green infrastructures—in mitigating increases in LST.
- For the Milano case study, future climate scenarios are also developed to evaluate the projected impacts of global climate change, using multiple General Circulation Models (GCMs) and alternative Shared Socioeconomic Pathways (SSPs) as defined by the IPCC.
- Finally, planning-relevant insights are derived by quantifying the mitigation potential of urban blue–green infrastructures under current and future climate conditions.

1.3 State of art

The study of Urban Heat Islands (UHI) dates back to the early nineteenth century, when Howard [**1.2**] first observed higher air temperatures in urban areas compared to rural surroundings. Traditionally, UHI has been defined using near-surface air temperature (T_a). A major advancement occurred in the 1970s with the introduction of satellite remote sensing, which enabled the estimation of LST. Rao [**1.4**] first identified urban–rural differences in LST, defining the SUHI. While UHI describes atmospheric temperature differences, SUHI captures the spatial variability of surface temperatures and the underlying physical processes, providing a more detailed representation of urban thermal patterns. These distinctions are crucial for urban climate studies: UHI impacts human comfort and health, while SUHI drives surface mitigation strategies such as greenery and reflective materials. Main differences are reported in Table 1.1.

	UHI	**SUHI**
Measure	Air temperature (T_a)	Land Surface Temperature (LST)
Reference height	2 m a.g.l. (Station height)	0 m a.g.l. (Surface elevation [1])
Scale	Local (km)	Large (satellite pixel)
Main causes	Anthropogenic heat release	Land cover properties
Intensity	Higher at night	Higher during daytime

Table 1.1. Comparison between Urban Heat Island (UHI) and Surface Urban Heat Island (SUHI).

There is still some conceptual ambiguity in the literature, as several studies associate UHI directly with LST. For consistency, this PhD dissertation will refer exclusively to SUHI, since LST is the target variable. Therefore, SUHI will be the only term used throughout the thesis paper. Despite extensive progress in modeling and monitoring the urban thermal environment, several limitation persist in understanding and predicting Surface Urban Heat Island dynamics, especially under future scenarios.

Regarding SUHI, several modeling techniques are commonly employed, such as: remote sensing analysis, machine learning models, global climate models, and local physically based models.

1 – Remote sensing analysis. Satellite-based techniques have been extensively used to capture LST [**1.41**, **1.42**]. Remote sensing methods are particularly useful for capturing spatially continuous information over an entire urban area,

[1] Surface elevation refers to the height of the surface intercepted by the satellite signal from above. In most cases, this corresponds to the terrain level, but in other situations it may instead capture the top of the canopy or the roof level of buildings.

allowing the detection of LST patterns rather than relying on single-point measurements. However, these methods may suffer from limited temporal resolution, reduced accuracy, and potential uncertainties due to the influence of complex urban infrastructures. In urban studies, remote-sensing techniques are widely used to detect SUHI. Thermal infrared data acquired from satellites have been extensively applied to retrieve LST, surface heat fluxes, and to characterize the Urban Heat Island effect [**1.43**]. Multiple satellite platforms—such as NOAA-AVHRR, MODIS, ASTER, and Landsat—provide imagery that is routinely processed and analyzed for this purpose. Examples include the Basel Urban Boundary Layer Experiment (BUBBLE) [**1.44**], the PCACA (Pixel Component Arranging and Comparing Algorithm) model [**1.45**], and the URBANFLUXES Project [**1.46**]. Several studies have examined the human footprint through metrics such as Impervious Surface Area (ISA) [**1.47**] or urban density indices [**1.12**], comparing these with satellite-derived LST maps. They assessed the degree to which the human footprint affects LST in Asian (Bangkok) and American (continental U.S.A.) cities. For instance, regarding the American study, [**1.47**] analyzed the ISA from Landsat TM based NLCD dataset and LST from MODIS to assess UHI skin temperature amplitude and its relationship to develop intensity, size and ecological settings in 38 US cities. He found that ISA is the primary driver for increase in temperature explaining 70% of the total variance in LST. In some cases, remote sensed LST has also been employed for the validation and calibration of energy balance models [**1.48**]. In these studies, satellite observations are integrated with physically based models to assess the representativeness of mass and energy fluxes across different spatial resolutions. Nevertheless, satellite sensors are unable to retrieve the surface signal under cloudy conditions, as cloud cover obstructs the sensor's line of sight and the radiance measured originates primarily from the clouds rather than the land surface. Consequently, no reliable surface signal is obtained on cloudy days. Previous studies based on satellite data reported that, in large European cities, the average summer daytime $SUHII$ is $2.1 \pm 1.5,^{\circ}$C, while the average summer nighttime $SUHII$ is $1.0 \pm 0.4^{\circ}$C [**1.6**].

2 – Machine Learning models. Several studies have investigated LST using machine learning (ML) models. For example, recent research conducted in China [**1.49**] examined the seasonal effects of urban morphology, such as land cover, on LST across different urban functional zones using a Random Forest (RF) regression model. The results showed that, during summer, building presence was the dominant contributor to LST in residential, industrial, and public service areas, accounting for 34.14%, 21.21%, and 13.32% of the variability, re-

spectively. In commercial zones, both building morphology and landscape indicators played a significant role, with built-up intensity contributing 10.76% and vegetation density contributing 10.04% to LST.

3 – Global Circulation Models. Climate models are sophisticated physical–mathematical representations that describe the functioning of the Earth's climate system at global or local scales. They use differential equations to simulate interactions among the atmosphere, oceans, land surface, biosphere, and ice, enabling the understanding of past climate changes and the prediction of future climate evolution under various scenarios, such as those related to greenhouse gas emissions. These models are essential for studying climate dynamics, assessing human impacts on the climate, and supporting the development of mitigation strategies [**1.50**, **1.51**, **1.52**, **1.53**].

4 – Physical Models. To assess LST, a lot of physical based methods at local scale were implemented. These methods are based on Energy and/or Hydrological balance. LST, which is directly influenced by the surface energy balance, represents a critical variable for understanding urban thermal dynamics at both regional and global scales. Early one-dimensional energy balance models [**1.54**, **1.55**] did not distinguish between vegetation and soil surfaces. This limitation led to the development of two-layer models explicitly accounting for canopy–air and soil–air exchanges [**1.56**, **1.57**, **1.58**, **1.59**]. More recent distributed and multi-component approaches, including FEST–EWB [**1.60**] and the triple-SEB model [**1.61**], improve the representation of surface heterogeneity, although their application to complex urban environments remains limited. Then, several methods have been developed to estimate the main terms of the surface energy balance (SEB) in urban areas [**1.62**], often combined with data assimilation techniques [**1.63**, **1.64**, **1.65**, **1.66**, **1.67**]. These approaches are instrumental in mitigating the adverse effects of the surface urban heat island by identifying key drivers of urban warming. SEB-based methods have also been successfully applied to estimate evapotranspiration (ET) [**1.68**, **1.69**, **1.70**, **1.71**] and to quantify the impact of anthropogenic heat flux (AHF) on urban energy balances [**1.45**, **1.72**, **1.20**]. Among the notable frameworks, the Surface Urban Energy and Water Balance Scheme (SUEWS) [**1.73**] provides an effective tool to simulate urban surface energy and hydrological fluxes [**1.74**, **1.75**]. Among physical models at urban scale, there exists two main categories: Urban Land Surface models (ULSMs) and Urban Hydrological models (UHMs). The former is based on energy balance, the latter on water cycle. Nevertheless, the ULSMs don't mimic well water and hydraulic systems, and UHMs miss the surface en-

ergy balance solution [**1.76**]. ULSMs vary in complexity [**1.77**]. Bulk models, for instance, represent urban areas as modified bare soil by parameterizing physical properties such as heat capacity, thermal conductivity, albedo, roughness, and moisture. These models are commonly classified as one-tile, representing a single surface, or two-tile, distinguishing between roof and ground surfaces. Urban Canopy Models (UCMs), in contrast, conceptualize the urban environment as infinite street canyons with three primary facets—walls, roofs, and ground—and operate in two dimensions. UCMs can be implemented as single-layer models, assuming a homogeneous canyon, or as multilayer models, which resolve vertical atmospheric profiles. At the highest level of detail, Building-Resolving Models employ computational fluid dynamics (CFD) to simulate airflow and thermal conditions in three dimensions, explicitly representing the geometry of individual buildings and the heterogeneous urban landscape. Urban Hydrological Models focus primarily on hydrological processes and can be distinguished into hydraulic and hydraulic–hydrological models. Hydraulic models are designed to quantify rainfall–runoff inflows into urban drainage systems, often coupling with flow-routing models for conduits. They tend to simplify natural hydrological processes and are commonly implemented through tools such as the Storm Water Management Model (SWMM) [**1.78**]. Hydraulic–hydrological models, on the other hand, simulate broader hydrological processes to evaluate the impacts of urbanization but provide only limited representation of artificial pathways such as sewers, stormwater networks, and water supply systems. Recent studies [**1.76**] have highlighted the limitations and complementarities of these approaches, showing that ULSMs often inadequately represent water surfaces and hydraulic systems, whereas UHMs generally lack detailed building representations and explicit surface energy balance solutions. Coupled models demonstrate significant potential for simulating urban hydro-meteorological processes. Thus, to understand deeper the *LST* dynamics, it is necessary not to treat the two modules separately, but to combine them. Among the notable frameworks, the Surface Urban Energy and Water Balance Scheme (SUEWS) [**1.73**] provides an effective tool to simulate urban surface energy and hydrological fluxes [**1.74**, **1.75**]. Based on physical principles, several software have been developed to simulate urban climate variables, such as *LST*. Among these, there are, for instance, ENVI-met [**1.79**, **1.80**], MeteoBlue [**1.81**, **1.82**], and TERRA-URB [**1.83**].

In summery, remote sensing techniques effectively capture current urban thermal conditions, but are limited in temporal availability, fixed acquisition times, and sensitivity to atmospheric disturbances. Machine learning approaches, al-

though increasingly reliable, the physical basis is weaker, reducing their transferability. Global Climate Models (GCMs) are physically robust but too coarse to resolve intra-urban variability. At the local scale, physically based models show complementary limitations: ULSMs often simplify hydrological processes, while UHMs lack a detailed representation of surface energy balance. This limits their ability to capture the coupled processes governing LST, and coupled approaches at city scale remain scarce.

To address this gap, this thesis propose the implementation of a modeling framework with the following features: (i) *city-scale applicability*, bridging the gap between coarse-resolution climate models and point-based analysis; (ii) *physically based formulation*, explicitly coupling water and energy balance processes; (iii) *flexibility*, allowing the exploration of future climate scenarios; and (iv) *computational efficiency*, ensuring applicability over large urban domains with acceptable computational cost.

For both Milano and Amsterdam, several studies have been conducted to assess SUHI in specific urban areas, and various mitigation and adaptation projects have been developed accordingly.

In Milano, the temperature-mitigating benefits of green areas have been previously investigated [**1.84**, **1.85**], highlighting the role of urban vegetation in reducing surface and near-surface temperatures. These studies, however, were primarily focused on specific zones or case studies within the city, limiting their applicability for a city-wide assessment. To overcome these limitations, this work proposes a simplified yet physically based model capable of interpreting the mitigating effect of green areas over the entire urban area of Milano. Analysis of the dislocated stations in Milan shows that the greenest and most peripheral areas during summer exhibit lower sensible heat ($H = 130 - 140$ W m^{-2}) and higher latent heat ($LE = 100 - 120$ W m^{-2}). In contrast, the more central areas display higher sensible heat ($H = 250 - 300$ W m^{-2}) and lower latent heat ($LE = 20 - 50$ W m^{-2}) [**1.84**]. In northern Italy in particular, the presence of the urban heat island has amplified the bias in the air temperature series [**1.86**]. A recent study [**1.87**] found a positive relationship between $SUHI$ intensity and built-up areas in Northern Italy (Padua as pilot case). During summer 2022, three extreme heat waves (2 – 7 June, 21 – 23 July, 4 – 8 August) led to maximum temperatures of $35 - 36$°C. Urban heat islands were intense, with average land surface temperatures of 33.8°C and $SUHI$ intensity reaching $5 - 8$°C above rural areas, particularly in heavily urbanized zones. In the province of Milano,

during the most critical summers of recent years, a temperature difference of 6.8 °C was observed between artificial and natural surfaces [**1.14**]. Milano's climate is already highly critical, as is the case for many large Mediterranean cities such as Madrid and Athens. A significant share of heat-related deaths in Milano is linked to ongoing climate change and global warming. A recent study [**1.88**] reported that climate change was responsible for a substantial proportion of heat-related mortality across Europe during the summer. In Italy, Milano recorded the highest national toll, with 1,156 estimated deaths attributable to extreme heat between June and August 2025.

In Amsterdam, several studies have highlighted the crucial role of citizen science in supporting research [**1.89**, **1.90**] aimed at assessing climate perception and related impacts. Some studies also engaged citizens to raise awareness. In this case, 571 indoor temperature records were gathered through a citizen science crowd-sourcing approach, showing a median value of 28.0°C on the warmest day of the study period. During the same period, outdoor mean minimum and maximum temperatures reached 20.6°C and 31.1°C, respectively. The findings reveal that temperatures collected via crowd-sourcing are significantly higher than those obtained through professional methods, highlighting the importance of professional indoor monitoring networks [**1.89**]. Several projects have been conducted to study the Urban Heat Island effect in Amsterdam. Among them, the Amsterwarm project [**1.91**] produced diurnal and nocturnal UHI maps based on Land Surface Temperature derived from satellite imagery and Urban Canopy Layer (UCL) temperature measured by Automatic Weather Stations (AWS). In addition, the project developed a third type of map showing the difference between nocturnal and diurnal temperatures on two consecutive days, in order to evaluate the capacity of different land uses to cool down after heat accumulation. This research was focused on the August 2006 heat wave and revealed that the intensity of the UHI in Amsterdam ranks among the highest in Europe. During this event, the temperature difference between water bodies and highly impervious urban areas reached up to 11.6°C. Another important project is the 4TU.HERITAGE [**1.92**, **1.93**, **1.76**]. The 4TU.HERITAGE program develops an advanced sensing and design system to detect, reduce, and prevent heat stress in urban environments and buildings in Dutch cities. By monitoring and forecasting spatiotemporal heat stress patterns at an unprecedented 1-meter resolution, it aims to provide socio-technical solutions that mitigate indoor and outdoor heat stress while delivering urban design guidelines that connect energy transition, housing needs, area repurposing, climate adaptation, and digitalization.

Thesis framework

In this PhD dissertation, a physically based and spatially semi-distributed method was implemented, following the Surface Water–Energy Balance ($SWEB$) framework. Remote-sensing products, such as LST datasets from MODIS and Landsat 8, were used to calibrate the model. General Circulation Models (GCMs) provided the basis for future climate inputs, including air temperature, precipitation, and wind speed. The GCM outputs were downloaded from the Copernicus project [**1.94**], downscaled to the spatial resolution required by the $SWEB$ model, and then used as input forcing data. This Ph.D. thesis is organized as follows: In chapters 2 and 3 the two case studies are introduced, and used data; in Chapter 4 the methodology is presented; in chapter 5 the main results are shown and the discussion and conclusion are given in chapter 6 and 7. In the end, key conclusions based on findings, and ways forward, are shown.

References

[**1.1**] C. O'Malley, P. Piroozfar, E.R.P. Farr, and F. Pomponi. "Urban Heat Island (UHI) mitigating strategies: A case-based comparative analysis". In: *Sustainable Cities and Society* 19 (2015), pp. 222–235. DOI: 10.1016/j.scs.2015.05.009.

[**1.2**] L. Howard. "The climate of London: deduced from meteorological observations, made at different places in the neighbourhood of the metropolis". In: *MDPI* 1 (1818).

[**1.3**] W.G.V. Balchin and N. Pye. "A micro-climatological investigation of bath and the surrounding district". In: *Quarterly Journal of the Royal Meteorological Society* 73 (1947), pp. 297–323. DOI: 10.1002/qj.49707331706.

[**1.4**] Rao Krishna. "Remote sensing of urban heat islands from an environmental satellite". In: *Bull. Am. Meteorol. Soc.* 53 (1972), pp. 647–648.

[**1.5**] KIM and L. Marth. "Simple formulation of turbolent mixing in the stable free atmosphere and nocturnal boundary layer". In: *Tellus A* (1992), pp. 381–394.

[**1.6**] S. Peng, S. Piao, P. Ciais, P. Friedlingstein, C. Ottle, F. M. Bréon, H. Nan, L. Zhou, and R.B. Myneni. "Response to comment on "Surface urban heat island across 419 global big cities"". In: *Environmental Science and Technology* 46.12 (2012), pp. 6889–6890. DOI: 10.1021/es301811b.

[**1.7**] Sylvain Dupont and Patrice G. Mestayer. "Parameterization of the urban energy budget with the submesoscale soil model". In: *Journal of Applied Meteorology and Climatology* 45.12 (2006), pp. 1744–1765. DOI: 10.1175/JAM2417.1.

[**1.8**] S. Changnon, K. Kunkel, and B. Reinke. "Impacts and responses to the 1995 heat wave: A call to action". In: *Bulletin of the American Meteorological society* 77.7 (1996), pp. 1497–1506.

[**1.9**] S.A. Lowe. "An energy and mortality impact assessment of the urban heat island in the US". In: *Environmental Impact Assessment Review* 56 (2016), pp. 139–144.

[**1.10**] S. Konopacki and H. Akbari. "Energy savings of heat-island reduction strategies in Chicago and Houston (including updates for Baton Rouge, Sacramento, and Salt Lake City)". In: *Environmental Energy Technologies Division* (2002).

[**1.11**] Y. Hirano and T. Fujita. "Evaluation of the impact of the urban heat island on residential and commercial energy consumption in Tokyo". In: *Energy* 37.1 (2012), pp. 371–383.

[**1.12**] S. Bonafoni and C. Keeratikasikorn. "Land surface temperature and urban density: Multiyear modeling and relationship analysis using modis and landsat data". In: *Remote Sensing* 10.9 (2018). DOI: 10.3390/rs10091471.

[**1.13**] X. Ge, D. Mauree, R. Castello, and J.L. Scartezzini. "Spatio-temporal relationship between land cover and land surface temperature in urban areas: A case study in Geneva and Paris". In: *ISPRS International Journal of Geo-Information* 9.10 (2020). DOI: 10.3390/ijgi9100593.

[**1.14**] M. Puche, A. Vavassori, and M.A. Brovelli. "Insights into the Effect of Urban Morphology and Land Cover on Land Surface and Air Temperatures in the Metropolitan City of Milan (Italy) Using Satellite Imagery and In Situ Measurements". In: *Remote Sensing* 15.3 (2023). DOI: 10.3390/rs15030733.

[**1.15**] M. Nuruzzaman. "Urban heat island: causes, effects and mitigation measures-a review". In: *International Journal of Environmental Monitoring and Analysis* 3.2 (2015), pp. 67–73.

[**1.16**] N.H. Wong and C. Yu. "Study of green areas and urban heat island in a tropical city". In: *Habitat international* 29.3 (2005), pp. 547–558.

[**1.17**] K. R. Gunawardena, M.J. Wells, and T. Kershaw. "Utilising green and bluespace to mitigate urban heat island intensity". In: *Science of the total environment* 584 (2017), pp. 1040–1055.

[**1.18**] D.J. Sailor and L. Lu. "A top–down methodology for developing diurnal and seasonal anthropogenic heating profiles for urban areas". In: *Atmospheric environment* 38.17 (2004), pp. 2737–2748.

[**1.19**] P. Shahmohamadi, A.I. Che-Ani, K.N.A. Maulud, N.M. Tawil, and N.A.G. Abdullah. "The impact of anthropogenic heat on formation of urban heat island and energy consumption balance". In: *Urban Studies Research* 2011.1 (2011), p. 497524.

[**1.20**] C. Yuan, A.S. Adelia, S. Mei, W. He, X.X. Li, and L. Norford. "Mitigating intensity of urban heat island by better understanding on urban morphology and anthropogenic heat dispersion". In: *Building and Environment* 176.April (2020), p. 106876. DOI: 10.1016/j.buildenv.2020.106876.

[1.21] D. Gachkar, S.H. Taghvaei, and S. Norouzian-Maleki. "Outdoor thermal comfort enhancement using various vegetation species and materials (case study: Delgosha Garden, Iran)". In: *Sustainable Cities and Society* 75 (2021), p. 103309.

[1.22] E. Morini, A.G. Touchaei, B. Castellani, F. Rossi, and F. Cotana. "The impact of albedo increase to mitigate the urban heat island in Terni (Italy) using the WRF model". In: *Sustainability* 8.10 (2016), p. 999.

[1.23] X. Sun, X. Tan, K. Chen, S. Song, X. Zhu, and D. Hou. "Quantifying landscape-metrics impacts on urban green-spaces and water-bodies cooling effect: The study of Nanjing, China". In: *Urban Forestry and Urban Greening* 55 (2020). DOI: 10.1016/j.ufug.2020.126838.

[1.24] X. Chen, H. Wang, and J. Yang. "Effect of green blue spaces on the urban thermal environment: A field study in Hong Kong". In: *Urban Climate* 55.February (2024), p. 101912. DOI: 10.1016/j.uclim.2024.101912.

[1.25] S.W. Kim and R.D. Brown. "Urban heat island (UHI) intensity and magnitude estimations: A systematic literature review". In: *Science of the Total Environment* 779 (2021). DOI: 10.1016/j.scitotenv.2021.146389.

[1.26] M.R. Marselle, K. N. Irvine, A. Lorenzo-arribas, and S.L. Warber. "Does perceived restorativeness mediate the effects of perceived biodiversity and perceived naturalness on emotional well-being following group walks in nature ?" In: *Journal of Environmental Psychology* 46 (2016), pp. 217–232. DOI: 10.1016/j.jenvp.2016.04.008.

[1.27] E. Beele, M. Reyniers, R. Aerts, and B. Somers. "Spatial configuration of green space matters: Associations between urban land cover and air temperature. Landscape and Urban Planning. Accepted pending minor revisions." In: *Landscape and Urban Planning* 249.May (2024), p. 105121. DOI: 10.1016/j.landurbplan.2024.105121.

[1.28] M. Imran, A. Rauf, T. Abu-Izneid, M. Nadeem, M.A. Shariati, I.A. Khan, A. Imran, I. E. Orhan, M. Rizwan, and M. Atif. "Luteolin, a flavonoid, as an anticancer agent: A review". In: *Biomedicine & Pharmacotherapy* 112 (2019), p. 108612.

[1.29] Xing Z., Liutao C., and Jiachuan Y. "Simulation framework for early design guidance of urban streets to improve outdoor thermal comfort and building energy efficiency in summer". In: *Building and Environment* 228 (2023), p. 109815. DOI: 10.1016/j.buildenv.2022.109815.

[**1.30**] F. Aram, E.H. García, E. Solgi, and S. Mansournia. "Urban green space cooling effect in cities". In: *Heliyon* 5.4 (2019).

[**1.31**] P.Y. Tan, N.H. Wong, C.L. Tan, S.K. Jusuf, K. Schmiele, and Z.Q. Chiam. "Transpiration and cooling potential of tropical urban trees from different native habitats". In: *Science of the Total Environment* 705 (2020), p. 135764.

[**1.32**] S. Zheng, J. Guldmann, Z. Wang, Z. Qiu, C. He, and K. Wang. "Experimental and theoretical study of urban tree instantaneous and hourly transpiration rates and their cooling effect in hot and humid area". In: *Sustainable Cities and Society* 68 (2021), p. 102808.

[**1.33**] E.B. Peters, R. V. Hiller, and J.P. McFadden. "Seasonal contributions of vegetation types to suburban evapotranspiration". In: *Journal of Geophysical Research: Biogeosciences* 116.1 (2011), pp. 1–16. DOI: 10.1029/2010JG001463.

[**1.34**] T R Oke. "City size and the urban heat island". In: *Atmospheric Environment (1967)* 7.8 (1973), pp. 769–779. DOI: 10.1016/0004-6981(73)90140-6.

[**1.35**] P. Ampatzidis and T. Kershaw. "A review of the impact of blue space on the urban microclimate". In: *Science of the total environment* 730 (2020), p. 139068.

[**1.36**] L. Jiang, S. Liu, C. Liu, and Y. Feng. "How do urban spatial patterns influence the river cooling effect? A case study of the Huangpu Riverfront in Shanghai, China". In: *Sustainable Cities and Society* 69 (2021), p. 102835.

[**1.37**] E.A. Hathway and S. Sharples. "The interaction of rivers and urban form in mitigating the Urban Heat Island effect: A UK case study". In: *Building and environment* 58 (2012), pp. 14–22.

[**1.38**] A. Barrios-Barocio, O. Peralta, C.A. Ochoa-Moya, E. Luyando, and M. Espinosa-Fuentes. "Heat wave: a new characterization in terms of energy". In: *Frontiers in Environmental Science* 12 (2024), pp. 1–9. DOI: 10.3389/fenvs.2024.1474608.

[**1.39**] M. Yu, X. Chen, J. Yang, and S. Miao. "A new perspective on evaluating high-resolution urban climate simulation with urban canopy parameters". In: *Urban Climate* 38.June (2021), p. 100919. DOI: 10.1016/j.uclim.2021.100919.

[1.40] Brian C. O'Neill, Claudia Tebaldi, Detlef P. Van Vuuren, Veronika Eyring, Pierre Friedlingstein, George Hurtt, Reto Knutti, Elmar Kriegler, Jean Francois Lamarque, Jason Lowe, Gerald A. Meehl, Richard Moss, Keywan Riahi, and Benjamin M. Sanderson. "The Scenario Model Intercomparison Project (ScenarioMIP) for CMIP6". In: *Geoscientific Model Development* 9.9 (2016), pp. 3461–3482. DOI: 10.5194/gmd-9-3461-2016.

[1.41] T. D. Mushore, J. Odindi, T. Dube, and O. Mutanga. "Prediction of future urban surface temperatures using medium resolution satellite data in Harare metropolitan city, Zimbabwe". In: *Building and Environment* 122 (2017), pp. 397–410.

[1.42] U. Avdan and G. Jovanovska. "Algorithm for automated mapping of land surface temperature using LANDSAT 8 satellite data". In: *Journal of sensors* 2016.1 (2016), p. 1480307.

[1.43] Q. Weng. "Thermal infrared remote sensing for urban climate and environmental studies: Methods, applications, and trends". In: *ISPRS Journal of Photogrammetry and Remote Sensing* 64.4 (2009), pp. 335–344. DOI: 10.1016/j.isprsjprs.2009.03.007.

[1.44] G. Rigo and E. Parlow. "Modelling the ground heat flux of an urban area using remote sensing data". In: *Theoretical and Applied Climatology* 90.3-4 (2007), pp. 185–199. DOI: 10.1007/s00704-006-0279-8.

[1.45] Y. Liu, G. Shintaro, D. Zhuang, and W. Kuang. "Urban surface heat fluxes infrared remote sensing inversion and their relationship with land use types". In: *Journal of Geographical Sciences* 22.4 (2012), pp. 699–715. DOI: 10.1007/s11442-012-0957-7.

[1.46] C. Feigenwinter, E. Vogt R.and Parlow, F. Lindberg, M. Marconcini, F. Frate, and N. Chrysoulakis. "Spatial Distribution of Sensible and Latent Heat Flux in the City of Basel (Switzerland)". In: *IEEE Journal of Selected Topics in Applied Earth Observations and Remote Sensing* 11.8 (2018), pp. 2717–2723. DOI: 10.1109/JSTARS.2018.2807815.

[1.47] M.L. Imhoff, P. Zhang, R.E. Wolfe, and L. Bounoua. "Remote sensing of the urban heat island effect across biomes in the continental USA". In: *Remote Sensing of Environment* 114.3 (2010), pp. 504–513. DOI: 10.1016/j.rse.2009.10.008.

[**1.48**] C. Corbari, J.A. Sobrino, M. Mancini, and V. Hidalgo. "Mass and energy flux estimates at different spatial resolutions in a heterogeneous area through a distributed energy-water balance model and remote-sensing data". In: *International Journal of Remote Sensing* 34.9-10 (2013), pp. 3208–3230. DOI: 10.1080/01431161.2012.716924.

[**1.49**] Y. Liu, W. Zhang, W. Liu, Tan Z., S. Hu, Z. Ao, J. Li, and H. Xing. "Exploring the seasonal effects of urban morphology on land surface temperature in urban functional zones". In: *Sustainable Cities and Society* 103 (2024), p. 105268. DOI: 10.1016/j.scs.2024.105268.

[**1.50**] X Zhao and X Liu. "Primary and secondary ice production: interactions and their relative importance". In: *Atmospheric Chemistry and Physics* 22.4 (2022), pp. 2585–2600. DOI: 10.5194/acp-22-2585-2022.

[**1.51**] A. Cherchi, P. G. Fogli, T. Lovato, D. Peano, D. Iovino, S. Gualdi, S. Masina, E. Scoccimarro, S. Materia, A. Bellucci, and A. Navarra. "Global Mean Climate and Main Patterns of Variability in the CMCC-CM2 Coupled Model". In: *Journal of Advances in Modeling Earth Systems* 11.1 (2019), pp. 185–209. DOI: 10.1029/2018MS001369.

[**1.52**] J.L. García-Franco, L.J. Gray, and S. Osprey. "The American monsoon system in HadGEM3 and UKESM1". In: *Weather and Climate Dynamics* 1.2 (2020), pp. 349–371. DOI: 10.5194/wcd-1-349-2020.

[**1.53**] T. Kataoka, H. Tatebe, H. Koyama, T. Mochizuki, K. Ogochi, H. Naoe, Y. Imada, H. Shiogama, M. Kimoto, and M. Watanabe. "Seasonal to Decadal Predictions With MIROC6: Description and Basic Evaluation". In: *Journal of Advances in Modeling Earth Systems* 12.12 (2020), pp. 1–25. DOI: 10.1029/2019MS002035.

[**1.54**] T.N. Carlson, J.K. Dodd, Stanley G Benjamin, and J.N. Cooper. "Satellite estimation of the surface energy balance, moisture availability and thermal inertia". In: *Journal of Applied Meteorology and Climatology* 20.1 (1981), pp. 67–87.

[**1.55**] S. Barbagallo, S. Consoli, and A. Russo. "A one-layer satellite surface energy balance for estimating evapotranspiration rates and crop water stress indexes". In: *Sensors* 9.1 (2009), pp. 1–21.

[**1.56**] B.J. Choudhury. "Monitoring global land surface using Nimbus-7 37 GHz data theory and examples". In: *International Journal of Remote Sensing* 10.10 (1989), pp. 1579–1605.

[1.57] W.P. Kustas. "Estimates of evapotranspiration with a one-and two-layer model of heat transfer over partial canopy cover". In: *Journal of Applied Meteorology and Climatology* 29.8 (1990), pp. 704–715.

[1.58] J.M. Norman, W.P. Kustas, and K.S. Humes. "Source approach for estimating soil and vegetation energy fluxes in observations of directional radiometric surface temperature". In: *Agricultural and Forest Meteorology* 77.3-4 (1995), pp. 263–293.

[1.59] M. Friedl. "Forward and inverse modeling of land surface energy balance using surface temperature measurements". In: *Remote sensing of environment* 79.2-3 (2002), pp. 344–354.

[1.60] C. Corbari, G. Ravazzani, and M. Mancini. "A distributed thermodynamic model for energy and mass balance computation: FEST-EWB". In: *Hydrological Processes* 25.9 (2011), pp. 1443–1452. DOI: 10.1002/hyp.7910.

[1.61] Q. Weng, M.K. Firozjaei, M. Kiavarz, S.K. Alavipanah, and S. Hamzeh. "Normalizing land surface temperature for environmental parameters in mountainous and urban areas of a cold semi-arid climate". In: *Science of the Total Environment* 650 (2019), pp. 515–529.

[1.62] T.R. Oke and H.A. Cleugh. "Urban heat storage derived as energy balance residuals". In: *Boundary-Layer Meteorology* 39.3 (1987), pp. 233–245.

[1.63] W.G.M. Bastiaanssen, M. Menenti, R.A. Feddes, and A.A.M. Holtslag. "A remote sensing surface energy balance algorithm for land (SEBAL). 1. Formulation". In: *Journal of hydrology* 212 (1998), pp. 198–212.

[1.64] W.G.M. Bastiaanssen, H. Pelgrum, J. Wang, Y. Ma, J.F. Moreno, G.J. Roerink, and T. Van der Wal. "A remote sensing surface energy balance algorithm for land (SEBAL).: Part 2: Validation". In: *Journal of hydrology* 212 (1998), pp. 213–229.

[1.65] G.J. Roerink, Z. Su, and M. Menenti. "S-SEBI: A simple remote sensing algorithm to estimate the surface energy balance". In: *Physics and Chemistry of the Earth, Part B: Hydrology, Oceans and Atmosphere* 25.2 (2000), pp. 147–157.

[1.66] Y. Liou and S.K. Kar. "Evapotranspiration estimation with remote sensing and various surface energy balance algorithms—A review". In: *Energies* 7.5 (2014), pp. 2821–2849.

[**1.67**] R. Abolafia-Rosenzweig, B. Livneh, E.E. Small, and S.V. Kumar. "Soil moisture data assimilation to estimate irrigation water use". In: *Journal of Advances in Modeling Earth Systems* 11.11 (2019), pp. 3670–3690.

[**1.68**] R. Jackson, S. Idso, R. Reginato, and P. Pinter. "Canopy temperature as a crop water stress indicator". In: *Water resources research* 17.4 (1981), pp. 1133–1138.

[**1.69**] W. P. Kustas and J. M. Norman. "A two-source energy balance approach using directional radiometric temperature observations for sparse canopy covered surfaces". In: *Agronomy Journal* 92.5 (2000), pp. 847–854. DOI: 10.2134/agronj2000.925847x.

[**1.70**] O. D. Anderson and F. C. Greene. "The α-gliadin gene family. II. DNA and protein sequence variation, subfamily structure, and origins of pseudogenes". In: *Theoretical and Applied Genetics* 95.1-2 (1997), pp. 59–65. DOI: 10.1007/s001220050532.

[**1.71**] G. B. Senay, M. E. Budde, and J. P. Verdin. "Enhancing the Simplified Surface Energy Balance (SSEB) approach for estimating landscape ET: Validation with the METRIC model". In: *Agricultural Water Management* 98.4 (2011), pp. 606–618. DOI: 10.1016/j.agwat.2010.10.014.

[**1.72**] A. Buyantuyev and J. Wu. "Urban heat islands and landscape heterogeneity: Linking spatiotemporal variations in surface temperatures to land-cover and socioeconomic patterns". In: *Landscape Ecology* 25.1 (2010), pp. 17–33. DOI: 10.1007/s10980-009-9402-4.

[**1.73**] C.S.B. Grimmond. "Urban Water Balance: 1. A Model for Daily Totals". In: *Water Resources Research* 22.10 (1986), pp. 1397–1403. DOI: 10.1029/WR022i010p01397.

[**1.74**] L. Järvi, C.S.B. Grimmond, and A. Christen. "The Surface Urban Energy and Water Balance Scheme (SUEWS): Evaluation in Los Angeles and Vancouver". In: *Journal of Hydrology* 411.3-4 (2011), pp. 219–237. DOI: 10.1016/j.jhydrol.2011.10.001.

[**1.75**] H.C. Ward, S. Kotthaus, L. Jarvi, and C.S.B. Grimmond. "Surface Urban Energy and Water Balance Scheme (SUEWS): Development and evaluation at two UK sites". In: *Urban Climate* 18 (2016), pp. 1–32. DOI: 10.1016/j.uclim.2016.05.001.

[**1.76**] X. Chen, J. Werf, A. Droste, and M. Coenders-gerrits. "Barriers of urban hydro-meteorological simulation : a review". In: *Hydrology and Earth System Sciences* 29.January (15 2025), pp. 3447–3480. DOI: 10.5194/hess-29-3447-2025.

[**1.77**] M.J. Lipson, S. Grimmond, M. Best, G. Abramowitz, A. Coutts, N. Tapper, J. Baik, M. Beyers, L. Blunn, and S. Boussetta. "Evaluation of 30 urban land surface models in the Urban-PLUMBER project: Phase 1 results". In: *Quarterly Journal of the Royal Meteorological Society* 150.758 (2024), pp. 126–169.

[**1.78**] J. Gironás, L.A. Roesner, L. A. Rossman, and J. Davis. "A new applications manual for the Storm Water Management Model(SWMM)". In: *Environmental Modelling & Software* 25.6 (2010), pp. 813–814.

[**1.79**] M. Bruse. "ENVI-met 3.0: updated model overview". In: *University of Bochum. Retrieved from: www. envi-met. com* 3 (2004).

[**1.80**] Stella Tsoka, A Tsikaloudaki, and T Theodosiou. "Analyzing the ENVI-met microclimate model's performance and assessing cool materials and urban vegetation applications–A review". In: *Sustainable cities and society* 43 (2018), pp. 55–76.

[**1.81**] meteoblue. *meteoblue Climate Data Store*. https://content.meteoblue.com/en. Accessed: Nov 2025. 2025.

[**1.82**] N. Bader, N. Zurfluh, J. Shin, and S. Schlögl. *Enhance the meteoblue City Climate Model by Climate Projections to assess Urban Climate Hazard*. Tech. rep. Copernicus Meetings, 2024.

[**1.83**] D. Cinquegrana, M. Montesarchio, A.L. Zollo, and E. Bucchignani. "Evaluation of the Urban Canopy Scheme TERRA-URB in the ICON Model at Hectometric Scale over the Naples Metropolitan Area". In: *Atmosphere* 15.9 (2024). DOI: 10.3390/atmos15091119.

[**1.84**] L. Mariani, S.G. Parisi, G. Cola, R. Lafortezza, G. Colangelo, and G. Sanesi. "Science of the Total Environment Climatological analysis of the mitigating effect of vegetation on the urban heat island of Milan , Italy". In: *Science of the Total Environment, The* 569-570 (2016), pp. 762–773. DOI: 10.1016/j.scitotenv.2016.06.111.

[**1.85**] G. Frustaci, S. Pilati, C. Lavecchia, and E. Montoli. "High-Resolution Gridded Air Temperature Data for the Urban Environment: The Milan Data Set". In: *Forecasting* 4.1 (2022), pp. 238–261. DOI: 10.3390/forecast4010014.

[**1.86**] Michele Brunetti, F. Mangianti, Maurizio Maugeri, and Teresa Nanni. "Urban heat island bias in Italian air temperature series". In: *Il Nuovo Cimento* 23 (2000), pp. 423–432.

[**1.87**] S.E. Pappalardo, C. Zanetti, and V. Todeschi. "Mapping urban heat islands and heat-related risk during heat waves from a climate justice perspective: A case study in the municipality of Padua (Italy) for inclusive adaptation policies". In: *Landscape and Urban Planning* 238 (2023). DOI: 10.1016/j.landurbplan.2023.104831.

[**1.88**] Imperial College London Grantham Institute. *Summer heat deaths in 854 European cities more than tripled due to climate change*. 2025.

[**1.89**] Esther Peerlings, Saša Vranic, Joy Ommer, Milan Kalas, and Gert Jan Steeneveld. "Indoor heat in Amsterdam: Comparing observed indoor air temperatures from a professional network and from a citizen science approach". In: *City and Environment Interactions* 24.September (2024), pp. 1–7. DOI: 10.1016/j.cacint.2024.100173.

[**1.90**] Arjan M. Droste, Bert G. Heusinkveld, Daniel Fenner, and Gert Jan Steeneveld. "Assessing the potential and application of crowdsourced urban wind data". In: *Quarterly Journal of the Royal Meteorological Society* 146.731 (2020), pp. 2671–2688. DOI: 10.1002/qj.3811.

[**1.91**] F. Van Der Hoeven and A. Wandl. "Amsterwarm: Mapping the landuse, health and energy-efficiency implications of the Amsterdam urban heat island". In: *Building Services Engineering Research and Technology* 36.1 (2015), pp. 67–88. DOI: 10.1177/0143624414541451.

[**1.92**] W. van der Meer, F. Zantinge, and G. J. Steeneveld. "Urban fluxes for free: Estimating urban turbulent surface fluxes from crowdsourced meteorological canyon layer observations". In: *City and Environment Interactions* 27.May (2025), p. 100201. DOI: 10.1016/j.cacint.2025.100201.

[**1.93**] A.D. Rocha, S. Vulova, M. Förster, B. Gioli, B. Matthews, C. Helfter, F. Meier, G. Steeneveld, J.F. Barlow, L. Järvi, N. Chrysoulakis, G. Nicolini, and B. Kleinschmit. "Unprivileged groups are less served by green cooling services in major European urban areas". In: *Nature Cities* 1.6 (2024), pp. 424–435. DOI: 10.1038/s44284-024-00077-x.

[1.94] Copernicus Climate Change Service. *Copernicus Climate Data Store (CDS).* `https://cds.climate.copernicus.eu/`. Accessed: Dec 2025. 2025.

Chapter 2

case study 1: MILANO

The study area is the city of Milano, capital town of Lombardia region, in northern Italy (45°28'38.28"N, 9°10'53.40"E). The area, laid within the Po river valley, has flat terrain, covers 181.8 km^2, and shows a small altitude range, between 102-147 m a.s.l. With its dense population of about 1.4 million inhabitants [**2.1**], Milano stands as a compelling hub for both students and professionals, commuting from the greater Milano province (Cittá Metropolitana). Climate here is classified as Cfa in the Köppen-Geiger classification [**2.2**], rather mild, with cold winters and hot summers. Average yearly precipitation meets ca. 920 mm, with average monthly air temperature spanning from -0.5 °C to +28°C. Land consumption, i.e. the occupation of natural land by artificial surfaces, is approximately 74% [**2.3**], and impervious surfaces account for 65% of the total area. Most of Milano's urban, and paved surfaces are located in its Northern part. In the south, land use displays more rural, and agricultural areas. Several large parks can be found here. Among others, Sempione Park was built at the end of the 19th century, nearby the old town center (and Sforzesco Castle, a worldwide known medieval fortress), the garden Giardini Pubblici Indro Montanelli was the first Park in Milano dedicated to collective leisure, Monte Stella Park was built in a suburban area, piling up city ruins after World War II bombings, and Parco Nord was cast upon a former military airport and Breda factory brownfield areas. In Figure 2.3, some main parks of Milano are shown in a map of vegetated fraction VF.

2.1 Meteorological and satellite data

Here, data from Automatic Weather Stations (AWS) were used as input, and remote sensing data were used to parameterize land use, and soil hydrology, to be used by the Surface Water-Energy balance model, to simulate urban land

surface temperature (LST). The meteorological stations (Figure 2.1), 9 in total, are managed, and their data are validated by the Regional Agency for Environmental Protection, ARPA Lombardia, an official source. Data covering 13 years (2010-2022) of daily global radiation (R_g), air temperature (T_a), liquid precipitation (P), wind velocity (v) and relative air humidity (RH), from the 9 AWS in Milano 2.1, were collected.

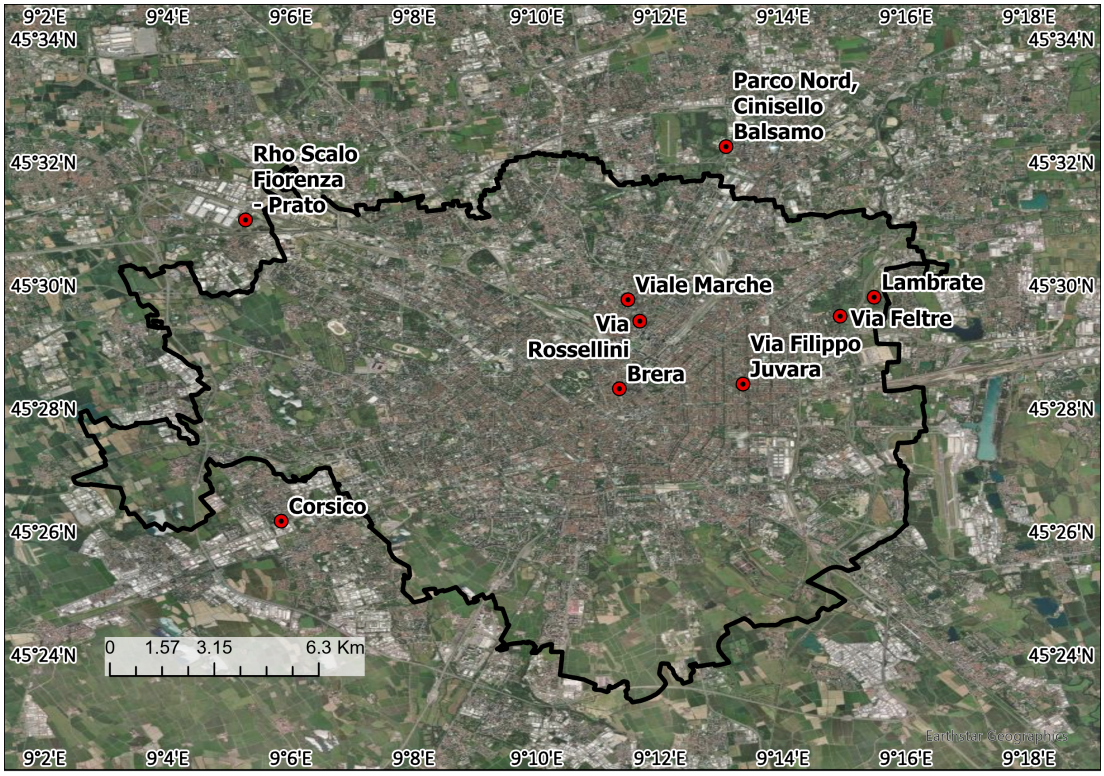

Figure 2.1. Study area with Automatic Weather Stations of ARPA in Milano.

Station	Lat. [°.']	Lon. [°.']	Variables
Rho Scalo Fiorenza - Prato	45.52	9.09	P (2015–2022), RH (2015–2022)
Parco Nord, Cinisello Balsamo	45.54	9.22	T_a, P, R_g, RH, v
Viale Marche	45.49	9.19	T_a, RH, v (2012–2022)
Via Rossellini	45.49	9.19	P (2012–2022)
Brera	45.47	9.19	T_a, P, R_g (2016–2022), RH, v (2014–2020)
Via Filippo Juvara	45.47	9.22	T_a, P, R_g, RH, v (2014–2022)
Lambrate	45.48	9.25	T_a, R_g, RH, v (2014–2022)
Via Feltre	45.49	9.24	T_a
Corsico	45.44	9.10	T_a, P, RH

Table 2.1. Weather stations used in this study. T_a[°C] is air temperature, P [mm] is liquid rainfall, RH [%] is relative air humidity, R_g [Wm^{-2}] is solar radiation, v [ms^{-1}] is wind velocity. If not specified, data refer to the observation period 2010 –2022.

For precipitation, air temperature, and global radiation, spatialization was pursued using *Kriging* technique, and variance reduction was employed, trough

correlation analysis [**2.4**]. Considering N available AWSs for the variable X, a spatial correlation function was built. In particular, *Kriging* requires:

- M: Covariance matrix of dimension $N \times N$;
- c: Covariance array between gauged and ungauged site of length N;
- $w = M^{-1}c$: Array of weights of length N.

The unknown variable X, at an ungauged position j is estimated, starting from all the gauged variables $\hat{X}$ at each of the N position i, via N weights $w_{i,j}$

$$X_j = \sum_{i=1}^{N} \hat{X}_i w_{i,j} \tag{2.1}$$

This process generates maps of air temperature, precipitation, and global radiation, spatializing the available data during 2010–2022. Using all available daily weather data from 2010 to 2022, we obtained a large number of couples (n) of recorded data, resulting in a very small confidence interval, or namely high/robust accuracy ($1/\sqrt{n} < 0.01$). Figure 2.2 shows the values of linear correlation coefficient ρ as a function of the planar distance dx. The results indicate that the correlation structure of (daily) precipitation scales linearly (within the investigated range) with geographical distance. Air temperature, and radiation also exhibit an inverse relationship with distance, though with a very mild slope (i.e. temperature, and radiation remain largely correlated in space). The AWSs network covers the entire area of Milan, with a radius of about 8 km, so the explored extent covers about 16 km, within which the observed high degree of correlation seemingly allows accurate assessment of spatial fields of the necessary weather variables (most notably precipitation, more erratically variable in space). In flat areas of Lombardy region, such as Milano here, wind speed is generally low, and wind patterns are somehow smooth [**2.5**]. Therefore, average (daily) wind velocity could be taken uniform across the entire domain. The same approach was applied to air humidity. This entailed calculating a daily mean of the variable from all available observations.

2.2 Land cover and soil properties

A land cover map was used to estimate the maximum soil retention potential W_{max}, [**2.6**, **2.7**], according to the SCS-CN method [**2.8**], and to assess the area covered by vegetation (trees, brushes, crops, forests, parks, garden,..), and by

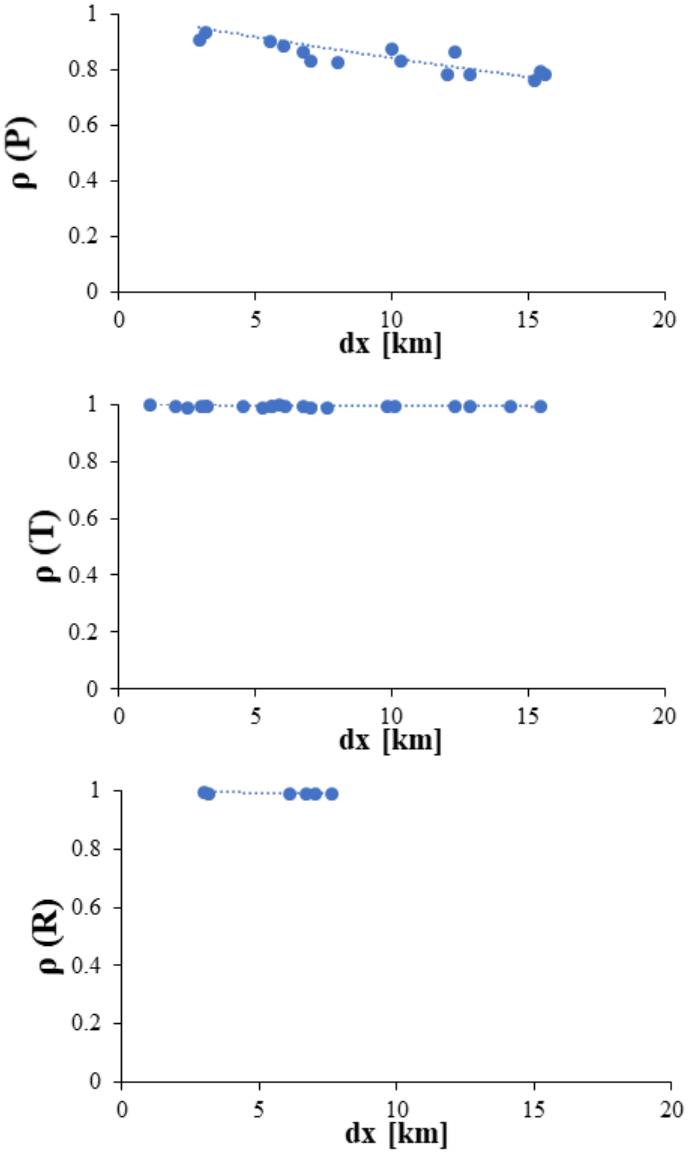

Figure 2.2. Correlation coefficient of: Precipitation P, Air Temperature T, Global Radiation R, against planar distance $dx[km]$.

urban soil (paved surface, wall, roads, buildings, industries, residential areas,..). The Land Use Land Cover map from the CORINE project was used to assess the Vegetation Fraction VF for each cell within the domain. Urban paved areas were assigned $VF = 0$, while green areas were assigned $VF = 1$. VF values were then averaged, and mapped to each pixel of the grid, as shown in Figure 2.3. Water content at permanent wilting point (θ_{WP}), field capacity (θ_{FC}), and saturation (θ_{sat}), as well as saturated hydraulic conductivity (K) were derived from soil texture [**2.9**]. The values of θ_{WP} , θ_{FC} and θ_{sat} were considered as constant as representative for the *Green Basin*, and the *Built-up Basin.* For the

model simulations, two hypothetical scenarios, that is one where Milano is entirely green (*Green Basin*), and one where it is entirely built up (*Built-Up Basin*) were defined. The parameters' values of the two virtual basins are reported in Table 4.1.

Weekly Leaf Area Index (LAI) values were used as model inputs within the *Green Basin* to evaluate soil resistance. These values were derived from the MOD15A2H Version 6.1 Moderate Resolution Imaging Spectroradiometer (MODIS) product, which provides an 8-day composite dataset, combining LAI and Fraction of Photosynthetically Active Radiation ($FPAR$) at a 500-meter pixel resolution. These data contain Level 3 information, and are already processed to remove cloud disturbance [**2.10**]. Significant LAI values are mapped in suburban areas, where extensive parks, and forests sprawl. On average, winter LAI is 0.41, and growing season (April-September) LAI is 1.21. LAI gradually grows starting from springs, reaching its maximum on August, then rapidly decreasing. These reference average values of LAI remain quite constant during the observation period.

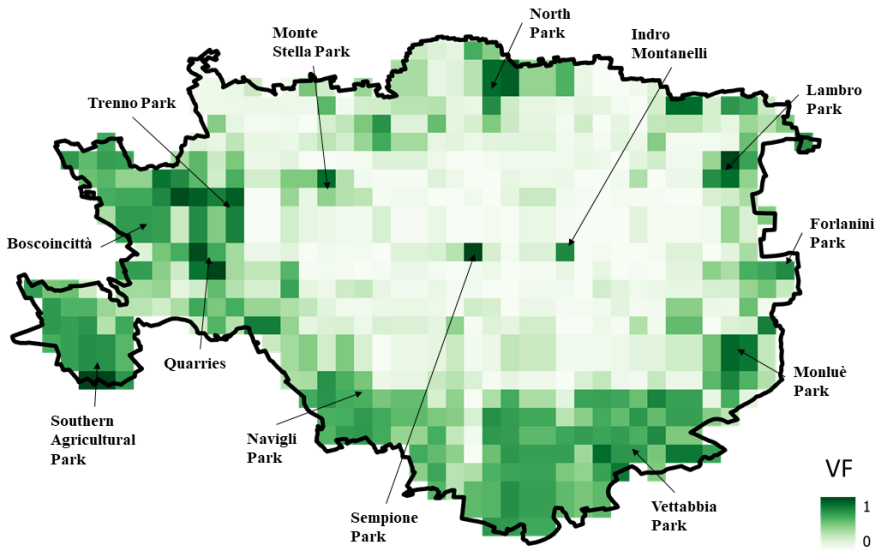

Figure 2.3. Vegetated Fraction VF map extracted from Land Use Land Cover map (DUSAF 6.0). Main parks in Milano are indicated.

2.3 Land Surface Temperature - MODIS

Land Surface Temperature data were obtained from the Terra Moderate Resolution Imaging Spectroradiometer (MODIS), specifically from the 8-Day (MOD11A2)

Version 6.1 product suite. This product is an average 8–day per–pixel *LST*, with a 1 km spatial resolution in a 1,200 by 1,200 km grid, and it may be suitable for hydrological modeling. However, the heterogeneity of urban areas can reduce the accuracy of observations. Daytime data of *LST* were downscaled at same resolution scale as *SWEB* model, i.e. 500 m $\times$ 500 m, trough GIS tools. Basically, the original raster was re-mapped using bilinear interpolation, a method well-suited for continuous data such *LST*. Satellite images were collected from January 2010 to December 2022, and then used for the model tuning. The *Geoportale del Comune di Milano* website introduced the average *LST* map obtained from Landsat-8 satellite. The high–resolution map provided by the geoportal, shown in Figure 2.4, classifies the city into *LST* classes and gives users an overview of the most sensitive areas of Milan based on *LST* value. It was also consulted to confirm the study findings.

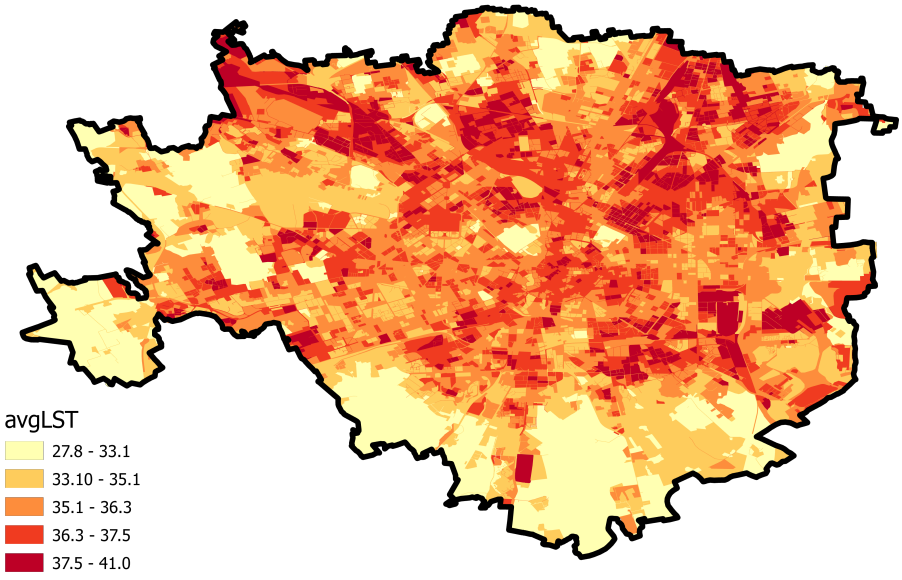

Figure 2.4. Average *LST*[°C] map provided by *Geoportale del Comune di Milano* [**2.11**].

References

[**2.1**] ISTAT - Istituto Nazionale di Statistica. *Popolazione residente al 1° gennaio*. https://www.istat.it/. Accessed: Feb 2023. 2023.

[**2.2**] M. C. Peel, B. L. Finlayson, and T. A. McMahon. "Updated world map of the Köppen-Geiger climate classification". In: *Hydrology and Earth System Sciences* 11.5 (2007), pp. 1633–1644. DOI: 10.5194/hess-11-1633-2007.

[**2.3**] PGT - Piano di Governo di Territorio. *PGT*. 2012. URL: https://www.pgt.comune.milano.it/pgt-previgente/pgt-2012-15112017.

[**2.4**] M.A. Oliver and W. Webster. "Kriging: a method of interpolation for geographical information systems". In: *International Journal of Geographical Information Systems* 4.3 (1990), pp. 313–332. DOI: 10.1080/02693799008941549.

[**2.5**] L. Ferrarin, L. Stucchi, and D. Bocchiola. "Statistical downscaling of GCMs wind speed data for trend analysis of future scenarios: a case study in the Lombardy region". In: *Theoretical and Applied Climatology* (2024). DOI: 10.1007/s00704-024-04921-x.

[**2.6**] M. Mancini and R. Rosso. "Using GIS to assess spatial variability of SCS Curve Number at the basin scale". In: *New Directions for Surface Water Modeling* (1989).

[**2.7**] D Bocchiola and R Rosso. "Advances in Water Resources Use of a derived distribution approach for flood prediction in poorly gauged basins : A case study in Italy". In: *Advances in Water Resources* 32.8 (2009), pp. 1284–1296. DOI: 10.1016/j.advwatres.2009.05.005.

[**2.8**] S. K. Mishra and V. P. Singh. "SCS-CN Method". In: *Soil conservation service curve number (SCS-CN) methodology* (2003), pp. 84–146.

[**2.9**] K. E. Saxton, W. J. Rawls, J. S. Romberger, and R. I. Papendick. "Estimating soil water characteristics-hydraulic conductivity". In: *Soil Science Society of America Journal* 5 (1986), pp. 1031–1036.

[**2.10**] N. Addimando, E. Nana, and D. Bocchiola. "Modeling Pasture Dynamics in a Mediterranean Environment: Case Study in Sardinia, Italy". In: *Journal of Irrigation and Drainage Engineering* 141.5 (2015), p. 04014063. DOI: 10.1061/(asce)ir.1943-4774.0000818.

[2.11] Comune di Milano. *Geoportale Comune di Milano – Open Data*. `https://geoportale.comune.milano.it/sit/open-data/`. Accessed: Nov 2025. 2025.

Chapter 3

case study 2: AMSTERDAM

The study area corresponds to the historic city center of Amsterdam, North Holland, the Netherlands (52.384122°N, 4.881703°E), as shown in Figure 3.1. The area of interest is delineated by the semi-circular waterway Singelgracht, which historically functioned as part of the city's defensive system. In the past, the canal was reinforced with ramparts and walls, most of which have since been removed, leaving the Singelgracht as the main physical boundary. The municipality of Amsterdam has about 0.9 million inhabitants [**3.1**]. However, in the city centre most buildings are dedicated to tourism or commercial activities, meaning the area is highly frequented by tourists but has relatively few residents. Within this perimeter, the Singelgracht encompasses the canal belt (UNESCO World Heritage Site), a high density of historical buildings, limited green spaces (e.g., the Artis Zoo), and the former harbor area of Oosterdok. The urban fabric of the city center is further characterized by a system of concentric ring canals, which structure its morphology and contribute to its distinctive spatial organization.

3.1 Meteorological and satellite data

Climate here is classified as *Cfb* in the Köppen-Geiger classification [**3.3**], rather mild, with cold winters and warm summers. Average yearly precipitation is about 1040 mm [**3.4**], with average monthly air temperature spanning from 3.5°C to 19.5 °C [**3.5**].

The study uses atmospheric and surface observations provided by the Meteorology and Air Quality (MAQ) group at Wageningen University through the Amsterdam Atmospheric Monitoring Supersite (AAMS). For this analysis, five AAMS weather stations located within the Singelgracht were selected. These stations measure air temperature, vapor pressure, vapor pressure deficit, wind

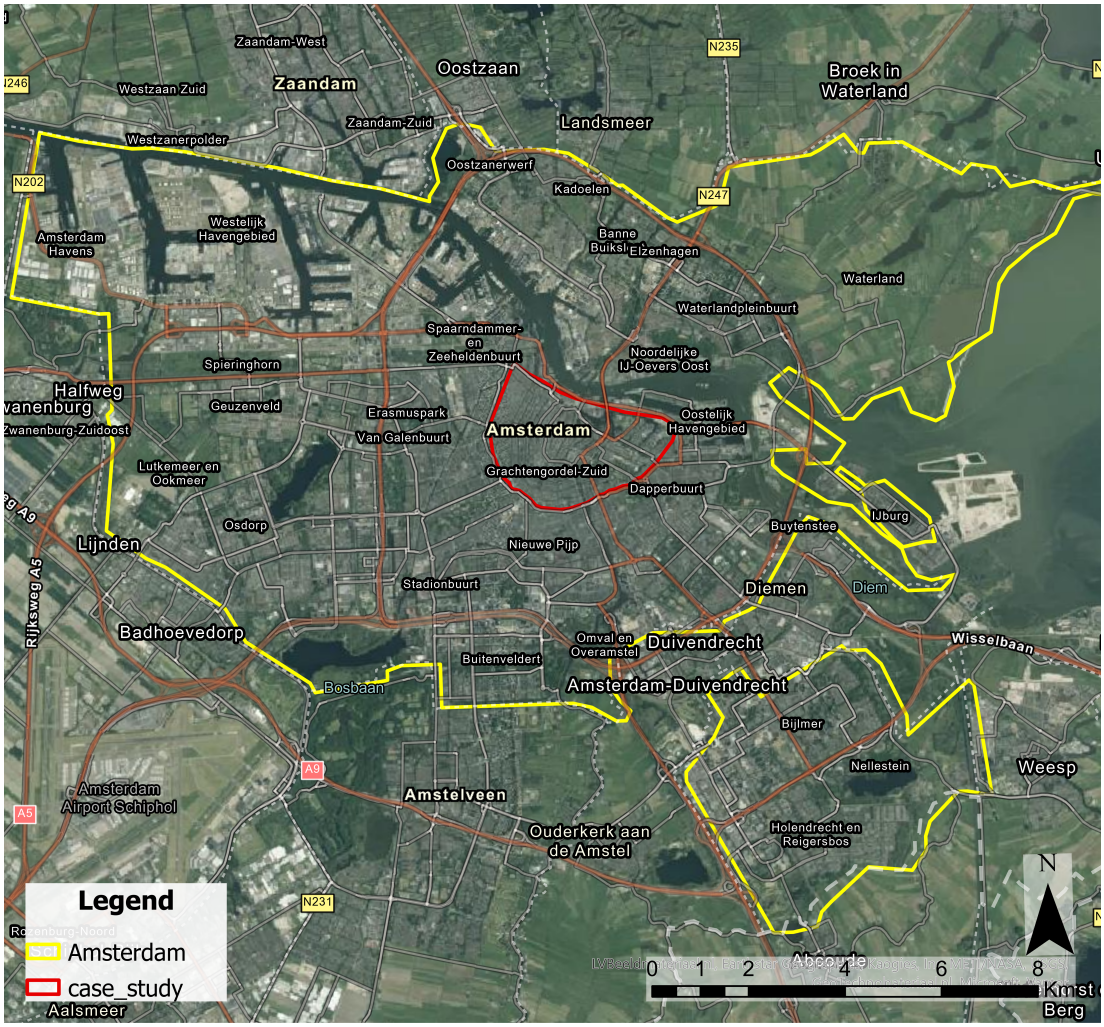

Figure 3.1. Amsterdam municipality boundaries (yellow) and study area (red). Basemap *Actueel_ortho25* product of PDOK-TOP10 [**3.2**]

speed, and wind direction. An eddy covariance flux tower, also managed by MAQ and located in the city center (52.3665°N, 4.8929°E, 40 m above ground level), provides continuous measurements of turbulent fluxes (sensible and latent heat), evapotranspiration, and radiative incoming and outcoming fluxes (short-wave and longwave). The locations of all the employed stations are reported in the Figure 3.2 and Table 3.1. Given its small surface area (about 6.9 km^2), the input meteorological data, such as air temperature and wind speed, were not spatialized with Kriging technique, as the values recorded at the stations were homogeneous, so they were averaged. Data have been collected for the summer seasons over a five-year period (2020–2024), as reported in Table 3.2.

Some issues remain in the dataset, resulting in occasional missing records. The original measurements were taken at intervals ranging from 1 to 30 minutes. For use in the model, the data were processed by averaging or cumulating them

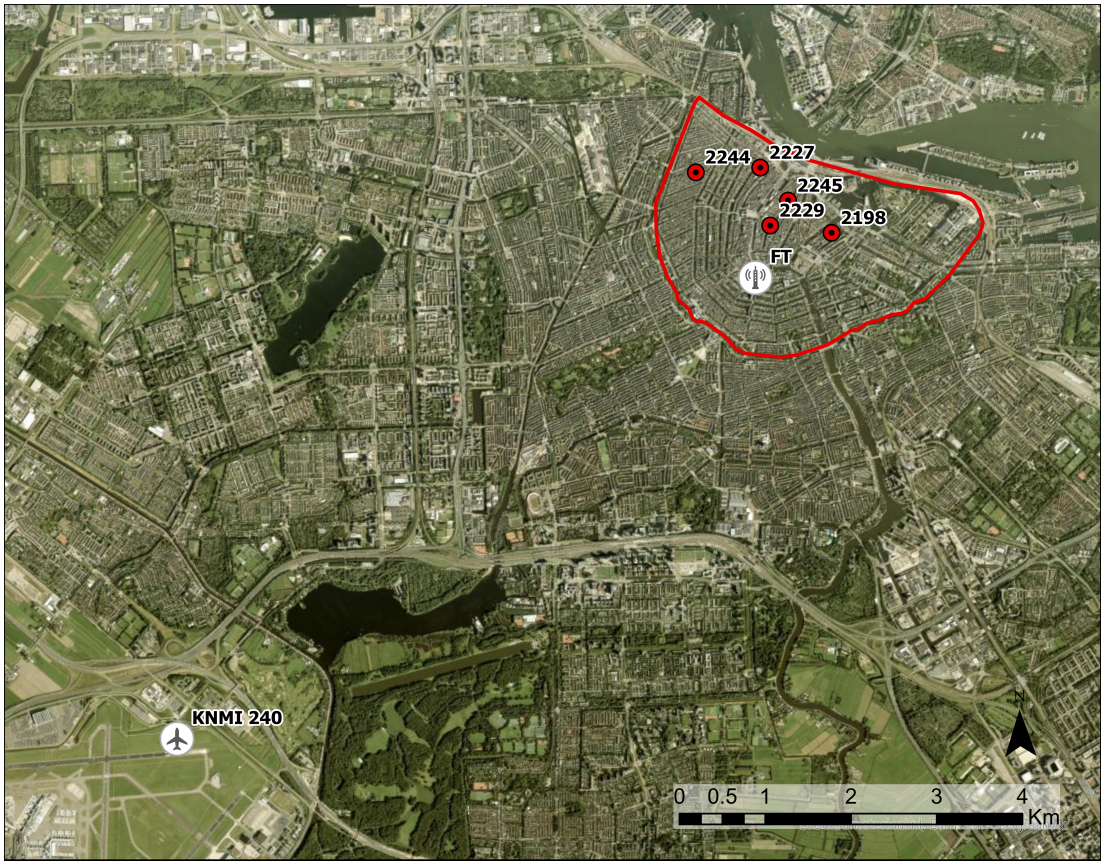

Figure 3.2. Study area and weather stations location. Red dots are the ASWs from AAMS project, FT is the eddy covariance flux tower and on the South-West there is the KNMI meteorological station located at Schiphol airport. The coordinates and the available variable are reported in Tables 3.2 and 3.1

Station	Lat. [°.']	Lon. [°.']	Variables
D2198	52.371	4.906	T_a, RH, v, VPD, SVP
D2227	52.377	4.894	T_a, RH, v, VPD, SVP
D2229	52.372	4.896	T_a, RH, v, VPD, SVP
D2244	52.378	4.883	T_a, RH, v, VPD, SVP
D2245	52.374	4.899	T_a, RH, v, VPD, SVP
FT	52.367	4.893	T_a, SW, LW, H, LE, v, RH
KNMI240	52.318	4.790	P, T_a, v, RH, SW

Table 3.1. Weather stations used in this study. T_a[°C] is air temperature, P [mm] is liquid rainfall, RH[%] is relative air humidity, SW[Wm^{-2}] is shortwave radiation, LW[Wm^{-2}] is longwave radiation, H[Wm^{-2}] is the sensible heat, LE[Wm^{-2}] is the latent heat, VPD [KPa] is the vapor pressure deficit, SVP [KPa] is the saturation vapor pressure and v[ms^{-1}] is wind velocity.

into hourly values, in order to achieve an hourly temporal resolution.

Variable	Description	Years	Sources
T_a[°C]	Air Temperature	2020-2024	MAQ, AAMS
SW[Wm^{-2}]	Corrected net shortwave radiation	2020-2024	MAQ
LW[Wm^{-2}]	Corrected net longwave radiation	2020-2024	MAQ
H[Wm^{-2}]	Sensible Heat	2020-2024	MAQ
LE[Wm^{-2}]	Latent Heat	2020-2023	MAQ
v[ms^{-1}]	Wind Speed	2020-2024	MAQ, AAMS
RH[%]	Relative Air Humidity	2021,2023	MAQ
VPD[KPa]	Vapor Pressure deficit	2020-2023	MAQ, AAMS
SVP[KPa]	Saturation Vapor Pressure	2020-2023	AAMS
P[mm]	Precipitation	2020-2024	KNMI Schipol station (240)

Table 3.2. Input data sources and year availability

Flux data The eddy covariance flux tower is set on the top of NH Collection Amsterdam hotel, in a very touristic area (Figure 3.3). By analysing the wind patterns under stable, neutral, and unstable conditions, it was possible to define the footprint of the heat fluxes recorded by the flux tower [**3.6**]. Most of the basin of study interest falls within this footprint. The eddy covariance technique is often adopted to analyze the energy balance, water vapor, CO_2 and other trace gasses over the atmosphere [**3.7**, **3.8**].

Figure 3.3. Eddy covariance Flux Tower (FT) location.

The measurement of sensible heat flux was conducted using a combination of a LI-COR Li-7500 open-path infrared gas analyzer and a Campbell CSAT3 three-dimensional sonic anemometer, following the eddy covariance methodology. The Li-7500 simultaneously measures fluctuations in CO_2 and H_2O concentrations, while the CSAT3 records three-dimensional wind velocity components at high frequency (about 10–20 Hz). By correlating the instantaneous vertical wind speed with the fluctuations in air temperature, the eddy covariance technique allows for the direct calculation of the sensible heat flux between the surface and

the atmosphere. The system is mounted on a flux tower, ensuring that measurements are taken within the constant flux layer and minimally influenced by obstacles or surface heterogeneity. Data are subsequently processed to remove spikes, apply coordinate rotation, and correct for density fluctuations following the Webb-Pearman-Leuning approach, providing reliable estimates of the turbulent sensible heat exchange over the study area.

At FT location, a double validation was possible, since there are the LST values evaluated trough the LW_{out} data recorded by the eddy-covariance station and the LST recognized by Landsat8 satellite images, at resolution about 31 m x 31 m. In this way, it has been also possible to assess the footprint of the sensor [**3.9**]. The results of calibration at FT location trough both Satellite images and outcoming longwave radiation records will be reported in Section 5.3.1.

KNMI Station An important official source of weather data in the Netherlands is the Koninklijk Nederlands Meteorologisch Instituut (KNMI), which is a network of official meteorological stations, managed by the Ministry of Infrastructure and Water Management and distributed throughout the country, that provides continuous meteorological observations. Temperature and precipitation measurements are taken from sensors mounted at a height of 1.8 m, whereas wind speed is recorded at 10 m above the surface. According to WMO recommendations, measurements at this height are considered free from the influence of nearby buildings or other obstacles. To obtain the wind velocity at the same reference height of AWS, hence 2 m, it was applied the wind speed profile formula (Equation 3.1), where z is the reference height (2 m), and z_0 the roughness. Considering a flat and empty surface, the friction is low, almost null.

$$v_{10} = v_z \cdot \frac{\ln \frac{10}{z_0}}{\ln \frac{z}{z_0}} \tag{3.1}$$

In this study, the climate variables obtained from KNMI were considered to compare the results with those from the Amsterdam-Singelgracht site. In particular, reference was made to station number 240 – Schiphol. At this station, no Eddy Covariance measurements are available; only solar radiation data are recorded, and therefore no direct observation of LST are provided.

3.2 Land cover and soil properties

Land cover and land use data were obtained from PDOK-TOP10 and LGN2022 datasets.

- PDOK-TOP10 **[3.2]** provides a high-quality, continuously updated governance dataset containing current geographic information for the Netherlands, as WMS file (Fig. 3.4).

- LGN2022 – Landelijk Grondgebruik Nederland 2022 **[3.10]** from Wageningen University and Research is a grid-based dataset representing Dutch land use in 2022 at a spatial resolution of 5 m, as raster file (Fig. 3.5).

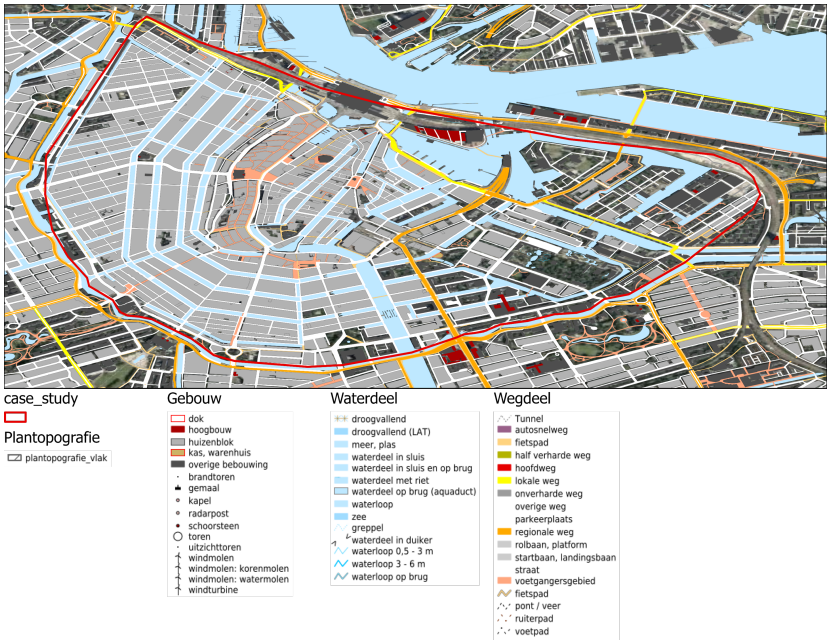

Figure 3.4. PDOK-TOP10 map - Reference System WGS1984

These datasets were used to characterize the spatial distribution of urban and non-urban areas within the study domain and to support the parametrization of the energy-water balance model. The parameters' values of the three virtual basins are reported in Table 4.2.

The study area was discretized into a grid with a spatial resolution of 100 m $\times$ 100 m. Within each grid cell, the relative proportion of land cover types (Built-up, Green and Water) was defined. Each cell in the domain is assigned a value between 0 and 1 representing the relative proportion of each land cover type: vegetation, or built-up, or wet areas (Figure 3.6). While Milano was discretized based on the presence of green areas using a single metric (Vegetation

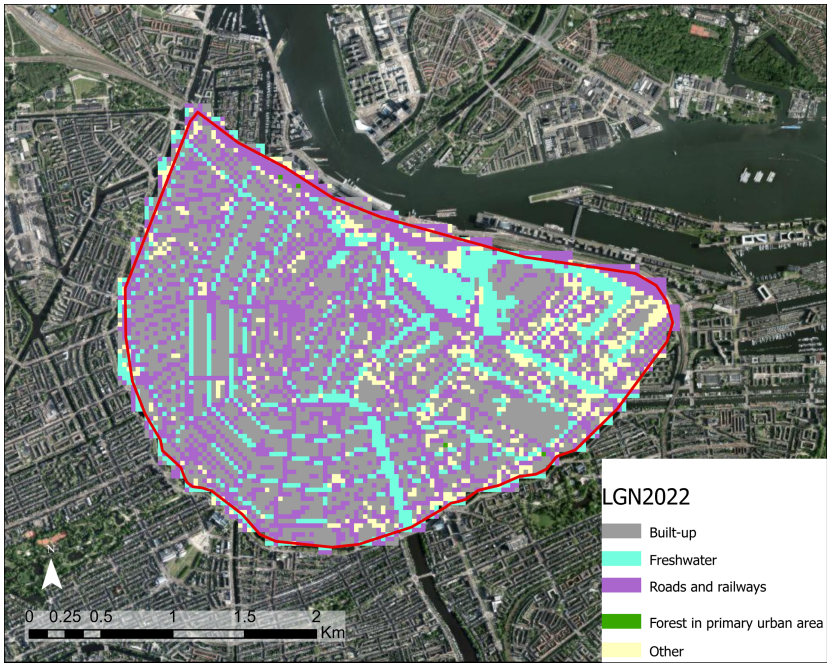

Figure 3.5. LGN2022 map - Reference System WGS194-UTM31N

Fraction, VF), the urban structure of Amsterdam's city center was characterized according to the proportional distribution of three land cover types. Three virtual catchments were defined to represent different land cover types: one characterized exclusively by vegetation, one fully urbanized and impervious, and one consisting solely of water bodies. These catchments are named respectively:

- *Green Basin*;
- *Built-up Basin*;
- *Water Basin*.

This approach allows for a more detailed representation of urban heterogeneity in terms of vegetation, built environment, and water bodies.

For the soil properties,the concept of Local Climate Zone (LCZ) has been adopted. LCZs [**3.11**] are regions of uniform surface cover, structure, material, and human activity that span hundreds of meters to several kilometers in horizontal scale. Each LCZ is individually named and ordered by one (or more) distinguishing surface property, such as the roughness parameters. In particular, it has been considered the World Urban Database and Access Portal Tools (WUDAPT) project [**3.12**] (Figure 3.7). The WUDAPT project acquires and disseminates climate-relevant information on cities worldwide [**3.13**]. Amsterdam city is part of this project.

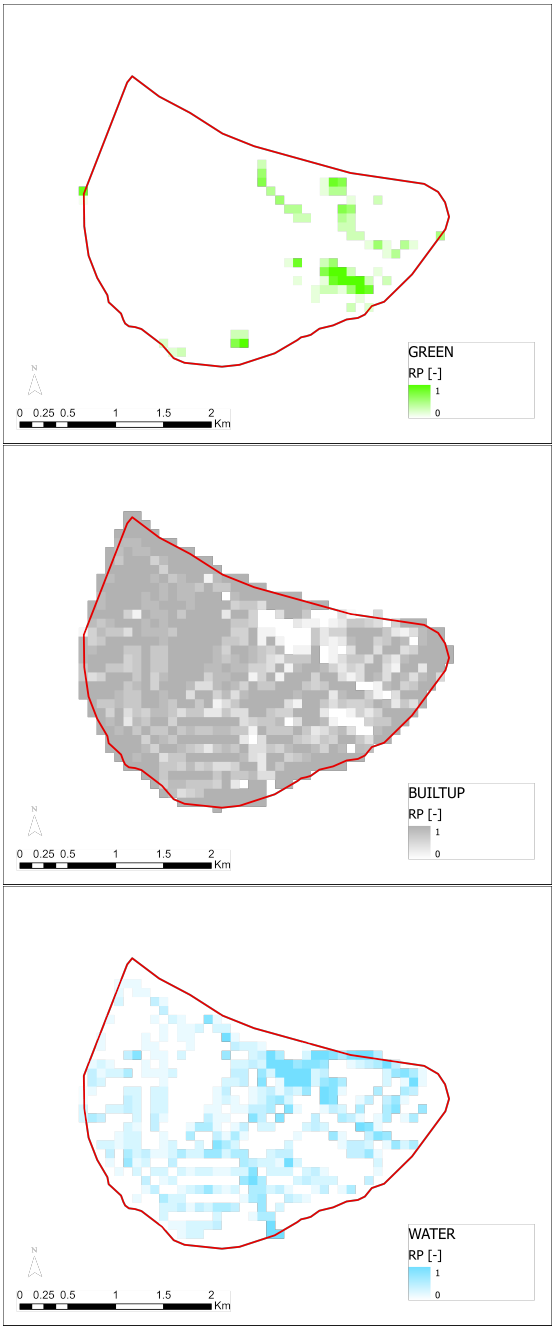

Figure 3.6. Fraction [0-1] of Green, Built-up and Water cover on the surface of Amsterdam's centre

According LCZs, most of Amsterdam city centre area is covered by "Compact mid-rise" surface (Figure 3.7), which means that:

- The majority of the area is occupied by buildings;
- The average buildings' height is $10 - 25$ m;
- Anthropogenic heat flux is less than 75Wm^{-2};

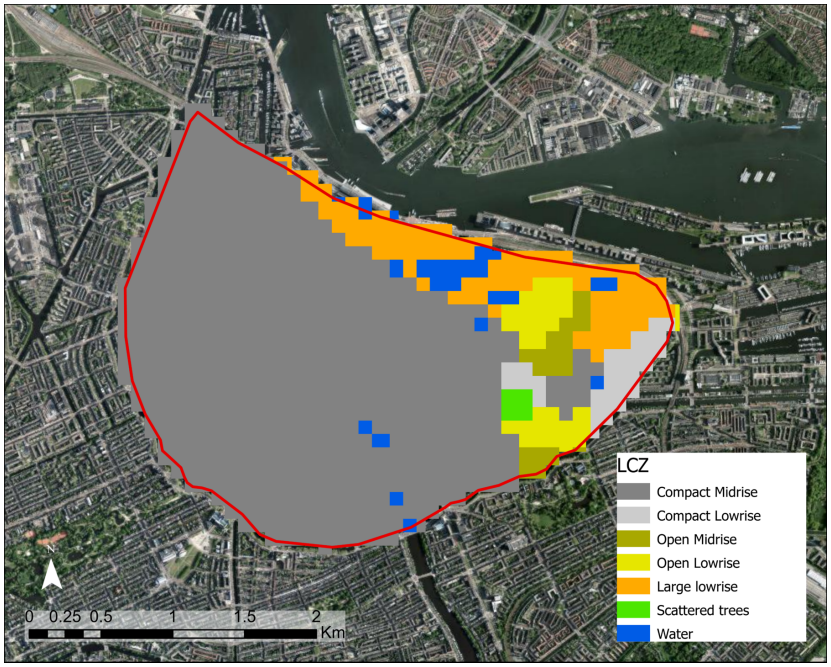

Figure 3.7. LCZ map of Amsterdam - resolution 100 m x 100 m - taken from project European LCZ map (WUDAPT) **[3.12]**.

- The total impervious surface is more than 70%.

In this study area, nested within the Singelgracht boundaries, the 74.4% of the soil surface is characterized by paved surface (*Built-Up*), the 21.4% by *Water* and the 4.2% by *Green*.

3.3 Land Surface Temperature

3.3.1 Flux Tower data

The MAQ station in Amsterdam records radiative flux data, as described in Section 3.1. According to the Stefan–Boltzmann law, reported in Equation 4.11, the outgoing longwave radiation emitted by a surface is a function of its surface temperature. Since the FT station measures all four radiative components, including the outgoing longwave radiation, this relationship allows the *LST* at the FT location to be estimated. This *LST* dataset is continuuos in time, available at hourly resolution (if no signal problems occur).

3.3.2 Landsat8 satellite imagery

Satellite-based *LST* data from Landsat8 (31 m x 31 m resolution) were used to calibrate and validate the energy-water balance model. Landsat 8 *LST* imagery

was accessed via USGS Earth Explorer **[3.14]**, selecting the product OLI/TIRS C2 L1. The extraction and processing of *LST* followed established workflows for satellite-derived surface temperatures using QGIS tools **[3.15]**. This process estimates Land Surface Temperature (LST) from Landsat-8 imagery using QGIS, following several key steps:

i) calculation of Top-of-Atmosphere (TOA) spectral radiance using the RADIANCE_MULT and RADIANCE_ADD coefficients from the metadata file;

ii) conversion of radiance to Brightness Temperature using the thermal constants K1 and K2;

iii) computation of the NDVI using bands 4 and 5;

iv) derivation of the Proportion of Vegetation (POV) by normalizing NDVI values;

v) calculation of land surface emissivity based on POV;

vi) final estimation of *LST* by correcting the Brightness Temperature with emissivity. The result is clipped to the Area of Interest and styled for cartographic visualization.

Raw data resolution is about 31 m x 31 m, but to be consistent with the model scale (100 m x 100 m), so data were reshaped trough bilinear interpolation using GIS tools. The satellite Landsat8 overpasses the study area grid between 10:00 and 11:00 a.m. Nonetheless, not all acquisitions are suitable for deriving *LST*, as the presence of cloud cover severely affects data quality. This is because the satellite sensors intercept the signal from the first interfering surface, which can be either the land surface or the cloud layer. On cloudy days, therefore, the retrieved signal corresponds to cloud-top properties rather than land surface characteristics, and such images are not considered for analysis.

Satellite observations from Landsat8 provide spatially distributed maps of *LST*, but only for a limited number of days per year and typically during morning overpasses. The *LST* derived from flux measurements, instead, is continuous in time and available at an hourly temporal resolution, although it refers to a single point location.

References

[**3.1**] StatLine and Urbistat. *StatLine / Urbistat database*. https://www.urbistat.com. Accessed: Sep 2025. 2023.

[**3.2**] Kadaster. *PDOK-TOP10*. https://www.pdok.nl. Accessed: Apr 2025. 2025.

[**3.3**] M. C. Peel, B. L. Finlayson, and T. A. McMahon. "Updated world map of the Köppen-Geiger climate classification". In: *Hydrology and Earth System Sciences* 11.5 (2007), pp. 1633–1644. DOI: 10.5194/hess-11-1633-2007.

[**3.4**] I. Manola, G. Steeneveld, R. Uijlenhoet, and A.A.M. Holtslag. "Analysis of urban rainfall from hourly to seasonal scales using high-resolution radar observations in the Netherlands". In: *International Journal of Climatology* 40.2 (2020), pp. 822–840. DOI: 10.1002/joc.6241.

[**3.5**] M. Dirksen, W. H. Knap, G. Steeneveld, A.A.M. Holtslag, and A.M.G. Tank. "Downscaling daily air-temperature measurements in the Netherlands". In: *Theoretical and Applied Climatology* 142.1-2 (2020), pp. 751–767. DOI: 10.1007/s00704-020-03313-1.

[**3.6**] G. Steeneveld, S. van der Horst, and B. Heusinkveld. "Observing the surface radiation and energy balance, carbon dioxide and methane fluxes over the city centre of Amsterdam". In: *EGU general assembly conference abstracts*. 2020, p. 1547.

[**3.7**] D. Baldocchi, E. Falge, L. Gu, R. Olson, D. Hollinger, S. Running, P. Anthoni, C. Bernhofer, K. Davis, R. Evans, J. Fuentes, A. Goldstein, G. Katul, B. Law, X. Lee, Y. Malhi, T. Meyers, W. Munger, W. Oechel, U.K.T. Paw, K. Pilegaard, H.P. Schmid, R. Valentini, S. Verma, T. Vesala, K. Wilson, and S. Wofsy. "FLUXNET: A New Tool to Study the Temporal and Spatial Variability of Ecosystem-Scale Carbon Dioxide, Water Vapor, and Energy Flux Densities". In: *Bulletin of the American Meteorological Society* 82.11 (2001), pp. 2415–2434. DOI: 10.1175/1520-0477(2001)082<2415:FANTTS>2.3.CO;2.

[**3.8**] A. Barrios-Barocio, O. Peralta, C.A. Ochoa-Moya, E. Luyando, and M. Espinosa-Fuentes. "Heat wave: a new characterization in terms of energy". In: *Frontiers in Environmental Science* 12 (2024), pp. 1–9. DOI: 10.3389/fenvs.2024.1474608.

[3.9] N. Kljun, P. Calanca, M. W. Rotach, and H. P. Schmid. "A simple parameterisation for flux footprint predictions". In: *Boundary-Layer Meteorology* 112.3 (2004), pp. 503–523. DOI: 10.1023/B:BOUN.0000030653.71031.96.

[3.10] Wageningen University. *LGN2022 - Landelijk Grondgebruik Nederland 2022*. https://lgn.nl/. Accessed: Apr 2025. 2025.

[3.11] I. D. Stewart and T. R. Oke. "Local climate zones for urban temperature studies". In: *Bulletin of the American Meteorological Society* 93.12 (2012), pp. 1879–1900. DOI: 10.1175/BAMS-D-11-00019.1.

[3.12] B. Bechtel, P.J. Alexander, C. Beck, J. Böhner, O. Brousse, J. Ching, M. Demuzere, C. Fonte, T. Gál, J. Hidalgo, P. Hoffmann, A. Middel, G. Mills, C. Ren, L. See, P. Sismanidis, M.L. Verdonck, G. Xu, and Y. Xu. "Generating WUDAPT Level 0 data – Current status of production and evaluation". In: *Urban Climate* 27 (2019), pp. 24–45. DOI: 10.1016/j.uclim.2018.10.001.

[3.13] M. Demuzere, B. Bechtel, A. Middel, and G. Mills. "Mapping Europe into local climate zones". In: *PLoS ONE* 14.4 (2019), pp. 1–2. DOI: 10.1371/journal.pone.0214474.

[3.14] USGS - Earth Explorer. https://earthexplorer.usgs.gov. Accessed: Apr 2025. 2025.

[3.15] R. Saputra. *Mapping Land Surface Temperature (LST) using Landsat-8 Imagery in ArcMAP*. https://riski-saputra.medium.com/mapping-land-surface-temperature-lst-using-landsat-8-imagery-in-arcmap-99bd64f2c3fa. Accessed: Apr 2025. 2025.

Chapter 4

Model

4.1 *SWEB* Model and *LST* assessment

The Surface Water Energy Balance ($SWEB$) model couples a hydrological module with an energy balance module. The model was developed in Matlab ® environment by Climate-Lab staff of Politecnico di Milano, using Milano as pilot case [**4.1**]. The Water-Energy Budget of the system, which accounts for soil, vegetation, and the atmospheric layer, is solved by determining the Land Surface Temperature (LST) that closes the system of equations for each cell of the basin surface. The model was applied separately for each land cover type, yielding a specific LST value for each. Finally, an average LST was assigned to each cell by weighting the contributions according to the corresponding land cover fractions (Equations 4.1, 4.2). The aim of the model is to simulate energy and water fluxes and get the output using input data, which can be obtained from AWS or remote-sensing data at mesoscale. The $SWEB$ model takes the precipitation, first layer atmosphere air temperature, atmospheric pressure (assumed as constant, for Amsterdam P_{atm} = 1012hPa and for Milano P_{atm} = 1014hPa), near surface wind speed, and radiation as input.

For Amsterdam case study, all four radiation components are available, namely incoming and outgoing shortwave radiation (SW_{in} and SW_{out}) and incoming and outgoing longwave radiation (LW_{in} and LW_{out}). Different land use types are included (Built-up, Green, Water), with a single soil layer. LST and net radiation R_n, Latent LE and Sensible H heat, and soil water content W are solved separately for each land use type. Then LST, W, LE and H are solved for the whole grid with the lumped result. All the dynamics here analyzed are constrained within the UBL (urban boundary layer), at mesoscale [**4.2**].

The $SWEB$ model follows the same general principles for both study cases,

but includes specific features tailored to the **Milano** and **Amsterdam**.

The model runs as spatially explicit, grid-based semi-distributed model (500 m x 500 m resolution for Milano and 100 m x 100 m resolution for Amsterdam). Lateral fluxes between consecutive cells are not simulated. Time is discretized in daily/hourly frames, for every time step of the simulation period. Control period is 2010-2022 for Milano and 2020-2024 summers for Amsterdam. The $SWEB$ model here proposed assess the LST for each cell of the domain for each soil type (i.e. Built-up, Green and Water) separately. The model solves the scheme independently for each soil type, treating them as three separate basins. For each grid cell, LST is then computed as a weighted average of the LST values obtained for each basin type, according to the fraction of each soil type within the cell. For Milano, the Vegetation Fraction (VF [0-1]) parameter was adopted. Each cell of the domain is thus characterized by the percentage of green areas (VF), while the remaining fraction ($1 - VF$) represents impervious urban surfaces. No water bodies are considered in Milano modeling.

$$LST = LST_g \cdot VF + LST_b \cdot (1 - VF) \tag{4.1}$$

For Amsterdam, three metrics have been adopted that are: B_f: Built-up fraction [0-1], G_f: Green Fraction [0-1], which has the same meaning as VF, and W_f: Water fraction [0-1].

$$LST = LST_g \cdot G_f + LST_b \cdot B_f + LST_w \cdot W_f \tag{4.2}$$

The subscript b is referred to built-up variables, the subscript g is referred to green (vegetation) variables, while the subscript w is referred to water variables.

The model flow scheme is presented in Figure 4.1, and the parameters are reported in Tables 4.2 and 4.1.

Parameter	**Symbol**	***Green***	***Built-up***	**Ref.**
Bulk exchange coefficient for H	$C_{H,g}$, $C_{H,b}$	0.02	0.05	*Cal.*
Soil permeability	k_g k_b	2	6	*Cal*
Wilting point	θ_{WP}	0.08		[**4.3**]
Field capacity	θ_{FC}	0.4		[**4.3**]
Albedo	α_g, α_g	0.7	0.1	[**4.4**]

Table 4.1. *SWE* balance model parameters for *Green Basin* and *Built-up Basin*. The values were either sourced from the literature or derived through calibration to mimic LST.

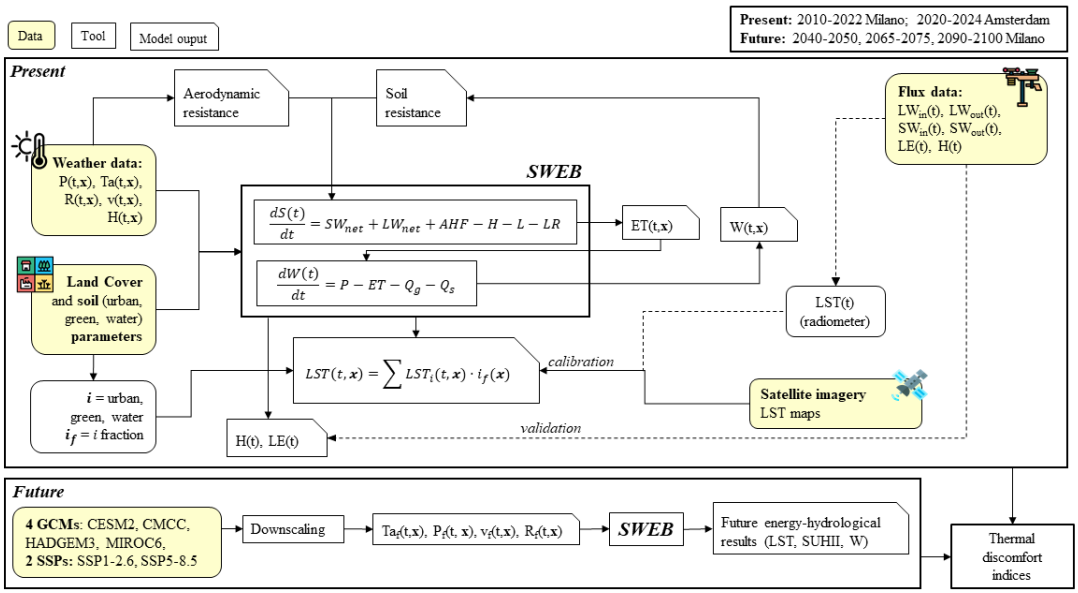

Figure 4.1. *SWEB* model framework. The model consists of an energy balance module and a water balance module. For each time step and grid cell, the model computes the land surface temperature (LST_i) for each soil type i. A single LST value is then assigned to each cell by averaging LST_i weighted by the corresponding soil-type fractions (i_f). For model calibration, simulated LST values were compared with satellite-derived LST; for the Amsterdam case study, LST estimates derived from FT records were also used.

Parameter	Symbol	*Green*	*Built-up*	*Water*
Bulk exchange coefficient for H	$C_{H,g}$, $C_{H,b}$, $C_{H,w}$	0.0097	0.031	0.002
Bulk exchange coefficient for LE	$C_{LE,g}$, $C_{LE,b}$, $C_{LE,w}$	0.005	0.0055	0.002
Density	ρ_g, ρ_b, ρ_w $[\mathrm{kgm}^{-3}]$	1500	2400	1000
Heat capacity	c_g, c_b, c_w $[\mathrm{J(Kg°C)}^{-1}]$	2000	62000	4186
Albedo	α_g, α_b, α_w	0.6	0.1	0.9
Soil permeability	k_g k_u	2	6	-

Table 4.2. *SWEB* model parameters for *Green Basin*, *Built-up Basin* and *Water Basin*. The values were either sourced from the literature or derived through calibration to mimic LST.

Parameter	Symbol	U.M.	Value
Air density	ρ_a	$\mathrm{kg\,m^{-3}}$	1.293
Kármán constant	k	–	0.41
Stefan–Boltzmann constant	σ	$\mathrm{W\,m^{-2}\,K^{-4}}$	5.67×10^{-8}
Latent heat of vaporization	L_v	$\mathrm{J\,kg^{-1}}$	2.45×10^{6}
Molecular weight ratio (water vapor / dry air)	MW	–	0.622
Specific heat capacity of air	c_p	$\mathrm{J\,kg^{-1}\,K^{-1}}$	1030
Minimum stomatal resistance	$r_{s,min}$	$\mathrm{ms^{-2}}$	90

Table 4.3. Constant parameters used in the *SWEB* model.

4.1.1 Hydrological model

The hydrological module consists in a semi-distributed model based upon the application of a mass conservation equation for soil water content. The hydrological module takes origin from Poli-Hydro [**4.5**], which has already been successfully applied in different contexts to simulate the response of the water budget under future climate conditions, including lake hydrodynamics [**4.6**], hydropower production [**4.7**], and pasture dynamics [**4.8**]. Here the water balance equation, applied to each cell of the study area, is written as:

$$\frac{dW(t)}{dt} = P - ET - Q_g - Q_s \tag{4.3}$$

Where, W [mm] is soil water content, P is liquid rainfall, ET is actual evapotranspiration, Q_g is groundwater discharge, Q_s is the surface discharge, cumulated during the time step dt. Each factor in the budget was calculated daily/hourly for each grid cell of the study area independently (vertical fluxes, only), as depicted in Figure 4.2. For Milano, the u.m. is [mmd^{-1}], for Amsterdam instead [mmh^{-1}].

Groundwater discharge The equation for groundwater discharge based on soil hydraulic conductivity and water content as follows:

$$Q_g = K \cdot \left(\frac{W}{W_{max}}\right)^k \tag{4.4}$$

K is saturated permeability, and k is a power exponent. W_{max} is greatest potential soil storage. W_{max} represents the maximum soil water storage capacity. In this study, W_{max} was estimated using the CN-SCS method [**4.9**]. For green areas, K was determined based on the average soil properties of the natural terrain in Milano and Amsterdam. For urban areas, K was instead interpreted as an effective sewer capacity coefficient. The term Q_g represents different processes depending on land cover: in green areas it corresponds to infiltration into the soil, whereas in built-up areas it represents runoff directed to the sewer system. In Amsterdam, stormwater and wastewater are managed through separate systems; therefore, rainwater can be directly discharged into surface water bodies such as rivers, canals, or ponds. Milano has a sewer network with an extension of 2085 km, and accordingly all surface waters are efficiently drained. Waterproof surfaces are either connected to the drainage network, or overflow to the neighboring natural surface. One may assume that hydraulic conductivity K is very high, because urban surface drainage systems are highly efficient in capturing rainwater, and

directing it toward the sewer system or water bodies. Percolating waters on impervious surfaces quickly reach the sewer collection system, minimizing their horizontal flow or lateral exchange with adjacent cells. Indeed, vertical flows are more significant than horizontal ones.

Sub-superficial discharge Sub-superficial discharge flow Q_s occurs only for saturated soil.

$$\begin{cases} Q_s = W(t+dt) - W_{max} \text{ if } W(t+dt) - W_{max} > W_{max} \\ Q_s = 0 \text{ if } W(t+dt) - W_{max} <= W_{max} \end{cases} \tag{4.5}$$

Evapotranspiration The actual evapotranspiration ET is estimated based on the latent heat flux LE (Equation 4.7), which influences the energy balance. In *Built-up* and *Water* areas, only evaporation occurs, whereas in *Green* areas transpiration also takes place due to the presence of trees and other tall vegetation. Evaporation over water surfaces is relatively constant, while over paved surfaces it is limited by water availability, for instance following rainfall events when moisture is present on the ground.

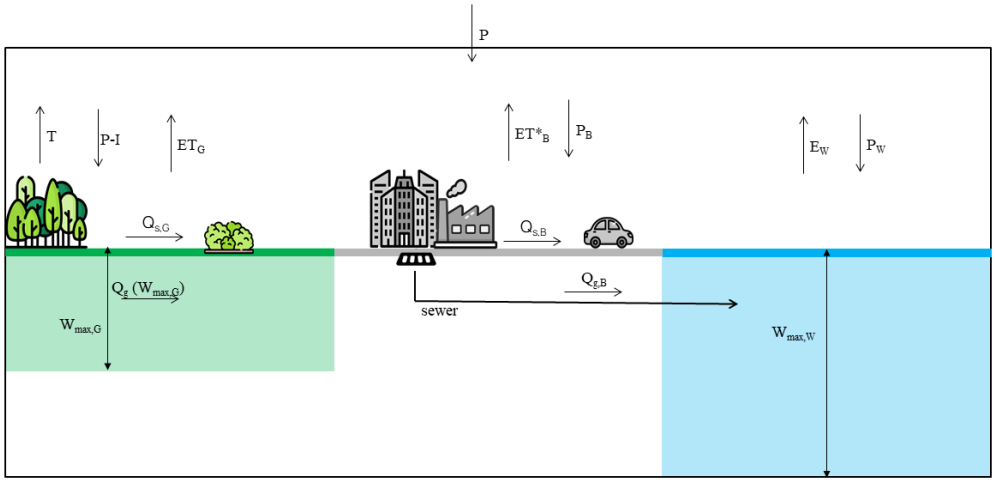

Figure 4.2. Water balance scheme for *Green Basin*, *Built-up Basin* and *Water Basin*

4.1.2 Energy model

Surface Energy Balance (SEB) is a key component of any model aiming to simulate dynamical and thermodynamical patterns above surface [**4.2**]. The energy

balance module is based upon vertical balance of heat fluxes [**4.10**, **4.11**]. Land surface energy balance derives from the first law of thermodynamics. It is based on the principle of energy conservation, according to which the total energy of a system is preserved even if energy transformations occur:

$$\frac{dS(t)}{dt} = SW_{net} + LW_{net} + AHF - G - H - LE - LR \tag{4.6}$$

Where SW_{net} is the shortwave net radiation, LW_{net} is the longwave net radiation (their sum defines the net radiation R_n), AHF is the anthropogenic heat flux, G is soil heat flux, H is sensible heat and LE is latent heat flux and LR is the liquid rainfall term. Water budget equation (Eq. 4.3) and Energy balance equation (Eq. 4.6) are linked trough evapotranspiration ET, since it depends on latent heat LE and latent heat of vaporization λ [**4.12**] and water density ρ_w:

$$LE = \lambda \rho_w ET \tag{4.7}$$

The so calculated ET contributes to the water budget (Equation 4.3).

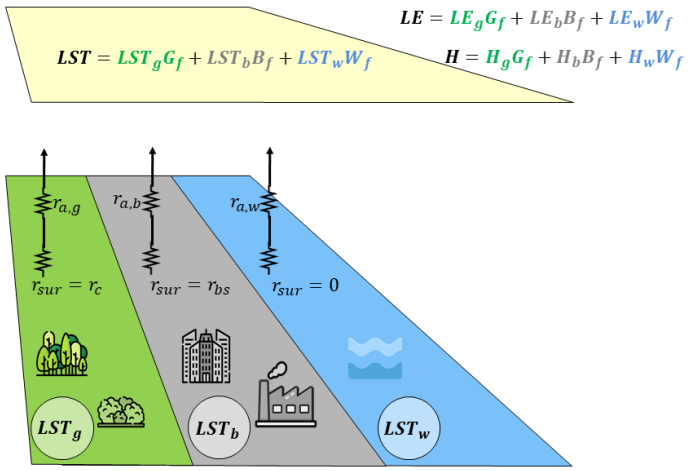

Figure 4.3. Definition of Heat Fluxes and LST through the Energy Balance Scheme for the *Green Basin*, *Built-up Basin* and *Water Basin*.

Soil heat flux Traditional equation for soil heart flux, in the simplified 1D form, is the following:

$$G = \kappa \frac{dT_s}{dz} \tag{4.8}$$

With κ is the soil heat conductivity, dT_s is the difference in temperature between LST and soil temperature at depth dz. The soil heat flux G shapes the hourly net radiation. While the day–night differences in the energy balance of G are consistent, they tend to average out to near zero in the seasonal energy balance [**4.13**]. For Milano case study, since the model works at a daily scale, and the primary outputs are seasonal averages, G could be considered negligible. Soil heat flux plays an important role on SEB for arid bare soil [**4.14**], where G values could be reach 100% of nighttime net radiation and 60% of daytime net radiation. For water bodies, G could be neglected [**4.15**], for green areas, G could reach non-negligible values mainly in Summer. A study carried out in Netherland's grasslands has shown that average summer soil heat flux is about $G = 8\text{Wm}^{-2}$ [**4.16**]. Compared the other seasons, G has higher values, but they are however a minor contribute in the SEB. At urban context, G is usually not measured and hard to determine [**4.2**].For this reason, in this simulation, the heat released from the ground is not treated as soil heat flux G; instead, it is included in the heat storage term dS, which represents the amount of heat absorbed (positive) or released (negative) by the ground within a given time step dt. This contribution plays a more significant role in built-up areas, while it is negligible in green spaces and water bodies.

Radiation The net Radiation R_n was assessed as the difference between incoming and outcoming solar (shortwave) radiation SW and the longwave radiation LW.

$$R_n = SW_{in} - SW_{out} + LW_{in} - LW_{out} \tag{4.9}$$

The longwave radiation LW is directly linked to air temperature T_a and Land Surface Temperature LST.

$$LW_{in} = \varepsilon_a \cdot \sigma \cdot T_a^4 \tag{4.10}$$

$$LW_{out} = \varepsilon \cdot \sigma \cdot LST^4 \tag{4.11}$$

Where T_a and LST are the air and surface temperature, respectively, expressed in K, and ε refers to emissivity of air [Equation 4.12] and surface. Values are usually included between [0.94-0.98].

$$\varepsilon_a = 1.24 \cdot \left(\frac{e_a}{T_a}\right)^{\frac{1}{7}} \tag{4.12}$$

According the [**4.17**] approach, during cloudy days, the air emissivity ε_a is increased by 22% [**4.18**], so:

$$\varepsilon_a = 1.22 \cdot \left(1.24 \cdot \left(\frac{e_a}{T_a}\right)^{\frac{1}{7}}\right) \tag{4.13}$$

Trough 4.11 it was also possible to assess the LST recorded at FT, as written in the Sections 3.1 and 3.3.

For Milano, only global radiation R_g records were available. To assess solar net radiation, an albedo (α) value was introduced and used as model parameter.

$$R_n = R_g \cdot (1 - \alpha) \tag{4.14}$$

In urban patterns, α is influenced by factors such as the height of structures, building density and brightness, that is, typically, walls are bright and roads tend to be darker [**4.19**]. The diffuse highly reflective building facades can reflect the incident sunlight into an open area when there are no obstructions, so the urban albedo could reach very high values [**4.4**]. α is a variable term within a certain range that depends on the zenith angle and the actual evapotranspiration. However, this study considers an average constant value for the $Built-Up$ surface (and two other values for $Green$ and $Water$ basins), consistent with available literature results.

Anthropogenic Heat Flux Anthropogenic Heat Flux (AHF) is the heat flow generated directly by human activities and released into the environment. This heat comes from various sources such as energy production and consumption (power plants, vehicles, industrial plants, heating and air conditioning of buildings), urbanization and infrastructure (heat-absorbing urban materials, transportation), and industrial processes that produce waste heat [**4.20**]. Waste heat produced by human activities is one contributor to the urban heat island [**4.21**]. Direct measurement of AHF is challenging due to the absence of specialized sensors; however, it can be assessed using parametric estimation methods. In this study, AHF values were assessed according the LCZ approach [**4.22**]. In the Milano case study, AHF was not considered, whereas it was included in the Amsterdam analysis. The corresponding values were derived from the LCZ map provided by the WUDAPT project, as described in Section 3.2.

Liquid Rainfall term The rainfall term LR is effective only during precipitation events and it is modeled assuming that rain has the same temperature as

the air. Once it reaches the ground, it is assumed to immediately reach thermal equilibrium with the soil.

$$LR = \rho_w c_w w(T_r - LST) \tag{4.15}$$

Where:

- $\rho_w[\mathrm{Kgm}^3], c_w[\mathrm{J(Kg^\circ C)}^{-1}]$ are density and specific heat of water;
- $w[\mathrm{ms}^{-1}]$ is the rainfall rate;
- $T_r[^\circ\mathrm{C}]$ is the rain temperature, considered equal to air temperature.

This term is more commonly used in glaciological studies and is relatively uncommon in urban-scale applications. In snow and ice environments, liquid rainfall generally has a warming effect, as it transfers heat to the surface. In contrast, in urban environments during summer, the effect is reversed: the presence of water promotes surface cooling. Following a precipitation event, part of the stormwater returns to the atmosphere through evaporation, enhancing latent heat fluxes and reducing surface temperature. To account for this cooling contribution, the LR term was included in the model formulation. Sensitivity analysis confirms that incorporating this term improves model performance.

The problem with rainy days is that signal reception isn't always as optimal as usual, which means the stream data might be corrupted. However, its contribution is generally negligible, as it typically assumes low values (approximately 3–10 $\mathrm{W\,m^{-2}}$) during rainfall events.

Sensible and Latent heat The sensible and latent heat fluxes are expressed as:

$$H = \frac{(\rho_a c_p)}{r_a} \cdot (LST - T_a) \tag{4.16}$$

$$LE = \frac{\rho_a \cdot MW \cdot \lambda}{(r_a + r_s)} \cdot \frac{(e^* - e_a)}{p} \tag{4.17}$$

where r_a and r_s are the aerodynamic and surface resistances. These are typically derived from physically based formulations, such as the Thom model for r_a [**4.23**, **4.24**] and the Jarvis approach for r_s [**4.25**], with additional parameterizations depending on surface type [**4.26**, **4.3**]. Vapor pressures are estimated using the Tetens equation [**4.27**], following [**4.28**].

The remaining parameters are defined as follows: $MW = 0.622$ is the ratio between the molecular weight of water vapor and dry air; $\lambda = 2.45 \times 10^6$ J kg^{-1} is the latent heat of vaporization; $\rho_a = 1.293$ kg m^{-3} is the air density; and p is the atmospheric pressure (assumed as constant, for Amsterdam $P_{atm} = 1012$ hPa and for Milano $P_{atm} = 1014$ hPa).

Due to the limited availability of detailed input parameters, a bulk approach was adopted [**4.29**], in which the resistances are incorporated into bulk exchange coefficients:

$$C_H = \frac{1}{r_a \cdot v} \tag{4.18}$$

$$C_{LE} = \frac{1}{r_a \cdot v + r_s} \tag{4.19}$$

Thus, Equations 4.16 and 4.17 can be rewritten as:

$$H = \rho_a \cdot c_p \cdot v \cdot C_H \cdot (LST - T_a) \tag{4.20}$$

$$LE = MW \cdot \rho_a \cdot L_v \cdot v \cdot C_{LE} \cdot \frac{e^* - e_a}{p} \tag{4.21}$$

Importantly, the original formulations of r_a and r_s were first used to derive initial estimates based on literature values. These estimates provided physically consistent starting points, which were then embedded into the definitions of C_H and C_{LE}. The bulk coefficients were subsequently calibrated against observations, ensuring both physical consistency and model adaptability.

Bulk coefficients depend on land cover. For Amsterdam, five coefficients are defined ($C_{H,g}$, $C_{H,b}$, $C_{H,w} = C_{LE,w}$, $C_{LE,g}$, $C_{LE,b}$), while for Milano C_H is assumed constant and C_{LE} depends on soil moisture. When water is unavailable, latent heat flux is suppressed, preventing evapotranspiration.

Heat storage Equation 4.6 refers to the heat storage. For Milano this equation close to zero, assuming that negligible energy is stored during the day. For Amsterdam, since the time scale is hourly, at each step dt there is an accumulation term dS. At the end of the day, the integration of this term is zero, as demonstrated also in Section 5.3.4. In this study, G is directly included in the energy storage term dS/dt. As shown in Figure 5.40, an accumulation of energy storage can be observed during the day. Overall, throughout the day, all net solar energy is converted into sensible heat (about 65%) and latent heat (about 32%),

with residuals accounting for roughly 3%. There is an accumulation of energy during the day, when solar radiation increases, and a release during the latter part of the day, when solar radiation decreases. This term also incorporates the energy content of the ground, since G is not directly measured. It represents the release of energy from the ground to the surface and is therefore included in the definition of LST.

4.2 Definition of *LST* and *SUHII* assessment

The Surface Water-Energy balance system (Equations 4.6, 4.5 and 4.7) is solved for the closing value of LST, for each cell of the basin surface, at daily scale for Milano and hourly scale for Amsterdam. A real-valued function with solution $f(x) = 0$ can be approximated using Newton-Raphson method. When adopting this method, different possible atmospheric and soil coverage conditions were considered, and the function only has one real solution. Once the model has completed one iteration for each basin type, it produces a value of LST_g and LST_g for every cell within the Milano domain, for each day of the simulation, and LST_b, LST_g and LST_w for Amsterdam for each hour of simulation. To assess a proper value of LST, the results of LST are then averaged by the soil type fraction of the cell, hence using Equation 4.1 for Milano and Equation 4.2 for Amsterdam.

In natural environments, a larger share of the available energy is used for evaporation and transpiration, whereas in urban environments it is predominantly converted into sensible heat. This difference in energy partitioning leads to variations in LST and underlies the definition of the Surface Urban Heat Island (SUHI). SUHI is the phenomenon whereby urban surfaces, indicated by LST, are warmer than the surrounding rural areas [**4.30**]. It can be quantitatively defined through the Surface Urban Heat Island Intensity ($SUHII$), i.e., the difference in LST between different surface types. This indicator provides insight into the extent to which built-up areas influence surface temperature and associated heat fluxes, as well as the potential of blue and green spaces to mitigate these effects.

4.3 Climate projections and future scenarios

For Milano case study, both the baseline scenario and the projected future scenario were analyzed and compared. To simulate future projections of LST it was necessary to use climatic projections of precipitation (P), air temperature

(T_a) and near surface wind speed (v). In order to properly manage the uncertainty/variability of future climate projections, as due to the inherent noise in simulations from different General Circulation Models (GCMs), and to different potential Shared-Socio Economic Pathways (SSPs), I used the projections from four GCMs, and two IPCC AR6 SSPs. Use of more GCMs allowed to explore a wide range of climate sensitivity.

Model	**Research institute**	**Country**	**Grid size**	**Layers**	***Ref.***
CESM2	National Center for Atmosphere Research	USA	1.25 °x 0.9 °	32	[**4.31**]
CMCC	Centro Euro-Mediterraneo sui Cambiamenti Climatici	IT	1 °x 1 °	30	[**4.32**]
HADGEM3	Headley Center Global Environment	UK	0.25 °x 0.25 °	85	[**4.33**]
MIROC6	Center for Climate System Research	JP	1 °x 1 °	62	[**4.34**]

Table 4.4. Adopted GCMs and features.

In order to properly manage the uncertainty/variability of future climate projections, as due to the inherent noise in simulations from different General Circulation Models (GCMs), and to different potential Shared-Socio Economic Pathways (SSPs), we used the projections from four GCMs, and four IPCC AR6 SSPs.

T_a and P data from each GCM × SSP combination were downscaled using a stochastic approach [**4.35**, **4.36**]. u data were downscaled trough a specific correction factor [**4.37**]. Solar radiation was calculated on a distributed basis (i.e. in every cell of the model), based on theoretical extra-terrestrial radiation [**4.38**], and corrected by a CSI factor.

The downscaling process was applied to have a series of T_a, R, P and v data in each AWS, then these data were spatialized in the entire domain with Kriging approach, using same correlation coefficients obtained in the baseline scenario (Figure 2.2).

Future projections were done for the period 2023-2100. Here, analysis was done for three decades, the first at the middle of the XXI century, 2040-2050 (ST), the second a middle-term 2065-2047 (MT) and the last one at end of the century, 2090-2100 (LT).

CMIP6 model simulations [**4.39**] were performed using a combination of the representative concentration pathways (RCP), and the shared socioeconomic pathways (SSP) [**4.40**]. The simulations are named after the SSP levels and the related RCP values, since SSPs often correspond to distinct radiative forcing values

[**4.41**]. The five available scenarios are SSP1-1.9, SSP1-2.6, SSP2-4.5, SSP3-7.0 and SSP5-8.5. They were launched in 2015, and include scenarios where GHG emissions are high to very high (SSP3-7.0 and SSP5-8.5), and CO_2 emissions roughly double from current levels by 2100 and 2050, respectively. They also include a scenario where GHG emissions are intermediate (SSP2-4.5) and CO_2 emissions stay at current levels until the middle of the century. Finally, they include scenarios where GHG emissions are low to very low, and CO_2 emissions decline to net zero around or after 2050 (SSP1-1.9 and SSP1-2.6) [**4.42**].

The Shared Socioeconomic Pathways (SSPs) were developed to complement the Representative Concentration Pathways (RCPs) and are based on five narratives describing alternative socio-economic futures. They represent different potential trajectories of future societies, taking into account investments in education, healthcare, and energy development.

In this study, scenarios SSP1-2.6, and SSP5-8.5 have been considered, because these two scenarios represent the opposite ends of the spectrum in term of potential evolution of the future climate, i.e. the best case scenario and the worst case scenario.

SSP1-2.6: Sustainable Development. This scenario is the most optimistic. Its application to existing GCMs results in an increase in T_a of less than $+2°C$, making it suitable for analyses aimed at this target. According to this scenario, only minor land-use changes are expected, accompanied by significant mitigation efforts. SSP1-2.6 projects a radiative forcing increase of $+2.6\,W/m^2$ by 2100.

SSP5-8.5: Fossil Fuel Based Development. This scenario represents the most extreme pathway. SSP5-8.5 projects a radiative forcing increase of $+8.5\,W/m^2$ by 2100, reflecting high reliance on fossil fuels and limited mitigation efforts.

4.4 Heat Wave definition

According the WMO, an heat wave (HW) occurs when at least six consecutive days with maximum temperature is higher than the 90°percentile of the reference thirty-year period, in this study 1991-2020. To assess the HW frequency, the 90°percentile of the maximum temperature for 1991-2020 period was evaluated for the two European cities. For Milano, daily maximum temperature data from the Brera Observatory in Milan were used for the period 1991–2022. The Brera Observatory, founded in 1764 by Roger Boscovich and Giuseppe Lodovico Lagrangia in Palazzo Brera, is among the oldest scientific institutions in Italy and is currently part of INAF. The location of Brera AWS is shown in Figure 2.2 and the coordinates in the Table 2.1. The analysis computed the average summer maximum temperatures over the 30-year period and applied the 90th percentile as a reference threshold to identify exceptionally high values. For Amsterdam, a similar analysis was carried out for Amsterdam using data from KNMI Station 240 at Schiphol Airport. This station, operated by the Royal Netherlands Meteorological Institute, delivers essential meteorological observations for aviation safety and atmospheric research. Daily maximum temperature data for 1991–2022 were processed to compute the average summer maximum temperatures over the 30-year period, and the 90th percentile was applied as a reference threshold, following the same procedure adopted for the Brera Observatory.

It's important to investigate into HW occurrence since during these days, the energy budget is unbalanced toward sensible heat **[4.43]**, causing a greater increase in LST and in perceived air temperatures. So, this indicator, that will be better discussed in the Section 5.4, is strongly linked to the health stress. Heat waves are driven by large-scale climatic conditions, while the SUHI effect locally amplifies their intensity and duration, leading to higher thermal stress and increased health risks in urban areas compared to surrounding rural regions.

According historical records and HW definition, threshold air temperatures for the Heat Wave assessment (Figure 4.4) are:

- 30.90 °C for Milano;
- 23.25 °C for Amsterdam.

These values will be used to assess heat waves events in the two cities (Section 5.1.5 for Milano and Section 5.3.5 for Amsterdam) and to investigate their influence on LST.

Year	Ta [°C]
1991	20.60
1992	22.22
1993	19.76
1994	22.30
1995	22.56
1996	20.39
1997	22.48
1998	19.90
1999	21.55
2000	20.14
2001	21.69
2002	21.50
2003	23.35
2004	21.62
2005	21.15
2006	23.17
2007	21.22
2008	21.46
2009	22.26
2010	22.09
2011	20.29
2012	21.09
2013	22.05
2014	21.76
2015	21.93
2016	21.84
2017	22.21
2018	23.80
2019	23.33
2020	22.83
1991-2020	**21.75**

Table 4.5. Average maximum summer air temperature in Amsterdam for the 1991–2020 reference period. Source: KNMI - Schiphol station.

2022 Heat Wave

The summer of 2022 was characterized by exceptionally high temperatures across northwestern Europe. The number of warm daytime events was extraordinarily large, particularly in southwestern regions. Maximum temperatures in western Europe reached values up to 10 °C above the typical summer averages. A distinctive feature of this unusually hot summer was the early onset of the first tropical day (i.e., a day with air temperature exceeding 30 °C). In several parts of Europe, the first tropical day occurred around mid-May, approximately one month ear-

Year	Ta [°C]
1991	30.58
1992	27.74
1993	26.45
1994	29.27
1995	27.11
1996	26.59
1997	26.66
1998	28.55
1999	27.47
2000	27.23
2001	27.93
2002	26.89
2003	31.92
2004	28.44
2005	28.24
2006	28.91
2007	28.85
2008	28.78
2009	30.46
2010	29.31
2011	28.96
2012	31.00
2013	29.36
2014	27.61
2015	30.91
2016	29.94
2017	30.92
2018	30.10
2019	30.71
2020	29.38
1991-2020	**28.95**

Table 4.6. Average maximum summer air temperature in Milano for the 1991–2020 reference period. Source: ARPA Lombardia - Brera station.

lier than usual. In June 2022, air temperatures were above average across most of Europe, with Italy being one of the most affected countries. In July 2022, a persistent high-pressure system developed over western Europe, bringing dry and sunny conditions. Combined with the advection of hot air masses from North Africa, this led to widespread heat wave conditions across western Europe. As a result, several days with air temperatures exceeding 40°C were recorded in the north-western part of the continent. Globally, increasingly high latitudes are also experiencing more extreme temperatures, including those exceeding 40°C [**4.44**].

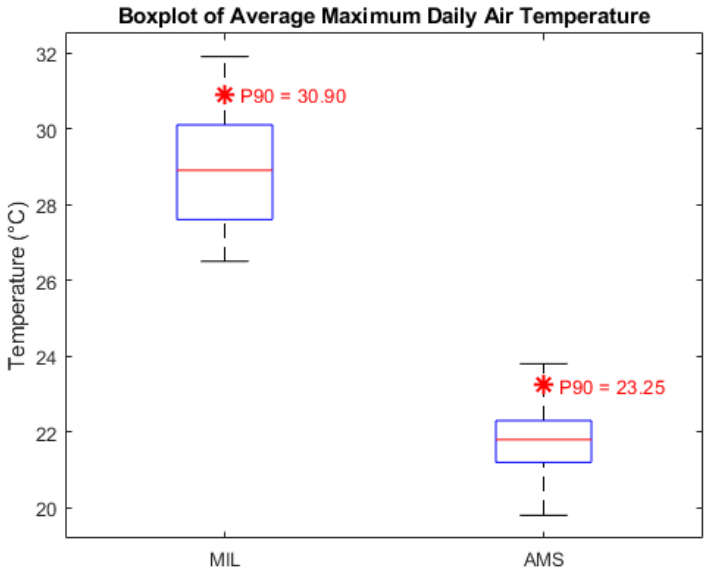

Figure 4.4. Boxplot and 90th percentile of average maximum summer air temperature in Milano **MIL** and Amsterdam **AMS**. Reference period: 1991–2020.

In August 2022, air temperatures remained above average throughout most of Europe. The anomalies were strongest over the far east of the continent and generally elevated in the west, although not as extreme as those observed earlier in the summer. The frequent occurrence of extreme temperatures, combined with a persistent lack of precipitation, was closely associated with the widespread drought that affected much of Europe during the summer of 2022 [**4.44**]. During the summer of 2022, numerous anomalies in warm daytime conditions were observed. Warm days are defined as those with maximum air temperatures exceeding the 90th percentile of values for the corresponding calendar day during the reference period (1991–2020) (Figure 4.5).

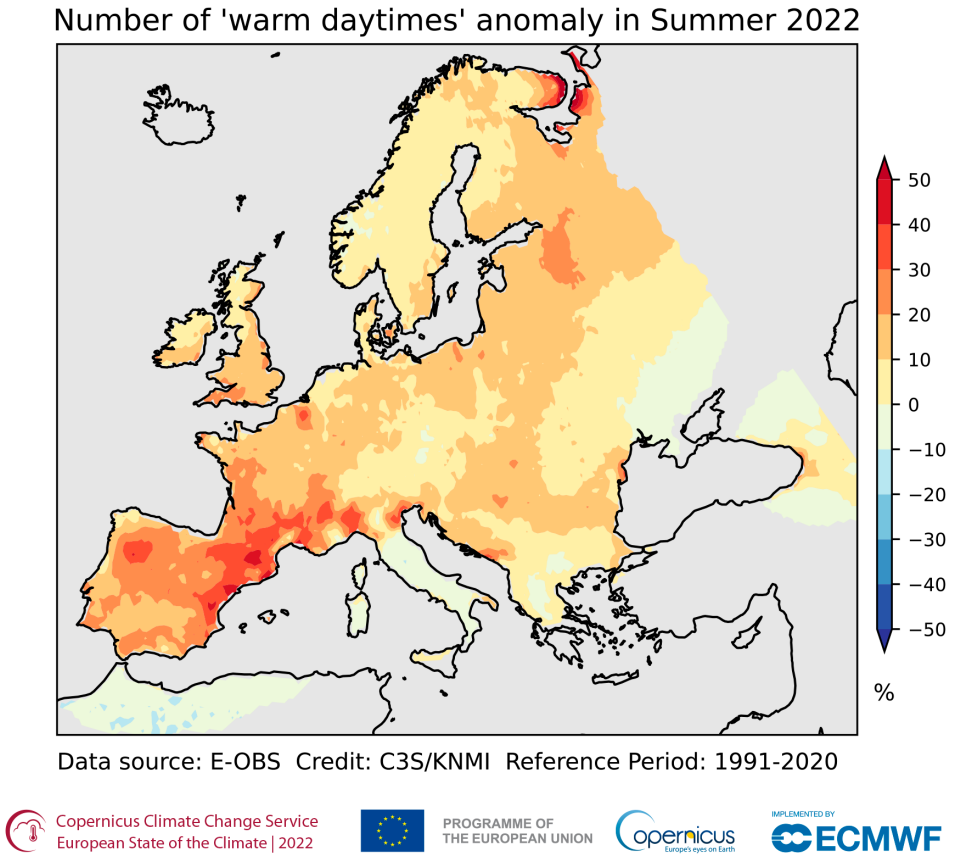

Figure 4.5. Warm daytimes anomaly [%] for summer (June-August) 2022, relative to the average for the 1991-2020 reference period. The image is taken from Copernicus report [**4.44**]. Data Source: E-OBS. Credit: KNMI/C3S/ECMWF

References

[**4.1**] S. Morgese, W. Zhang, F. Casale, and D. Bocchiola. "A Hydrological–Energy Balance Model to Assess Land Surface Temperature at the Urban Scale: The Case Study of Milano, Italy". In: *Meteorological Applications* 32.3 (2025). DOI: 10.1002/met.70069.

[**4.2**] M. Piringer, C. S. B. Grimmond, S. M. Joffre, P. Mestayer, D. R. Middleton, M. W. Rotach, A. Baklanov, K. De Ridder, J. Ferreira, E. Guilloteau, A. Karppinen, A. Martilli, V. Masson, and M. Tombrou. "Investigating the Surface Energy Balance in Urban Areas — Recent Advances and Future Needs". In: *Urban Air Quality — Recent Advances* (2002), pp. 1–16. DOI: 10.1007/978-94-010-0312-4_1.

[**4.3**] C. Corbari, D.S. Jovanovic, L. Nardella, J. Sobrino, and M. Mancini. "Evapotranspiration estimates at high spatial and temporal resolutions

from an energy–water balance model and satellite data in the capitanata irrigation consortium". In: *Remote Sensing* 12.24 (2020), pp. 1–24. DOI: 10.3390/rs12244083.

[**4.4**] J. Yuan, K. Emura, and C. Farnham. "Is urban albedo or urban green covering more effective for urban microclimate improvement ?: A simulation for Osaka". In: *Sustainable Cities and Society* 32 (2017), pp. 78–86. DOI: 10.1016/j.scs.2017.03.021.

[**4.5**] T. Aili, A. Soncini, A. Bianchi, G. Diolaiuti, C. D'Agata, and D. Bocchiola. "Assessing water resources under climate change in high-altitude catchments: a methodology and an application in the Italian Alps". In: *Theoretical and Applied Climatology* 135.1-2 (2019), pp. 135–156. DOI: 10.1007/s00704-017-2366-4.

[**4.6**] Flavia Fuso, Francesca Casale, Federico Giudici, and Daniele Bocchiola. "Future hydrology of the cryospheric driven lake como catchment in Italy under climate change scenarios". In: *Climate* 9.1 (2021), pp. 1–24. DOI: 10.3390/cli9010008.

[**4.7**] Leonardo Stucchi, Daniele Bocchiola, Camilla Simoni, Stefano Romano Ambrosini, Alberto Bianchi, and Renzo Rosso. "Future hydropower production under the framework of NextGenerationEU: The case of Santa Giustina reservoir in Italian Alps". In: *Renewable Energy* 215.May (2023), p. 118980. DOI: 10.1016/j.renene.2023.118980.

[**4.8**] S. Morgese, F. Casale, E. Movedi, R. Confalonieri, and D. Bocchiola. "Modelling the effects of potential climate change on the dynamics of multi-species mountain pastures: A case study in Gran Paradiso National Park, Italy". In: *Agricultural Systems* 217.March (2024), p. 103942. DOI: 10.1016/j.agsy.2024.103942.

[**4.9**] M. Mancini and R. Rosso. "Using GIS to assess spatial variability of SCS Curve Number at the basin scale". In: *New Directions for Surface Water Modeling* (1989).

[**4.10**] C. Corbari, G. Ravazzani, and M. Mancini. "A distributed thermodynamic model for energy and mass balance computation: FEST-EWB". In: *Hydrological Processes* 25.9 (2011), pp. 1443–1452. DOI: 10.1002/hyp.7910.

[**4.11**] C. Corbari, J.A. Sobrino, M. Mancini, and V. Hidalgo. "Mass and energy flux estimates at different spatial resolutions in a heterogeneous area through a distributed energy-water balance model and remote-sensing data". In: *International Journal of Remote Sensing* 34.9-10 (2013), pp. 3208–3230. DOI: 10.1080/01431161.2012.716924.

[**4.12**] John M. Wallace and Peter V. Hobbs. "Atmospheric Thermodynamics". In: *Atmospheric Science*. Elsevier, 2006, pp. 63–111. DOI: 10.1016/B978-0-12-732951-2.50008-9.

[**4.13**] S. Kato and Y. Yamaguchi. "Estimation of storage heat flux in an urban area using ASTER data". In: *Remote Sensing of Environment* 110.1 (2007), pp. 1–17. DOI: 10.1016/j.rse.2007.02.011.

[**4.14**] B. G. Heusinkveld, A. F.G. Jacobs, A. A.M. Holtslag, and S. M. Berkowicz. "Surface energy balance closure in an arid region: Role of soil heat flux". In: *Agricultural and Forest Meteorology* 122.1-2 (2004), pp. 21–37. DOI: 10.1016/j.agrformet.2003.09.005.

[**4.15**] S. Assouline, S. W. Tyler, J. Tanny, S. Cohen, E. Bou-Zeid, M. B. Parlange, and G. G. Katul. "Evaporation from three water bodies of different sizes and climates: Measurements and scaling analysis". In: *Advances in Water Resources* 31.1 (2008), pp. 160–172. DOI: 10.1016/j.advwatres.2007.07.003.

[**4.16**] A.F.G. Jacobs, B.G. Heusinkveld, and A.A.M. Holtslag. "Long-term record and analysis of soil temperatures and soil heat fluxes in a grassland area, The Netherlands". In: *Agricultural and Forest Meteorology* 151.7 (2011), pp. 774–780. DOI: 10.1016/j.agrformet.2011.01.002.

[**4.17**] Wilfried Brutsaert. "On a derivable formula for long-wave radiation from clear skies". In: *Water Resources Research* 11.5 (1975), pp. 742–744. DOI: 10.1029/WR011i005p00742.

[**4.18**] Michiaki Sugita. "Optimal measurement strategy for surface temperature to determine sensible heat flux from anisothermal vegetation". In: *Water Resources Research* 32.7 (1996), pp. 2129–2134.

[**4.19**] V. Masson. "A physically-based scheme for the urban energy budget in atmospheric models". In: *MDPI* September 1999 (2000), pp. 357–397.

[**4.20**] E. Mirabi and P.J. Davies. "A systematic review investigating linear infrastructure effects on Urban Heat Island (UHIULI) and its interaction with UHI typologies". In: *Urban Climate* 45 (2022), p. 101261. DOI: 10.1016/j.uclim.2022.101261.

[**4.21**] L. Allen, F.k Lindberg, and C. Grimmond. "Global to city scale urban anthropogenic heat flux: model and variability". In: *International Journal of Climatology* 31.13 (2011), p. 1990.

[**4.22**] M. Demuzere, B. Bechtel, A. Middel, and G. Mills. "Mapping Europe into local climate zones". In: *PLoS ONE* 14.4 (2019), pp. 1–2. DOI: 10.1371/journal.pone.0214474.

[**4.23**] A. S. Thom. "Momentum, mass and heat exchange of plant communities". In: *Vegetation and the Atmosphere* 4 (1975), pp. 57–109.

[**4.24**] C. Corbari, W. Timmermans, and A. Andreu. "Intercomparison of Surface Energy Fluxes Estimates from the FEST-EWB and TSEB Models over the Heterogeneous REFLEX 2012 Site (Barrax, Spain)". In: *Acta Geophysica* 63.6 (2015), pp. 1609–1638. DOI: 10.2478/s11600-014-0258-x.

[**4.25**] P.G. Jarvis. "The interpretation of the variations in leaf water potential and stomatal conductance found in canopies in the field". In: *Philosophical Transactions of the Royal Society of London. B, Biological Sciences* 273.927 (1976), pp. 593–610.

[**4.26**] C. Corbari and M. Mancini. "Calibration and validation of a distributed energy-water balance model using satellite data of land surface temperature and ground discharge measurements". In: *Journal of Hydrometeorology* 15.1 (2014), pp. 376–392. DOI: 10.1175/JHM-D-12-0173.1.

[**4.27**] Otto Tetens. "Über einige meteorologische Begriffe". In: *Z. geophys* 6 (1930), pp. 297–309.

[**4.28**] J. L. Monteith and M.H. Unsworth. *Principles of Environmental Physics Plants , Animals , and the Atmosphere Fourth Edition*. Elsevier, 2014. ISBN: 9780123869104.

[**4.29**] J. Oerlemans and E. J. Klok. "Energy Balance of a Glacier Surface: Analysis of Automatic Weather Station Data from the Morteratschgletscher, Switzerland". In: *Arctic, Antarctic, and Alpine Research* 34.4 (2002), pp. 477–485. DOI: 10.1080/15230430.2002.12003519.

[4.30] S. Peng, S. Piao, P. Ciais, P. Friedlingstein, C. Ottle, F. M. Bréon, H. Nan, L. Zhou, and R.B. Myneni. "Response to comment on "Surface urban heat island across 419 global big cities"". In: *Environmental Science and Technology* 46.12 (2012), pp. 6889–6890. DOI: 10.1021/es301811b.

[4.31] X Zhao and X Liu. "Primary and secondary ice production: interactions and their relative importance". In: *Atmospheric Chemistry and Physics* 22.4 (2022), pp. 2585–2600. DOI: 10.5194/acp-22-2585-2022.

[4.32] A. Cherchi, P. G. Fogli, T. Lovato, D. Peano, D. Iovino, S. Gualdi, S. Masina, E. Scoccimarro, S. Materia, A. Bellucci, and A. Navarra. "Global Mean Climate and Main Patterns of Variability in the CMCC-CM2 Coupled Model". In: *Journal of Advances in Modeling Earth Systems* 11.1 (2019), pp. 185–209. DOI: 10.1029/2018MS001369.

[4.33] J.L. García-Franco, L.J. Gray, and S. Osprey. "The American monsoon system in HadGEM3 and UKESM1". In: *Weather and Climate Dynamics* 1.2 (2020), pp. 349–371. DOI: 10.5194/wcd-1-349-2020.

[4.34] T. Kataoka, H. Tatebe, H. Koyama, T. Mochizuki, K. Ogochi, H. Naoe, Y. Imada, H. Shiogama, M. Kimoto, and M. Watanabe. "Seasonal to Decadal Predictions With MIROC6: Description and Basic Evaluation". In: *Journal of Advances in Modeling Earth Systems* 12.12 (2020), pp. 1–25. DOI: 10.1029/2019MS002035.

[4.35] B. Groppelli, D. Bocchiola, and R. Rosso. "Spatial downscaling of precipitation from GCMs for climate change projections using random cascades: A case study in Italy". In: *Water Resources Research* 47.3 (2011), pp. 1–18. DOI: 10.1029/2010WR009437.

[4.36] B. Groppelli, A. Soncini, D. Bocchiola, and R. Rosso. "Evaluation of future hydrological cycle under climate change scenarios in a mesoscale Alpine watershed of Italy". In: *Natural Hazards and Earth System Science* 11.6 (2011), pp. 1769–1785. DOI: 10.5194/nhess-11-1769-2011.

[4.37] L. Ferrarin, L. Stucchi, and D. Bocchiola. "Statistical downscaling of GCMs wind speed data for trend analysis of future scenarios: a case study in the Lombardy region". In: *Theoretical and Applied Climatology* (2024). DOI: 10.1007/s00704-024-04921-x.

[4.38] A. Soncini, D. Bocchiola, R. S. Azzoni, and G. Diolaiuti. "A methodology for monitoring and modeling of high altitude Alpine catchments". In: *Progress in Physical Geography* 41.4 (2017), pp. 393–420. DOI: 10.1177/0309133317710832.

[**4.39**] V Eyring, S Bony, G A Meehl, C Senior, B Stevens, and R J Stou. "Overview of the Coupled Model Intercomparison Project Phase 6 (CMIP6) experimental design and organisation". In: *Geoscientific Model Development Discussions* 8.12 (2015), pp. 10539–10583. DOI: 10.5194/gmdd-8-10539-2015.

[**4.40**] R.H. Moss, J.A. Edmonds, K.A. Hibbard, M.R. Manning, S.K. Rose, D.P. Van Vuuren, T.R. Carter, M. Emori S.and Kainuma, T. Kram, G.A. Meehl, J.F.B. Mitchell, N. Nakicenovic, K. Riahi, S.J. Smith, R.J. Stouffer, A.M. Thomson, J.P. Weyant, and T.J. Wilbanks. "The next generation of scenarios for climate change research and assessment". In: *Nature* 463.7282 (2010), pp. 747–756. DOI: 10.1038/nature08823.

[**4.41**] M.R. Grose, S. Narsey, F.P. Delage, A.J. Dowdy, M. Bador, G. Boschat, C. Chung, J.B. Kajtar, S. Rauniyar, and M.B. Freund. "Insights from CMIP6 for Australia's future climate". In: *Earth's Future* 8.5 (2020), e2019EF001469.

[**4.42**] V. Masson-Delmotte, P. Zhai, A. Pirani, S.L. Connors, C. Péan, S. Berger, N. Caud, Y. Chen, L. Goldfarb, and M. Gomis. "Climate change 2021: the physical science basis". In: *Contribution of working group I to the sixth assessment report of the intergovernmental panel on climate change* 2.1 (2021), p. 2391.

[**4.43**] A. Barrios-Barocio, O. Peralta, C.A. Ochoa-Moya, E. Luyando, and M. Espinosa-Fuentes. "Heat wave: a new characterization in terms of energy". In: *Frontiers in Environmental Science* 12 (2024), pp. 1–9. DOI: 10.3389/fenvs.2024.1474608.

[**4.44**] Copernicus Climate Change Service (C3S). *ESOTC 2022 – Extreme Heat*. Accessed: Oct 2025. 2023. URL: https://climate.copernicus.eu/esotc/2022/extreme-heat.

Chapter 5

Results

5.1 Milano - Baseline Scenario

5.1.1 Model tuning and calibration

For the baseline scenario of Milano, the results have already been presented in a scientific paper [**5.1**] authored by the PhD candidate.

Tuning of the $SWEB$ model uses output values of LST, compared against their counterparts, as estimated from the MODIS images. Figure 5.1 shows the city-wise mean monthly LST as obtained from MODIS, and from the model, during 2010-2022. Meanwhile, Figure 5.2 illustrates the map of the mean seasonal LST, spatially distributed across the entire domain.

As shown in Figure 5.1, the model tends to overestimate LST during the summers of 2012–2015 and 2016. These periods are characterized by higher air temperatures, reaching approximately 31.5°C, 33.5°C, and 31.5°C, respectively, which likely contributes to the observed overestimation. With respect to the increasing LST trend observed over the summer seasons, as illustrated in Figure 5.14, several years exhibit positive deviations from the overall trend. In these years, observed LST is higher than average and simulated LST even a little more. A possible explanation lies in higher-than-average air temperatures during those years, which result in LST values exceeding the expected trend. However, this discrepancy (less than 1°C) can be considered acceptable over a 13-year period, especially given that these data are averaged to construct a baseline scenario. Short-term fluctuations, particularly those associated with extreme events, are not the primary focus of this analysis. The year 2012 was notably dry, with total summer precipitation of approximately 58 mm, which is below the climatological average. The model shows a clear sensitivity to these climatic variations.

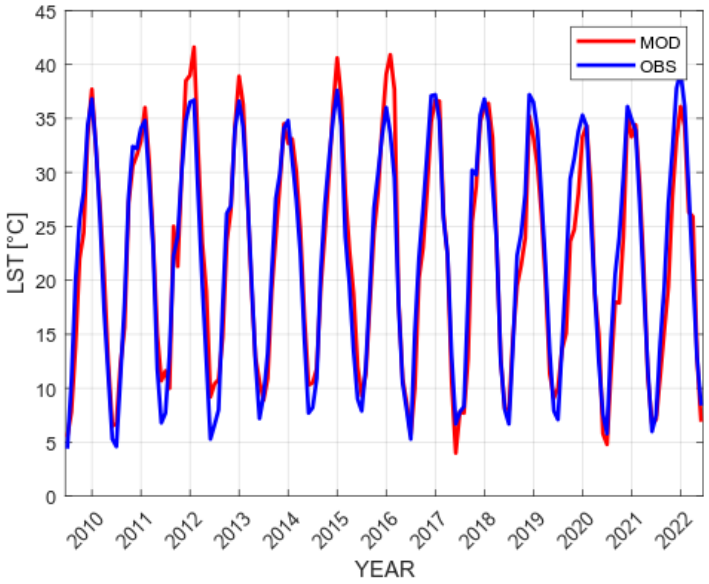

Figure 5.1. Comparison among city-wise monthly Land Surface Temperature (LST) simulated (MOD) and observed (OBS), 2010-2022

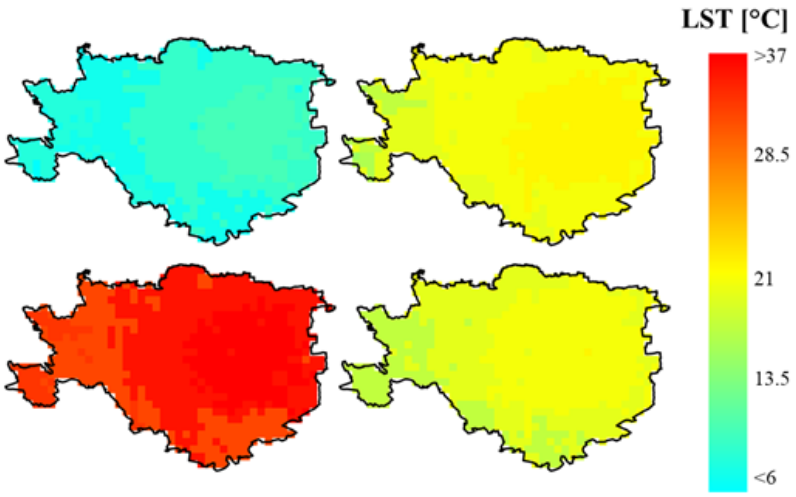

Figure 5.2. Average seasonal land surface temperature (LST) map during 2010-2022. The grid has a resolution of 500 m × 500 m, and represents the simulated LST, as output from the model, of the study area of Milano. Each map represents the average seasonal LST for every cell of the domain for: a) winter; b) spring; c) summer; d) fall.

Especially during the summer months (June, July, and August), when Surface Urban Heat Island ($SUHI$) is the largest, and heat waves are most critical, the model seems to depict the LST patterns acceptably well. Nash–Sutcliffe Efficiency index (NSE), Root Mean Square Error ($RMSE$), and average $Bias$ were used to verify as to whether the model describes accurately the information from the satellite images. The statistics city-wise are: $Bias - 0.24$°C; $RMSE =$

2.92°C and $NSE = 0.921$.

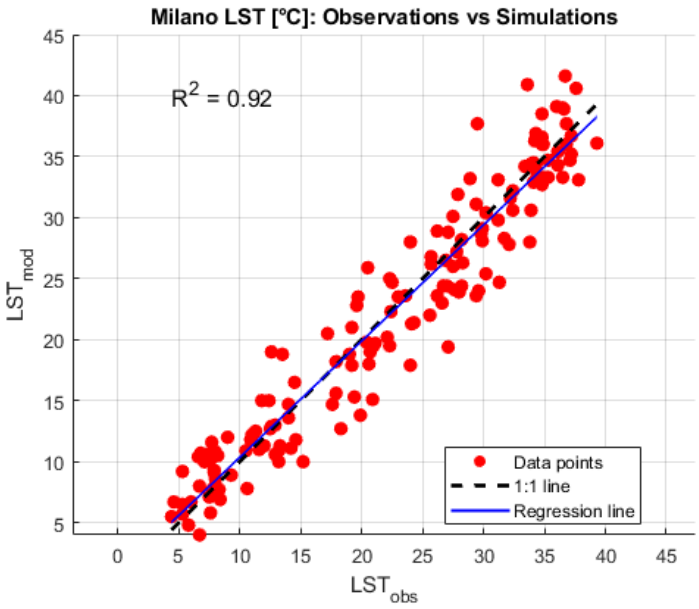

Figure 5.3. Scatter plot of time average LST: MODIS satellite observation vs $SWEB$ model simulations.

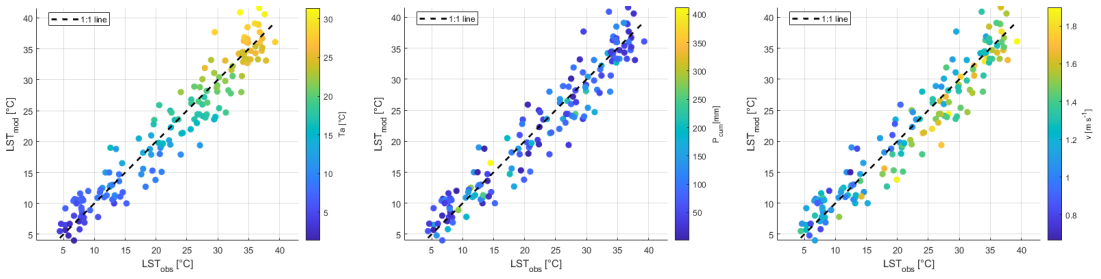

Figure 5.4. Average monthly LST satellite observation *vs* LST simulation, in function of monthly cumulated precipitation P, temperature T_a, and wind speed v.

Accuracy could be tested into gauged cells where AWS data of T_a are available, to well validate the link between air and surface temperatures, as well as the influence of presence of green areas (Figure 5.5).

An inverse correlation between LST and VF is evident. As depicted in Figure 5.5, both observed and simulated LST tend to decrease as Vegetation Fraction increases. However, the link between T_a, and VF seems less clear. Looking at the data from the gauged sites, no significant change in T_a was observed with variations in vegetation cover VF, while soil temperature LST demonstrates a stronger correlation. This investigation demonstrated the accuracy of the model not only to match mean LST values across the entire area, but even for the point-site values, as seen e.g. in the cells corresponding to FELTRE and JUVARA

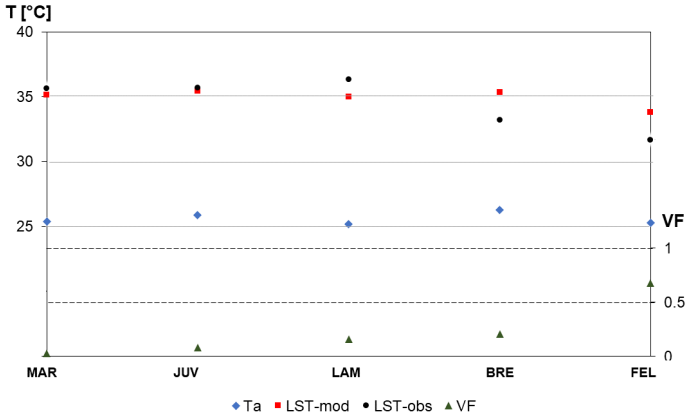

Figure 5.5. Temperature at AWS points and corresponding VF. The Figure presents observed and simulated LST during the summer season in the cells where AWSs are located. Ta is recorded by ARPA thermometers in Milano from June to August for the period 2010-2022. The data shown are the average values for these months over the observation period.

stations (Table 5.1). These two sites differ in the presence of green areas, i.e. FELTRE has a $VF = 0.67$, while JUVARA has a $VF = 0.08$. In Figure 5.6, LST during observation period for the two representative sites is plotted. In summer, average LST in FELTRE is about +32°C, while in JUVARA it is +35°C.

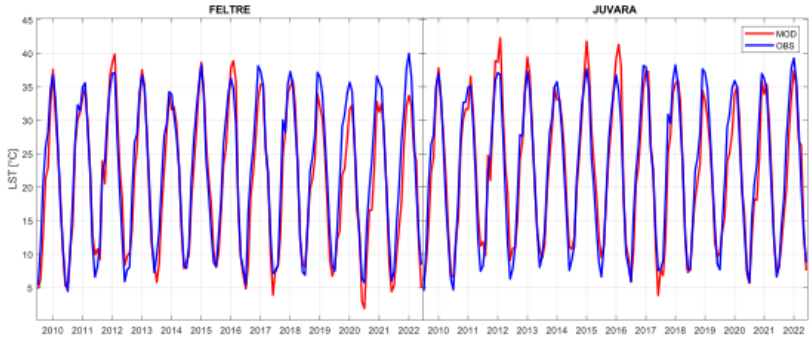

Figure 5.6. Comparison among land surface temperature LST simulated (red line) and observed (blue line) for two representative cells (and AWS stations): FELTRE (high-green site) and JUVARA (low-green site) stations, for the period 2010-2022. Data refer to the average monthly values.

5.1.2 *LST* and Surface Urban Heat Island Intensity

$SUHII$ is defined as the difference between background rural, and highest urban temperatures [**5.2**], as:

$$SUHII = LST_{VF=0} - LST_{VF=1} \tag{5.1}$$

Station	Bias[°C]	RMSE Bias[°C]	NSE [-]
FELTRE VF 67%	-1.60	3.36	0.90
JUVARA VF 8%	-0.35	3.64	0.92

Table 5.1. Goodness of fit indices (Nash-Sutcliffe Efficiency index, Root Mean Square Error and average Bias) of the variable LST for two representative cells: FELTRE (high-green site) and JUVARA (low-green site) stations. Indices have been assessed analyzing all the observation period.

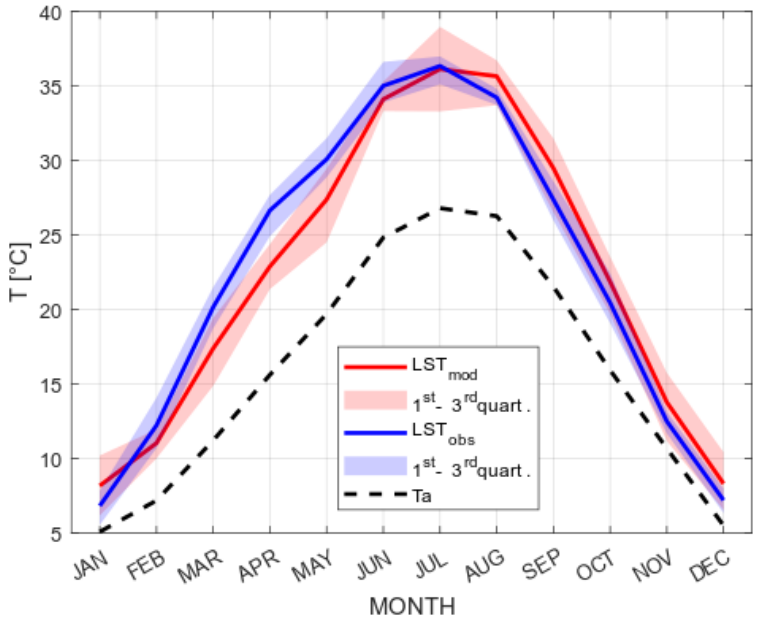

Figure 5.7. City wide average monthly values, period 2010-2022. Air temperature (Ta), MODIS observed Land Surface Temperature (LST_{obs}), SWE balance model simulated Land Surface Temperature (LST_{mod}) and respective interquartile ranges.

During summer, the average difference between green and paved areas of LST is about +3.7°C, and in some years (i.e. 2015, 2016, 2020, 2021 and 2022) it may reach $SUHII = +4.5$°C. In comparison to the average LST, green areas (VF tends to 1) have an average LST that is lower by $\Delta LST = -1.99$°C, while paved areas (VF tends to 0), exhibit an average $\Delta LST = +0.5$°C. $SUHI$ mitigation efforts should primarily focus on the summer season, as during winter the $SUHI$ can have a beneficial effect by reducing cold-related mortality. In mid-latitude regions such as Italy, cold-related mortality remains substantially higher than heat-related mortality, accounting for about 85% of total temperature-related deaths [**5.3**].

The resulting data plotted in Figure 5.8 indicate that an increase of +0.1 in VF corresponds to a decrease of $\Delta LST = -0.26$°C in surface temperature. The scatter between the linear trend and the simulation yields an $R^2 = 0.51$. A

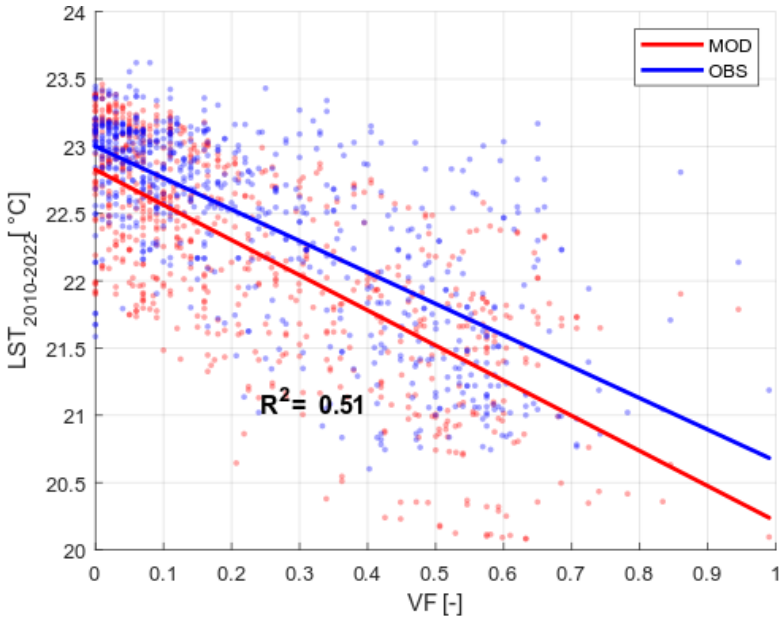

Figure 5.8. Scatter plot of LST vs VF. LST values is averaged for all the observation period. The linear trends, derived from linear regression of simulation and observation, show a decreasing pattern with a slope of -2.6%.$R^2 = 0.51$.

total of 30 outliers, out of 724 values (identified using a $|Z - score| > 2$) occur. This could be explained because some areas, even within parks, are surrounded by built-up zones, reducing their cooling effect. Still, an inverse correlation between LST and VF is appreciable. Such outliers are however equally present in both observations, and simulated values. Comparing observations and simulations (values reported in Figure 5.8), a $RMSE = 0.59$°C is obtained. From Figure 5.8, a temperature gradient based on the Vegetation Fraction can be obtained (Figure 5.9). The gradient in temperature is amplified if the soil is totally paved ($VF = 0$). In verdant regions, the gradient is more gradual, and it becomes even softer as LAI increases. According to the ARPA Lombardia sensor registry, the average height of weather stations equipped with thermometers is approximately 2.8 meters above ground level.

The highest LST values were identified in densely urbanized areas (where VF approaches 0). Conversely, the lowest LST values were found in areas with high green content (where VF approaches 1). The average seasonal difference between the warmer (paved) and the cooler (green) areas, within the concept of $SUHII$, of Milano is reported in Table 5.2.

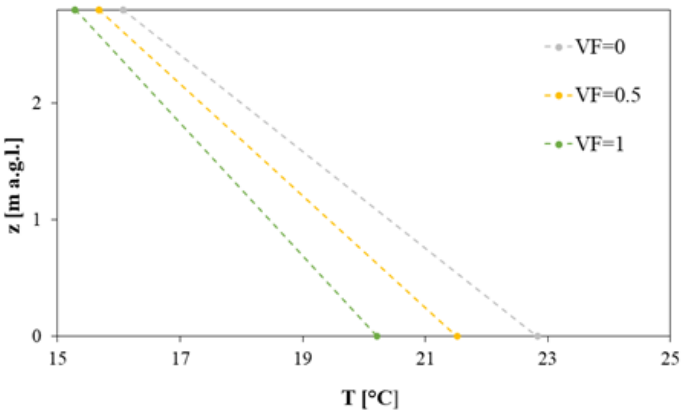

Figure 5.9. Altitudinal gradient of temperature, analysing the average land surface temperature $LST = T(z = 0)$ and the air temperature T_a = *T(z=thermometer station height)* for tree different green cover scenarios ($VF = 0$; $VF = 0.5$; $VF = 1$).

Season	$LST_{VF=1}$[°C]	$LST_{VF=0}$[°C]	$SUHII$[°C]
Spring	+20.65	+23.74	+3.09
Summer	+32.36	+36.02	+3.66
Fall	+19.53	+23.00	+3.47
Winter	+6.90	+9.89	+2.99
Year	+20.05	+23.31	+3.25

Table 5.2. The seasonal and annual land surface temperature (LST) in green and urban areas and the average Surface Urban Heat Island Intensity ($SUHII$) for the period 2010-2022.

5.1.3 *LST* in summer season

For the summer months (June, July, and August), when the issue of Surface Urban Heat Island ($SUHI$) and heat waves is most critical, the model seems to interpret the observations acceptably. During this period, the difference between air temperature and surface temperature is about +9.3°C. As shown in Figure 5.7, highest LST occurs during summer months, and this effect is amplified in the most impervious areas.

In Figure 5.10, the results of $SWEB$ during summer are shown distributed in space. Average surface temperature range is included within +32.5 °C to +37.5 °C. Indeed, suburban areas experience lower surface temperatures, especially the south-west side of Milano, while the central zones are visibly warmer. As shown in Figure 5.7, the average daily LST across the entire area of Milano overlaps quite consistently with the satellite images. Additionally, examining the spatialized LST results over the domain reveals a good coherence with the observations

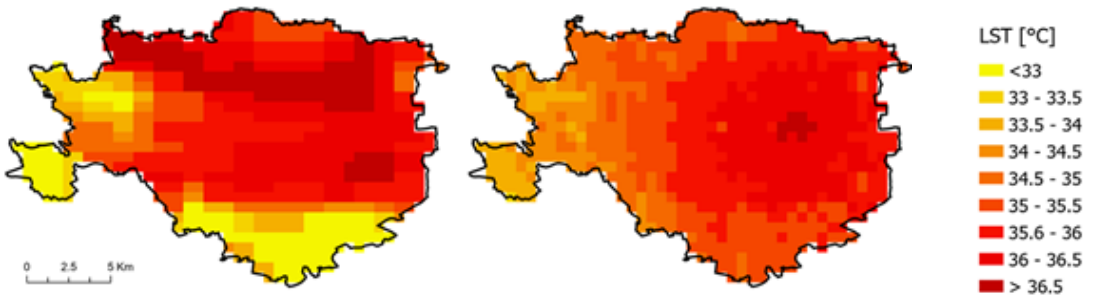

Figure 5.10. Average spatialized summer (June-August) LST value in Milano. On the left the elaboration from MODIS satellite images for the period 2010-2022; on the right simulation of $SWEB$ model.

(Figure 5.10).

The average LST in Milano during the summer period of 2010–2022 was 35.37 °C. This mean value was strongly influenced by the exceptionally hot summer of 2012, when a severe heat wave affected the Mediterranean region. That event was the second most intense air temperature episode of the last two centuries [**5.4**]. In that summer, the average LST reached 39.69 °C, exceeding the 2010–2022 reference mean by more than +4 °C. Average recorded air temperature in 2012 was 29 °C.

Each grid cell was assigned a corresponding VF value (Figure 2.3), the complementary $(1-VF)$ represents the degree of built-up or impervious surface. By comparing the mean summer LST values—computed from the satellite-derived LST maps —across $(1-VF)$ classes through a box plot analysis, a clear positive linear trend was identified. This relationship indicates that increasing impervious surface fraction corresponds to higher land surface temperatures, as reported in the boxplot in Figure 5.11. The only exception occurs in the range $(1-VF) = 0.4$–0.6. In this urban fraction class, summer LST values are lower than those in greener areas, contrasting with the general trend. However, even the applied $SWEB$ model was able to capture this irregularity, estimating lower LST values for the class $(1-VF) = 0.4$–0.6. Figure 5.12 shows the boxplot of summer LST across $(1-VF)$ classes from the simulation, which displays the same behavior as the observed data.

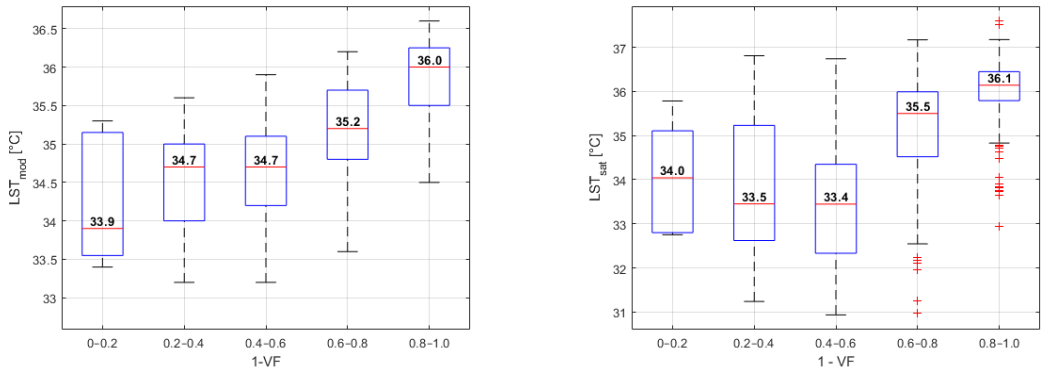

Figure 5.11. Boxplot of simulated (LST_{mod}) and satellite observed (LST_{sat}) summer land surface temperature values across five classes of built-up fraction ($1 - VF$). Each box represents the distribution of LST values within a specific $1 - VF$ interval (0–0.2, 0.2–0.4, 0.4–0.6, 0.6–0.8, 0.8–1.0). Boxes show the interquartile range, the horizontal line indicates the median, and whiskers extend to the 5^{th} and 95^{th} percentiles.

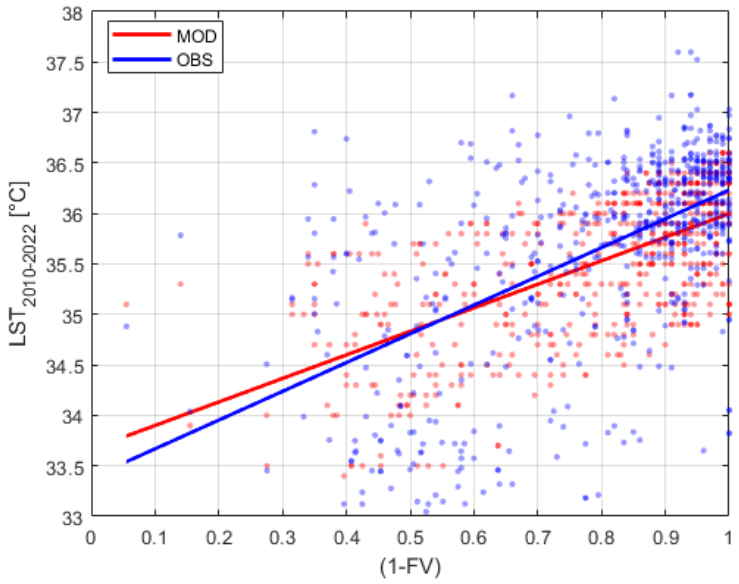

Figure 5.12. Linear trend LST vs $(1 - VF)$ for Milano summer 2010-2022 according model and Satellite images. The slope is + 2.85 °C

5.1.4 Overview on peri-urban areas of Milano: Milano West and Milano North-East

Western Milano is generally younger than the eastern side of the city. The eastern part of Milano developed earlier over time; for example, the Tangenziale Est is older than the Tangenziale Ovest, and urban expansion historically followed the main highway corridors. The western side hosts the airport (Milano Linate) and

Area	*LST* [°C]	*LST* variation [°C]
West	32.74	+1.6
North-East	35.77	+1.7
Centre	36.54	+1.9

Table 5.3. Average summer *LST* [°C] of the observation period 2010-2022 for the three area of Milano, comparing the west outskirts (*West*), the North-East outskirts (*North-East*), and the city centre (*Centre*), and the *LST* variation along the 13 (2010-2022) observations summers.

several industrial areas, while large portions of the western districts remained non-urbanized for a long time. As a result, this area became suitable for major greening and reforestation projects, such as BoscoinCittà, Monte Stella, and other public green spaces.

Southern Milano also shows a relatively high proportion of green areas; however, no ASWs are available in that sector. Overall, the western side of Milan is characterized by a higher presence of green spaces and a lower anthropogenic footprint compared to the eastern side.

Figure 5.13 shows a detailed view of three representative areas in Milano, each one with a different land cover. This zoom illustrates the impact of various land uses on *LST* during summer season. Western Milano has a dense presence of parks and forests, including Boscoincittà, Southern Agricultural Park and Quarries' Park. These green areas significantly reduce the surface temperature, as evidenced by the considerably lower *LST* values against the central areas. Here, *LAI* reaches peak values. Due to such high *LAI* values, there is an increased flux of sensible heat at the expense of latent heat, thereby reducing *LST*. The north-east side, despite being situated in a suburban area with ample green spaces such as North Park and Lambro Park, is somewhat affected by nearby industries and highly urbanized areas. The proximity to Linate Airport, and the former military airfield in Bresso seemingly contributes to higher *LST* values, when compared to the more vegetated western side. The most critical situation occurs in the center of Milano. Popular areas such as Brera, Duomo, and Porta Romana, that attract tourists and workers, experience extremely high *LST* during summer. This is exacerbated by high built-up density, low wind circulation, and increased solar radiation absorption, as due to the high thermal capacity of gray infrastructures.

Peri-urban area of Milano are less warm the the central ones, that's the effect of SUHI. As shown in Figure 5.14 and reported in Table 5.3, a light variation in *LST* is observed during the 13 year analysis. This increase is more pronounced in the central area (+1.9 °C), compared to the outskirts (+1.6 °C and +1.7 °C).

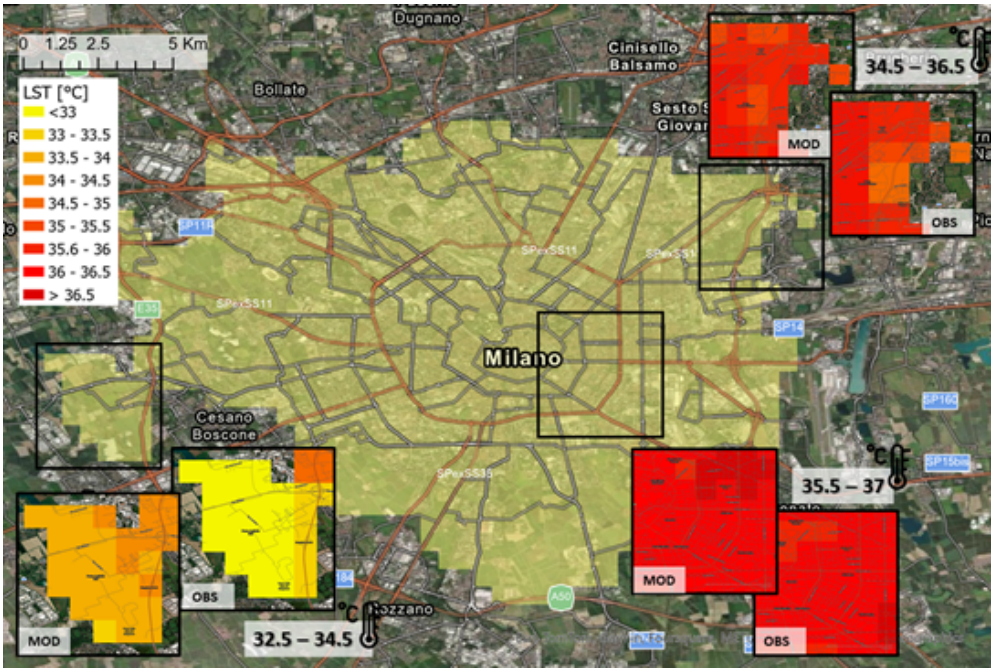

Figure 5.13. Detailed view of three representative areas in Milano characterized by distinct types of land cover. Zoomed maps compare the simulated *LST* values (**MOD**) with the observed ones (**OBS**) for summer season of years 2010-2022.

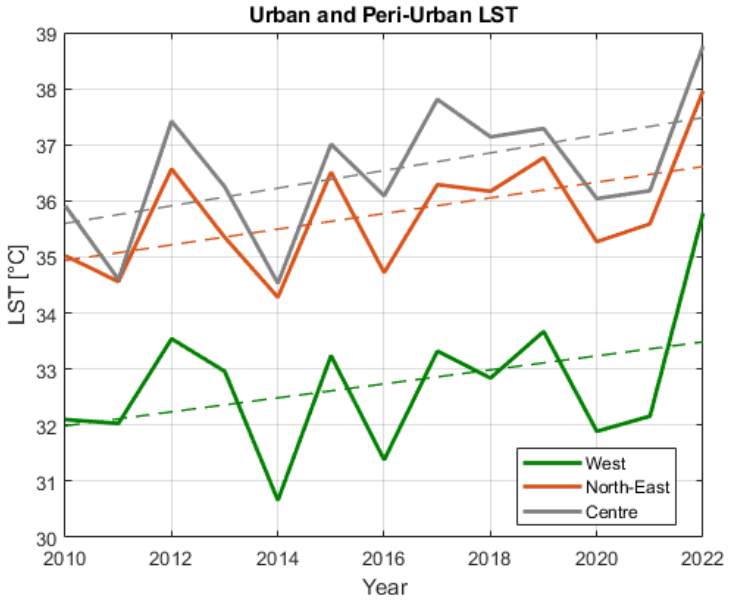

Figure 5.14. Average summer *LST* for each year of simulation, for three different areas of Milano, and trend line.

Due to this increase, even the $SUHII$ tends to get higher. This preliminary observation reveals that, due to the increase in T_a that occurred in the period 2010-2022, *LST* also increased, but this increase is higher in more urbanized areas than in peripheral areas.

5.1.5 Heat Waves events

As reported in Table 5.4, two prolonged heat wave events occurred in July 2015 and July 2022. In Figure 5.15, which displays the LST obtained from the $SWEB$ model together with satellite-derived LST observations, distinct peaks are visible during the summers of 2015 and 2022. The average LST in July 2015 reached 38 °C, while in July 2022 it reached 39 °C. These values are higher than the typical summer LST in Milan, which is around 35 °C. The summer of 2012 was extremely hot, since a severe heat wave affected the Mediterranean region. That event was the second most intense air temperature episode of the last two centuries [**5.4**]. In that summer, the average LST reached 39.69 °C, exceeding the 2010–2022 reference mean by more than +4 °C. Average recorded air temperature in 2012 was 29 °C.

Start	**End**	**n°days**
29/06/10	06/07/10	7
08/07/10	18/07/10	10
15/08/10	26/08/10	11
16/06/12	22/06/12	6
26/06/12	02/07/12	6
07/07/12	13/07/12	6
23/07/12	05/08/12	13
13/08/12	26/08/12	13
19/07/13	28/07/13	9
29/07/13	06/08/13	8
07/06/14	13/06/14	6
29/06/15	25/07/15	26
02/08/15	09/08/15	7
21/06/16	27/06/16	6
18/06/17	26/06/17	8
26/07/17	06/08/17	11
22/08/17	30/08/17	8
21/07/18	11/08/18	21
16/08/18	24/08/18	8
22/06/19	08/07/19	16
18/07/19	26/07/19	8
05/08/20	15/08/20	10
08/08/21	17/08/21	9
28/06/22	06/08/22	39

Table 5.4. Heat Waves days occurred in Milano in the period 2010-2022.

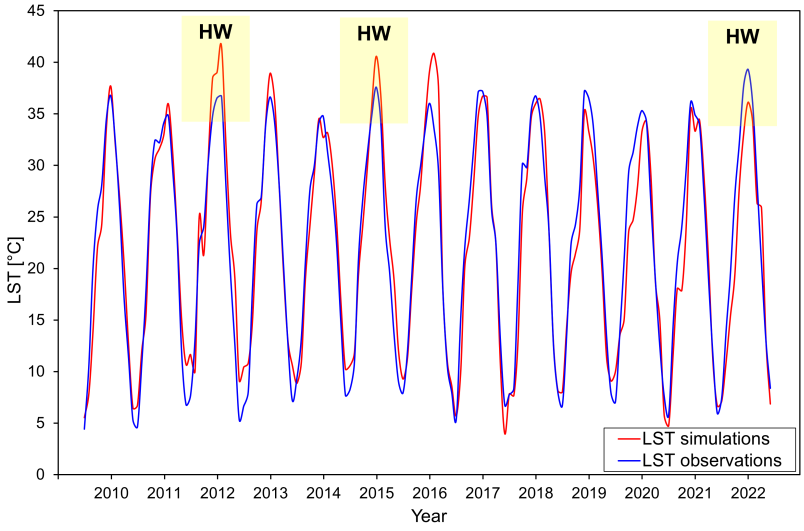

Figure 5.15. LST simulations from $SWEB$ model (red) and observation (blue) obtained from satellite images, with focus on two important HW events. The average LST in July 2015 is 38 °C, in July 2022 LST reached 39 °C.

5.1.6 Conclusion

The $SWEB$ model demonstrates a strong capability in reproducing both temporal and spatial patterns of LST over Milano during the period 2010–2022. Model performance metrics indicate high agreement with satellite observations ($NSE = 0.92$, $RMSE = 2.92$°C, $Bias = -0.24$°C), with particularly good accuracy during summer months, when SUHI effects are most pronounced.

Results confirm a clear relationship between land cover and surface temperature. Vegetation plays a key cooling role, with an average reduction of LST of about -2°C in green areas, while built-up surfaces increase LST by up to $+3.7$°C in summer. The inverse correlation between LST and VF is evident, with an increase of VF by 0.1 leading to a decrease of approximately 0.26°C. Green presence is certainly one of the most influential factors affecting LST. However, it is not the only one. Other factors, such as climatic conditions and vegetation type, also play a significant role. In particular, ungauged areas tend to show the largest discrepancies between observations and simulations. Therefore, it is essential to increase the density of climatic data networks in order to better calibrate the model and achieve more accurate simulations.

As depicted in Figure 5.10, both simulations and observations agree that south and west boundaries of Milano exhibit lower LST values. From a qualitative point of view, the model is consistent with the observed reality, and statistic metrics are good. However, some inaccuracies are still appreciable, since the observed

LST values of south and west are lower of 1-2 °C than the modeled ones. The main reason of this model overestimation is due to the fact that those area result uncovered from AWS (Figure 2.2). Here, input weather data are taken from interpolation Kriging technique, but they weren't directly validated. In addition, these areas are characterized by higher LAI values; however, satellite-derived maps often struggle to accurately capture this variability. The use of more advanced and detailed LAI datasets could improve the representation of surface resistance and, consequently, lead to a more accurate simulation of LST dynamics. This fact highlights the importance of weather monitoring, including the use of non-official data sources, to improve model performance. The results can be considered reliable, as the model shows a low bias (below 2°C at the local scale and 0.24°C overall) and reproduces spatial patterns that are consistent with observations. Although the lack of in situ measurements limits further validation, the agreement with satellite data supports the robustness of the results. Surface Urban Heat Island Intensity ($SUHII$) shows a strong seasonal variability, with maximum values in summer (up to +4.5°C) and an annual average of about +3.25°C. During summer, LST exceeds air temperature by approximately +9.3°C, highlighting the relevance of surface processes in urban thermal dynamics. Spatial analysis reveals significant intra-urban variability. Central and highly urbanized areas exhibit the highest LST values, while peri-urban and green-rich zones (particularly in western Milano) remain significantly cooler. Over the 2010–2022 period, a general increasing trend in LST is observed, more pronounced in central areas (+1.9°C) than in peripheral zones (+1.6–1.7°C), suggesting an amplification of $SUHI$ effects under ongoing warming. Overall, these results highlight the critical role of land cover composition in modulating urban thermal patterns and confirm the importance of integrating vegetation and nature-based solutions to mitigate future SUHI intensity.

Possible extensions of this model include its application to different scenarios, such as alternative urban configurations and future climate conditions. The model has already been applied to Milano under future climate scenarios, using projected climate variables as input (see Section 5.2 for the corresponding results). In addition, the model has been further refined and adapted to the city of Amsterdam, where it was implemented over a smaller domain and a shorter reference period, but with higher spatial and temporal resolution (see Section 5.3 for the corresponding results).

5.2 Milano - Future Projections

After downscaling as described, air temperature and precipitation variations were estimated for the decades:

- Short Term (ST): 2040-2050;
- Medium Term (MT): 2065-2075;
- Long Term (LT): 2090-2100.

5.2.1 Temperature Variation

Air temperature projections from four GCMs (CESM2, CMCC, HADGEM and MIROC6) were downloaded and downscaled for Milano city. As reference socio-economics pathways, SSP1 2.6 and SSP5 8.5 were considered.

SSP1-2.6 Air temperature tends to increase of about +0.88°C for ST, +1.41°C for MT and +1.54°C for LT. The increase is quite modest. The maximumun expected increase potentially occurs in august (+2.51°C).

SSP5-8.5 Air temperature tends to increase of about +1.24°C for ST, +3.14°C for MT and +4.69°C for LT. These temperature increases are particularly pronounced during the summer season, when thermal conditions are already critical, thus representing a severe and growing concern.

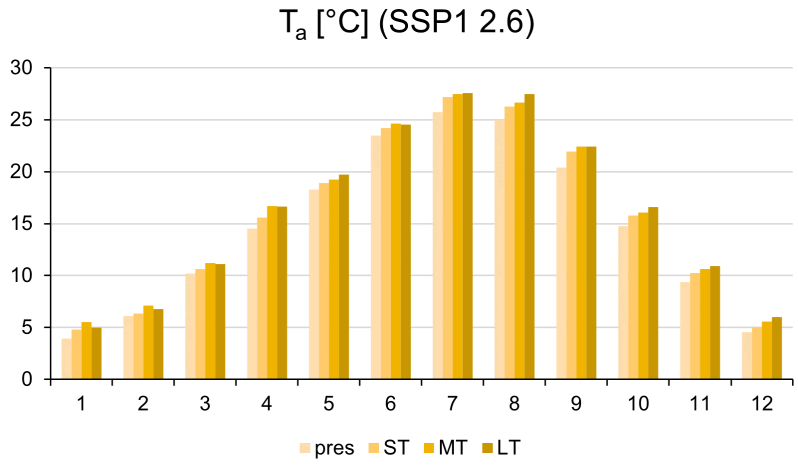

Figure 5.16. Monthly air temperature T_a variation according scenario SSP1-2.6 for reference periods: pres:2010-2022; ST:2040-2050; MT:2065-2075 and LT:2090-2100.

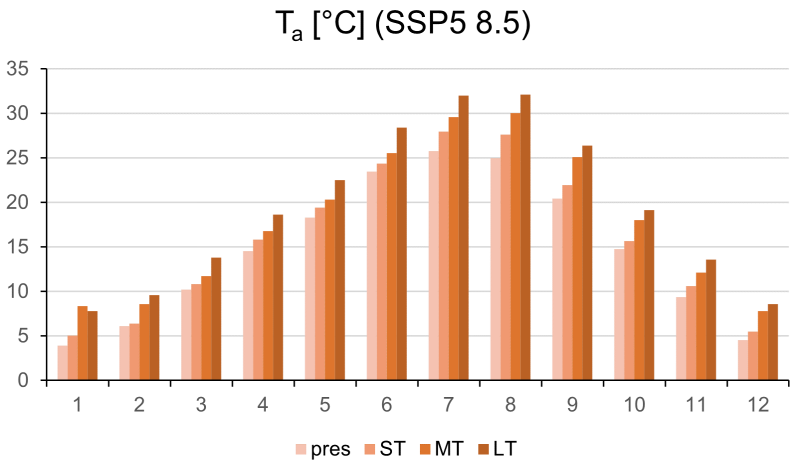

Figure 5.17. Monthly air temperature T_a variation according scenario SSP5-8.5 for reference periods: pres:2010-2022; ST:2040-2050; MT:2065-2075 and LT:2090-2100.

5.2.2 Precipitation Variation

Downscaled precipitations were estimated for the decades ST, MT and LT.

SSP1-2.6 As shown in Figure 5.18, under this scenario, the precipitation regime does not deteriorate compared to the baseline scenarios.

SSP5-8.5 Average annual cumulative precipitation tends to decrease over the decades. The estimated reduction is approximately -5% for the short term (ST), -7% for the medium term (MT), and -10% for the long term (LT).

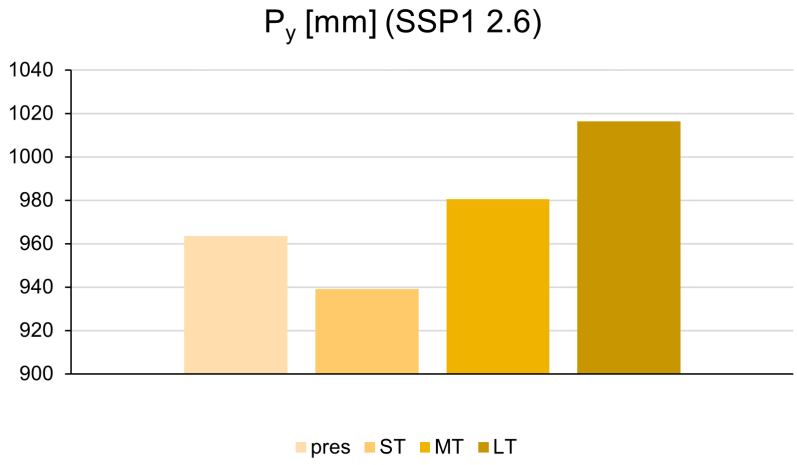

Figure 5.18. Average yearly cumulated precipitation P_y according scenario SSP1-2.6 for reference periods: pres:2010-2022; ST:2040-2050; MT:2065-2075 and LT:2090-2100.

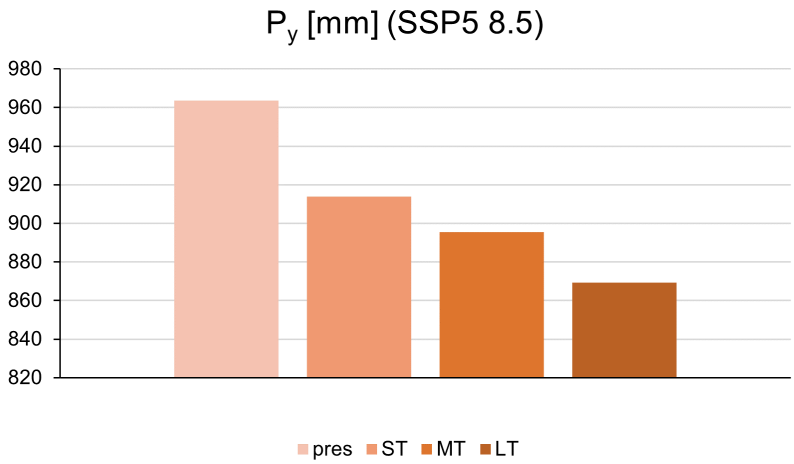

Figure 5.19. Average yearly cumulated precipitation P_y according scenario SSP5-8.5 for reference periods: pres:2010-2022; ST:2040-2050; MT:2065-2075 and LT:2090-2100.

5.2.3 Wind Speed variation

Near surface wind speed was assessed trough statistical downscale technique [**5.5**]. It was found out that wind speed, in plain areas of Lombardy region, like Milano, has the lowest values in Europe. Even the future projections don't simulate a larger increase in wind speed. Downsacaled wind speed were estimated for the decades ST, MT and LT and shown in the Figures 5.20 and 5.21.

SSP1-2.6 As shown in Figure 5.18, under this scenario, the near surface wind speed does not change a lot compared to the baseline scenarios.

SSP5-8.5 Even in the worst-case scenario, obtained by averaging all GCM outputs, the projected near-surface wind speed regime shows only minor changes compared with present conditions. The largest decrease in wind speed is estimated for LT during the summer months. This represents the most critical situation, as it combines reduced precipitation, higher air temperatures, and a light decline in air circulation. Together, these factors create harsher environmental conditions and contribute to an overall deterioration of climatic quality.

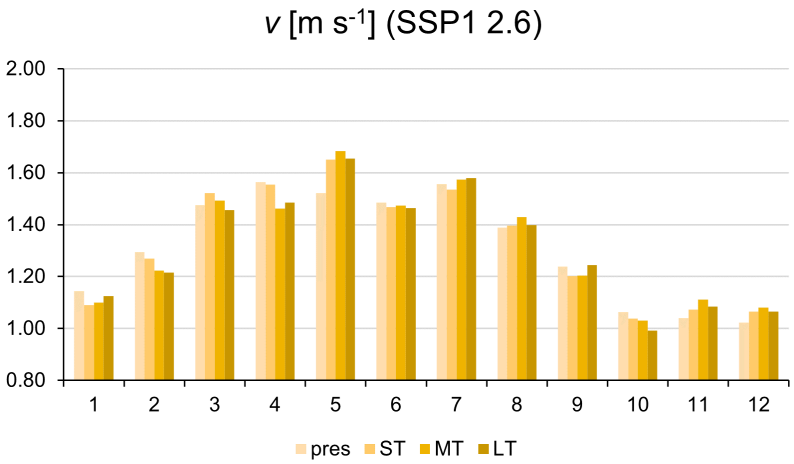

Figure 5.20. Monthly near surface wind speed v according scenario SSP1-2.6 for reference periods: pres:2010-2022; ST:2040-2050; MT:2065-2075 and LT:2090-2100.

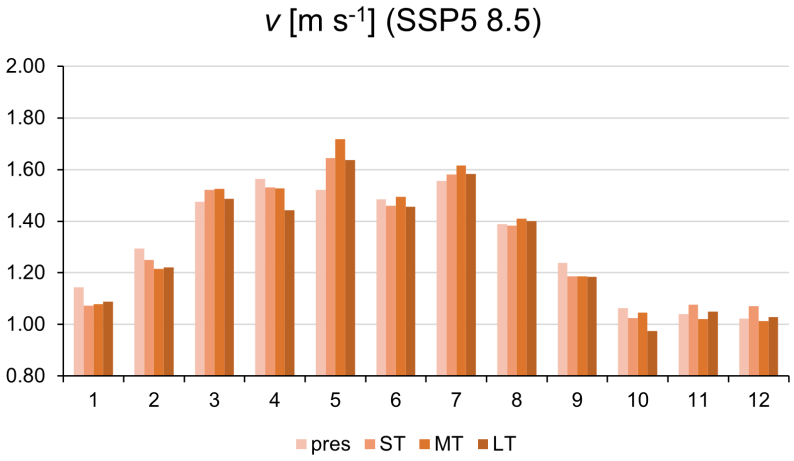

Figure 5.21. Monthly near surface wind speed v according scenario SSP5-8.5 for reference periods: pres:2010-2022; ST:2040-2050; MT:2065-2075 and LT:2090-2100.

5.2.4 *LST* under climate changes scenarios

The *SWEB* scheme was applied using future climate projections of air temperature (Section 5.2.1) and precipitation (Section 5.2.2) as input data. Solar radiation was estimated from theoretical extraterrestrial radiation [**5.6**] and subsequently adjusted using an empirical correction factor.

The two analyzed scenarios exhibit different trends in *LST*. In both cases, *LST* increases over time, although with different magnitudes.

Under the SSP1–2.6 scenario, the projected *LST* values are lower than those of the present-day scenario. In contrast, under the SSP5–8.5 scenario, *LST* shows a

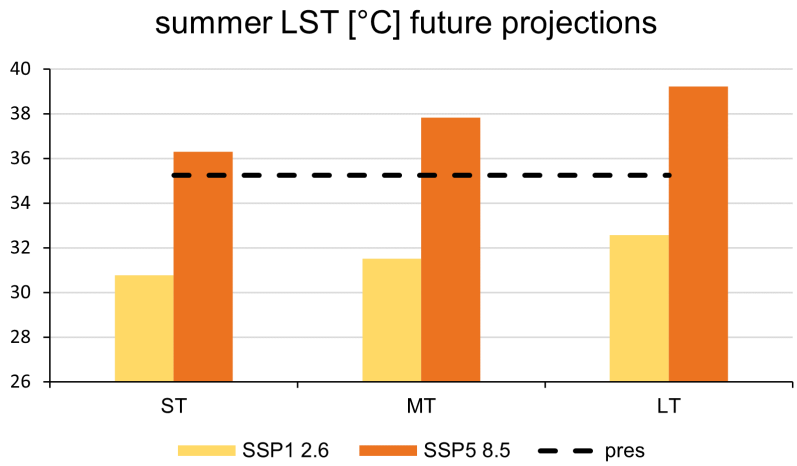

Figure 5.22. Projected mean summer LST in Milano under the SSP1–2.6 and SSP5–8.5 scenarios, compared with the present scenario.

		P [mm]	Ta [°C]	LST [°C]
present scenario		210	24.73	35.24
SSP1 2.6	ST	216	25.88	30.77
	MT	214	26.26	31.50
	LT	213	26.54	32.57
SSP5 8.5	ST	203	26.64	36.30
	MT	190	28.38	37.82
	LT	164	30.83	39.21

Figure 5.23. Projected mean summer cumulative precipitation (P) [mm], air temperature (T_a) [°C], and land surface temperature (LST) [°C]. P and T_a were derived from multiple GCMs and downscaled to Milano domain, while LST is obtained from the $SWEB$ model output.

continuous increasing trend throughout the analyzed period. This rapid increase is primarily driven by rising T_a and a concurrent reduction in P. Since no huge variation are expected for v, as shown in Figures 5.20 and 5.21, there is no sensitive linking between LST and v variations.

In summer, according to the worst-case scenario (SSP5–8.5) the simulated average $SUHII$ are very low, decreasing from approximately +0.8 °C in the short term (ST) to about +0.5 °C in the long term (LT). This indicates that the thermal contrast between green areas and urban areas is relatively weak. This behavior can likely be attributed to reduced water availability associated with a decrease in summer precipitation (Figure 5.24). Lower precipitation leads to reduced evapotranspiration, causing a larger fraction of the net radiation to be converted into sensible heat rather than latent heat. As a consequence, dry bare soil, even when classified as green, behaves thermally in a manner comparable to paved urban surfaces. Greater cooling benefits are instead associated with the presence of

tall vegetation, such as trees, which sustain transpiration, or with wet surfaces, such as water bodies, where evaporation remains available. Conversely, under the best-case scenario (SSP1–2.6), $SUHII$ remains relatively high, with ST values of +1.63 °C and LT values of +1.55 °C (Figure 5.24).

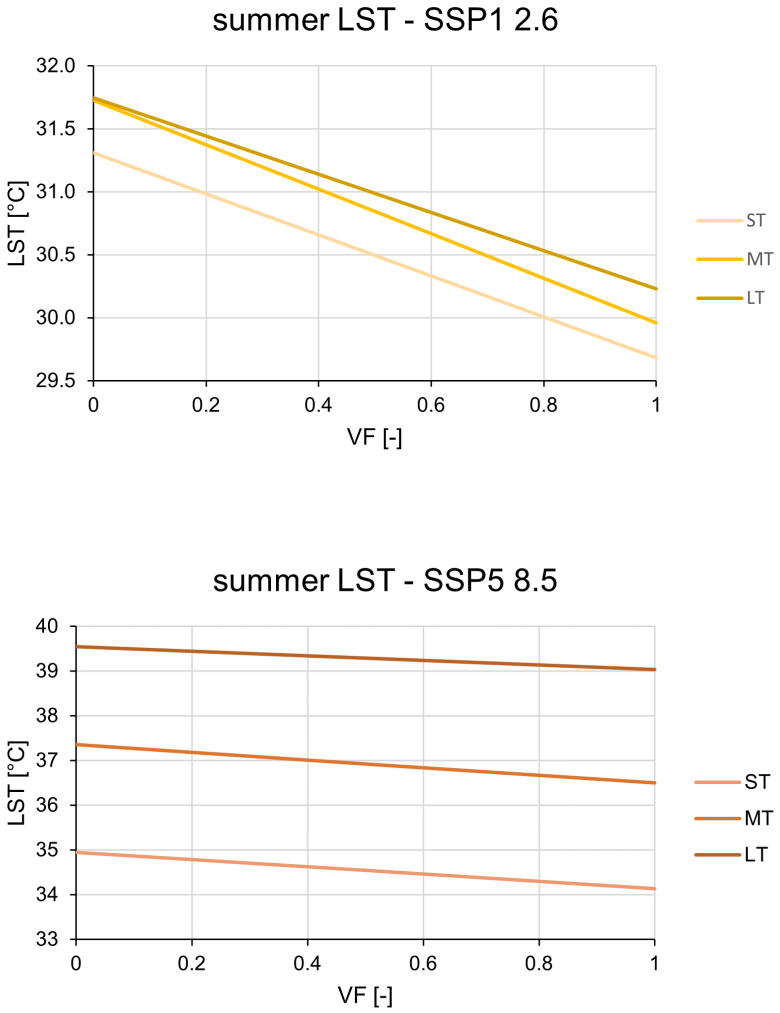

Figure 5.24. Summer LST vs VF for the three reference periods (Short Term, Middle Term, and Long Term) under the SSP1–2.6 and SSP5–8.5 scenarios. The difference $LST_{VF=0} - LST_{VF=1}$ defines the $SUHII$.

5.2.5 Conclusion

Future climate projections for Milano highlight a consistent warming trend across all scenarios and time horizons, with magnitude strongly dependent on the emission pathway. Under the low-emission scenario (SSP1–2.6), air temperature increases remain moderate (up to about +1.5°C), whereas under the high-emission scenario (SSP5–8.5) a substantial warming is projected, reaching up to +4.7°C

by the end of the century, with the most critical conditions occurring during summer.

Precipitation patterns show limited changes under SSP1–2.6, while a progressive reduction is observed under SSP5–8.5 (up to -10% in the long term), indicating increasing water scarcity. Wind speed, already low in the Po Valley, does not exhibit significant variations in future scenarios, suggesting a persistent condition of limited atmospheric ventilation.

These combined factors (higher temperatures, reduced precipitation, and weak wind regime) lead to a deterioration of climatic conditions, particularly in summer. This is reflected in the projected increase of LST, mainly driven by air temperature rise and reduced evapotranspiration.

An important result concerns the Surface Urban Heat Island Intensity: under the worst-case scenario, $SUHII$ decreases over time (from about $+0.8°C$ to $+0.5°C$), not due to improved urban conditions, but because vegetated areas lose their cooling capacity under drier conditions. Reduced soil moisture limits evapotranspiration, causing green areas to thermally behave more similarly to built surfaces.

Overall, the results emphasize that future SUHI mitigation strategies should not rely solely on increasing green coverage, but must also consider vegetation type, water availability, and the role of evapotranspiration to ensure effective cooling under changing climate conditions.

5.3 Amsterdam

5.3.1 Model tuning and calibration

The calibration procedure was performed in two complementary steps:

- **(a) Model tuning at the Flux Tower (FT).** Outcoming Longwave radiation LW_{out} measurements collected at the FT were used to derive LST values, which were subsequently compared with the corresponding model outputs. The parameters C_H and C_{LE} were adjusted during this process, with weights assigned according to the relative abundance of the different land cover types within the grid cell. This simulation was carried out on an hourly basis over the entire study period, providing a precise and time-resolved calibration. However, it was spatially limited to a single cell of the domain, namely the one containing the FT (Figure 5.25.a).

- **(b) Model tuning among the entire domain with satellite images.** To extend the calibration beyond the FT location, the model was applied to the whole study area using spatialized input data at a resolution of 100 m × 100 m. The simulation was repeated three times, each run parameterized for a specific land cover type, and the results were subsequently weighted by their relative areal coverage (Equation 4.2). The resulting LST maps were then validated against satellite-derived LST products, obtained following the framework explained in paragraph 3.3. This step provided a broader spatial perspective, since satellite data encompass the entire domain and enable the assessment of correlations between land cover and LST (Figure 5.25.b). Nevertheless, this approach is constrained by the limited temporal availability of satellite images, all of which correspond to the same overpass time.

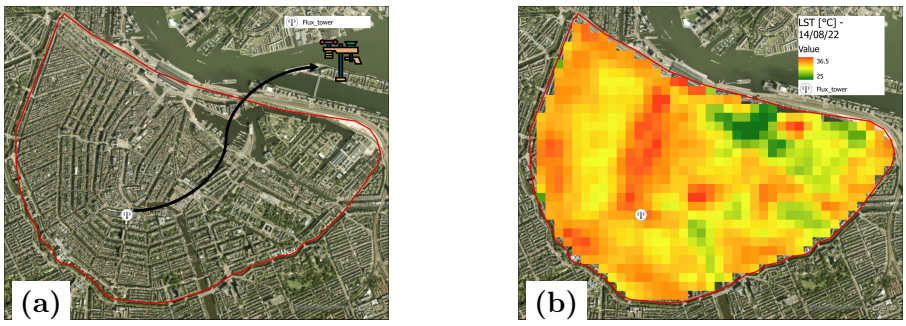

Figure 5.25. Model calibration through: (a) 1-point (FT) continuous records, (b) Landsat-8 satellite imagery (100 m × 100 m).

By integrating the "FT-based" calibration (highly accurate and temporally continuous but spatially restricted) with the satellite-based calibration (spatially comprehensive but temporally sparse), a more robust and balanced model tuning was achieved, combining the strengths of both approaches.

Model tuning at Flux Tower

Tuning of the *SWEB* model uses output values of *LST*, compared against the counterparts, as estimated from the LW_{out} records at Flux Tower. The parameters' optimization was considered satisfactory when the average bias was lower than 0.5 °C. Figure 5.26 presents the average daily *LST* over the entire observation period. The simulated and recorded *LST* trends at the FT site showed a visibly good overlap. In Table 5.5 average values of *LST* obtained from *SWEB* model at FT are reported. The 2020's summer refers only to June and July, as insufficient data were available for August. Consequently, the average *LST* values represent only the first two months of the summer period and are therefore lower than those of the other summers.

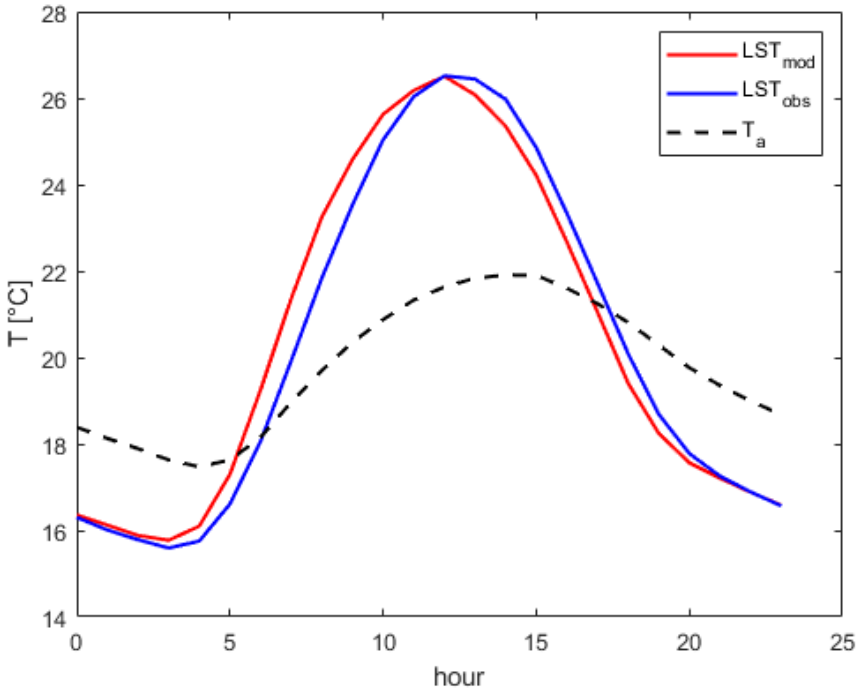

Figure 5.26. Mean hourly variation of modeled *LST* from the *SWEB* model (***MOD***) versus observed *LST* at FT (***OBS***), averaged over the summers of 2020–2024 and compared with air temperature (T_a).

	LST_{MOD}	LST_{OBS}
Summer 2020*	19.48	18.93
Summer 2021	19.59	19.66
Summer 2022	21.35	21.10
Summer 2023	20.72	20.43
Summer 2024	19.85	19.94
Average	20.20	20.01

Table 5.5. Mean *LST* values averaged over the observation period for the summers 2020–2024. Results are shown as simulated by the *SWEB* model (**MOD**) and observed at the FT station (**OBS**). *Summer 2020 includes only June and July due to limited data availability

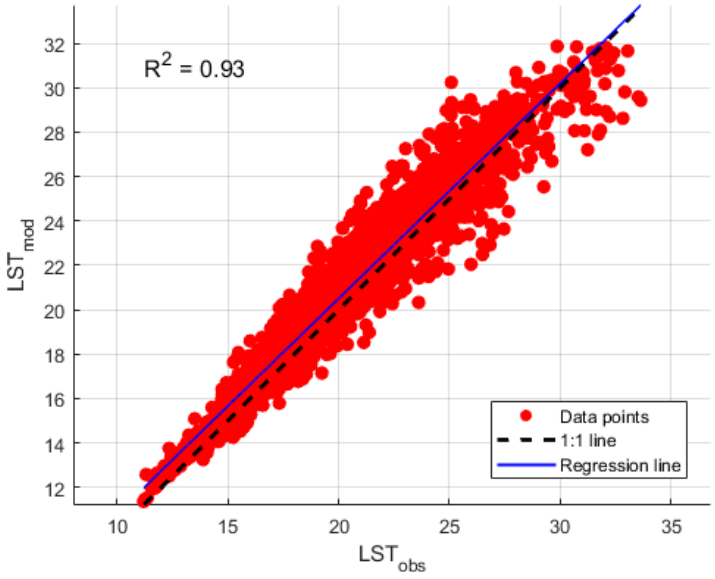

Figure 5.27. Scatter plot of *LST*: Flux Tower records ($\mathrm{LST_{obs}}$) vs *SWEB* model simulations ($\mathrm{LST_{mod}}$). Amsterdam, Summer 2020-2024.

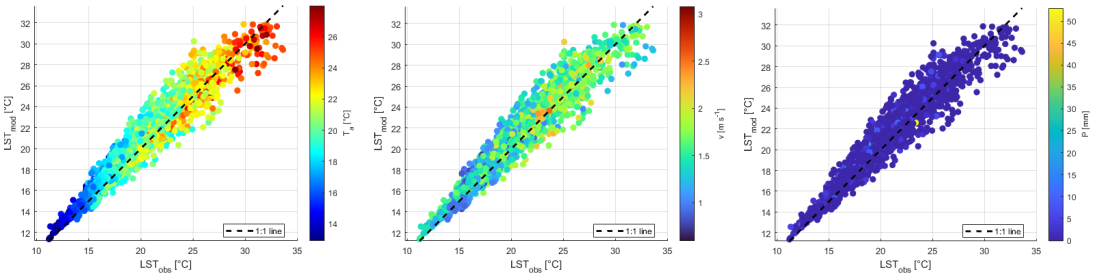

Figure 5.28. Scatter plot of LST_{obs} vs LST_{mod} at FT, with respect to air temperature, wind velocity and precipitation.

As shown in Figure 5.28, the error, defined as the difference between modelled and observed values, tends to increase at higher temperatures. The linear relationship between *LST* and air temperature (T_a) is more evident than the

relationships between LST and wind speed (v) or precipitation (P).

Summer 2022 was the warmest of the analyzed period, with correspondingly higher LST values. The mean LST exceeded 21 °C, whereas in 2020 and 2024 the average LST remained below 20 °C. Table 5.6 reports the minimum and maximum LST values recorded in Amsterdam, as well as the average daytime (08:00–19:00) and nighttime (20:00–07:00) LST. The results refer to the $SWEB$ output, which are well faithful to observation.

	LST_{min}	LST_{max}	LST_{day}	LST_{night}
Summer 2020*	7.72	38.07	22.42	16.03
Summer 2021	9.83	36.15	23.08	16.09
Summer 2022	10.52	44.69	24.77	17.95
Summer 2023	10.51	36.87	23.61	17.75
Summer 2024	9.70	35.42	22.58	17.04
Average	9.66	38.24	23.29	16.97

Table 5.6. Minimum and maximum LST values in Amsterdam, and average daytime (08:00–19:00) LST_{day} and nighttime (20:00–07:00) LST_{night}. The results refer to the $SWEB$ output. *Summer 2020 includes only June and July due to limited data availability.

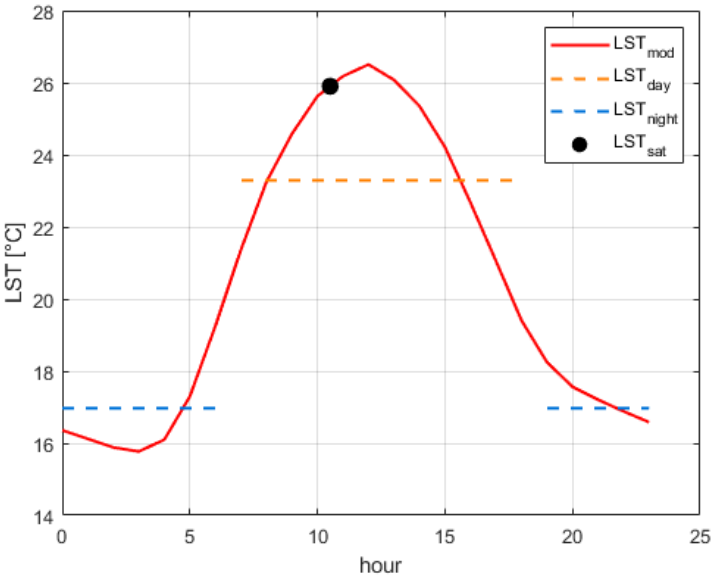

Figure 5.29. $SWEB$ modelled LST diurnal cycle, showing average daytime (08:00–19:00) LST_{day} and nighttime (20:00–07:00) LST_{night}. Landsat8 overpasses occur between 10:00 and 11:00 a.m., so all satellite-based LST data refer to this time window (black dot).

Model tuning among the entire domain with satellite images

This tuning was run to validate the model calibrated. LST maps from Landsat8 were derived using the procedure outlined in Section 3.3. Despite the regular satellite overpasses of Amsterdam around 10:00–11:00 a.m., data availability is limited by cloud cover and occasional sensor issues. For validation over the entire domain, only maps without "sink" artifacts were considered[1]. The $SWEB$ model was applied over the entire domain, producing spatially distributed values of LST. The resulting maps were compared with those derived from satellite imagery Landsat8 (Table 5.7). Satellite imagery products provide spatially well-distributed LST maps but restricted to 10:00-11:00 a.m. time window. From the analysis of LST over urban areas, green areas, and water bodies, clear differences emerge among the surface types. These differences allow the estimation of the $SUHII$, defined as the LST contrast between urban and green areas, as well as between urban areas and water bodies. Results are reported by soil type (Table 5.7) and as a function of the built-up fraction B_f (Figure 5.32), defined as the percentage of paved, urbanized surface within each 100 × 100 m grid cell of the domain. Figure 5.30 5.31 show the comparison between model output and satellite data of LST, and the associated error for each cell of the domain.

	Satellite			*Model*		
Date	LST_b	LST_g	LST_w	LST_b	LST_g	LST_w
07/06/2021	27.00	22.18	25.73	27.27	25.01	25.40
16/06/2021	30.98	28.76	28.50	32.97	29.90	28.90
13/08/2022	32.10	30.47	29.98	33.25	30.00	29.61
14/08/2022	31.63	29.75	29.31	32.47	29.98	29.73
16/06/2023	29.70	27.74	27.44	30.71	26.99	26.70
07/07/2023	30.10	28.30	28.00	29.35	26.63	26.61
10/08/2024	24.91	23.76	23.70	26.02	23.59	23.58
19/08/2024	25.10	24.53	23.85	26.41	23.67	23.32
Average	29.10	27.26	26.80	29.73	26.96	26.62

Table 5.7. Comparison between LST[°C] data obtained from *Satellite images* and *Model output* for different type of land cover: *Built-up*, *Green* and *Water*.

The observed LST maps reveal distinct spatial patterns. Lower LST values are systematically detected over water bodies, such as the Oosterdok wet dock and the Amstel canal, reflecting the cooling effect of these surfaces. In contrast, high-density built-up districts, including De Wallen and De Jordaan, exhibit significantly higher LST values, consistent with the surface urban heat island effect.

[1]Appendix - Figure 7.3

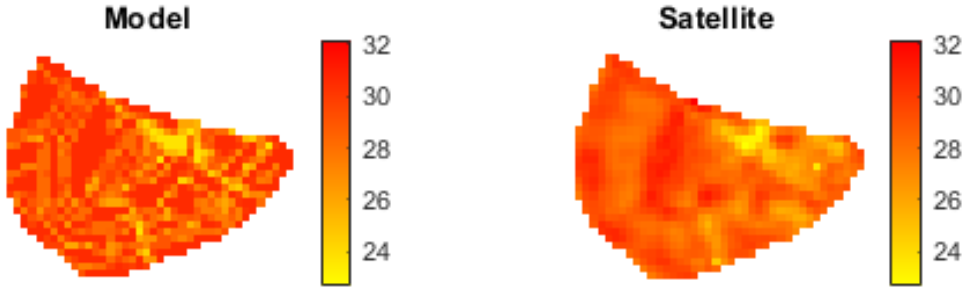

Figure 5.30. Comparison of LST[°C] maps for Amsterdam: $SWEB$ model outputs **Model** versus Landsat8 satellite observations **Satellite** averaged over the available summer dates from 2020 to 2024.

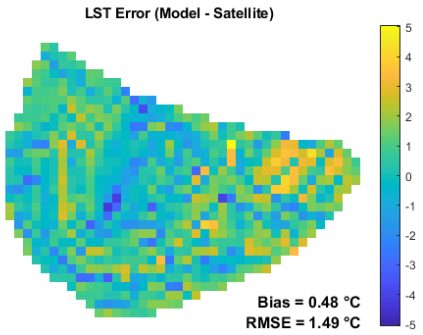

Figure 5.31. Error map showing the difference in LST between model outputs and satellite observations over the available summer periods from 2020 to 2024.

Each grid cell was assigned a corresponding B_f value (Figure 3.6), representing the degree of built-up or impervious surface. By comparing the mean summer LST values, computed from the eight satellite-derived LST maps (Figure 5.30), across B_f classes through a box plot analysis, a clear positive linear trend was identified. This relationship indicates that increasing impervious surface fraction corresponds to higher land surface temperatures, as reported in the boxplot in Figure 5.32.

There are some grid cells within the domain where the LST is appreciably lower than in others, even though both correspond to *Built-Up* areas. This can be explained by the fact that surface temperature is also influenced by the type of paved surface: for instance, the presence of white roofs, characterized by a very high albedo, results in lower LST values compared to the rest of the urban area. This represents a limitation of the model, as albedo is prescribed as a constant

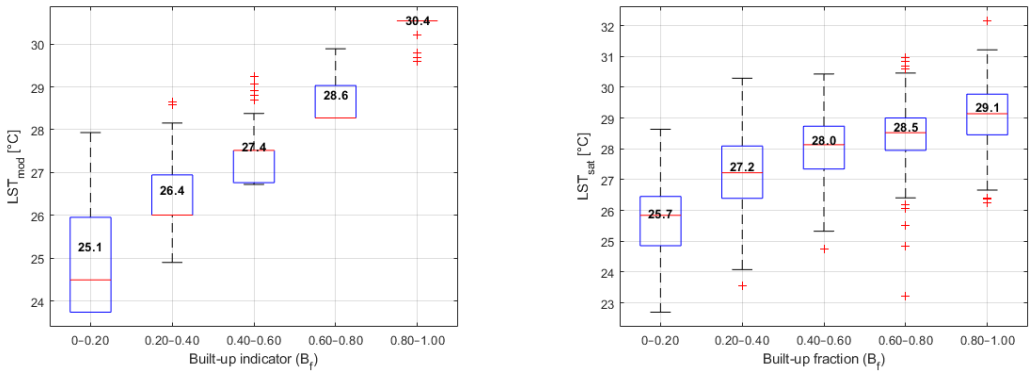

Figure 5.32. Boxplot of simulated (LST_{mod}) and satellite observed (LST_{sat}) summer land surface temperature values across five classes of built-up fraction (B_f). Each box represents the distribution of LST values within a specific B_f interval (0–0.2, 0.2–0.4, 0.4–0.6, 0.6–0.8, 0.8–1.0). Boxes show the interquartile range, the horizontal line indicates the median, the bold number is the mean, and whiskers extend to the 5^{th} and 95^{th} percentiles.

value for each soil type and is not treated as a model variable. Consequently, an average value derived from the literature and from available site-specific data was adopted (these values are reported in Table 4.2). This simplification may limit the accurate representation of point-scale LST values. However, the spatial patterns of LST are considered to be reliable, as the analysis focuses on relative variations rather than absolute values.

Double validation at FT location

In the cell containing the Flux Tower (52.3665°N, 4.8929°E), a twofold validation was possible, as both the direct outgoing longwave radiation measurements (LW_{out}) from the eddy-covariance station and the Landsat-8 satellite images, covering the Flux Tower cell at a 31 × 31 m grid resolution, were available. A comparison is carried out between: i) values retrieved from Landsat-8 imagery LST_{sat}; ii) values derived from LW_{out} at the Flux Tower LST_{FT}, and iii) $SWEB$ model output LST_{MOD}. Landsat8 satellite images are acquired between 10:00 and 11:00 a.m.; therefore, the corresponding values were compared with those obtained from the model and with those derived from outgoing longwave radiation measurements over the same time frame. The results are reported in Table 5.8. On average, FT–derived LST is higher than Landsat8-derived LST by approximately 1.3 °C, a difference that is consistent with the expected uncertainties and scale mismatch between point-based measurements and satellite observations. The comparison between modelled and Flux Tower LST shows a negligible bias (+0.18 °C) and a low RMSE (1.23 °C), indicating a good agreement

with in situ observations. The comparison between modelled and satellite-derived LST exhibits a moderate positive bias (1.45 °C) and a higher RMSE (3.53 °C); however, these differences remain within an acceptable range considering the inherent uncertainties of satellite LST retrievals and the spatial scale mismatch between point-based model outputs and satellite pixels. Overall, satellite-derived LST provides a reliable, albeit less precise, estimate of LST when compared to in situ measurements.

Date	LST_{Sat}	LST_{FT}	LST_{MOD}
13/06/20	28.44	29.52	32.24
07/06/21	28.31	28.92	27.77
16/06/21	32.78	33.01	33.367
18/07/21	30.67	28.00	-
04/07/22	25.85	25.25	-
13/08/22	33.95	34.11	34.09
14/08/22	33.24	33.39	33.43
14/06/23	31.70	29.77	28.40
21/06/23	29.49	28.87	29.86
07/07/23	31.85	32.33	30.95
08/07/23	33.00	33.81	34.84
16/08/23	26.99	27.09	29.19
18/07/24	20.25	30.92	31.69
10/08/24	26.04	28.74	27.89
11/08/24	29.13	31.17	31.29
19/08/24	25.71	27.09	26.19

Table 5.8. Land Surface Temperature at the Flux Tower location (52.3665°N, 4.8929°E), obtained using three approaches: i) derived from Landsat-8 satellite imagery (LST_{sat}), ii) estimated from outgoing longwave radiation measured at the Flux Tower (LST_{FT}), and iii) simulated using the $SWEB$ model (LST_{MOD}). All data refer to the 10:00–11:00 a.m. time frame.

5.3.2 *LST* and Surface Urban Heat Island Intensity

As introduced in Section 4.2, trough LST is it possible to assess the Surface Urban Heat Island Intensity. $SUHII$ is defined as the difference between background rural, and highest urban temperatures [**5.2**], as:

$$SUHII_g = LST_{B_f=1} - LST_{G_f=1} \tag{5.2}$$

For this case study, the concept of Surface Heat Island Intensity was extended to include the effect of water bodies, and it is therefore defined as the difference between the LST of built-up areas and that of water.

$$SUHII_w = LST_{B_f=1} - LST_{W_f=1} \tag{5.3}$$

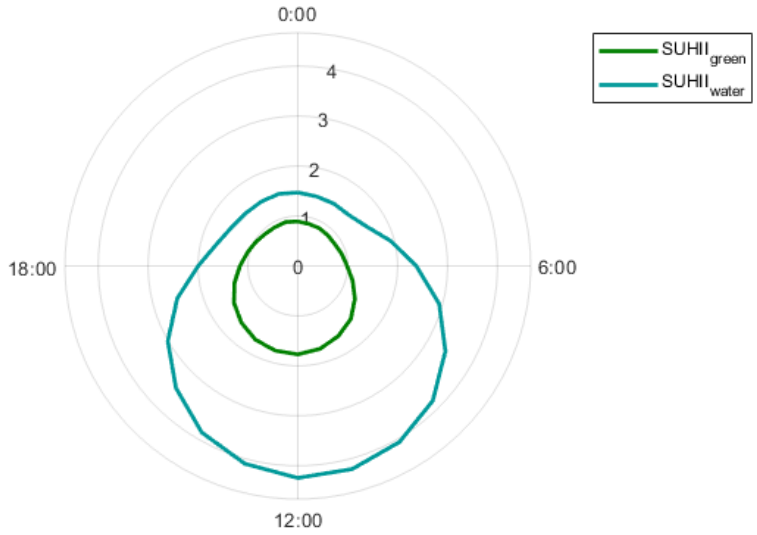

Figure 5.33. Average hourly $SUHII$ along the day for green areas ($SUHII_g$) and for water bodies ($SUHII_w$) for summer 2020-2024.

The cooling effect on LST provided by water bodies is stronger than that of green areas. The $SUHII$ values vary throughout the day, reaching their peak between 11:00 and 14:00, with values of about +4.21°C for water and +1.77°C for green areas.

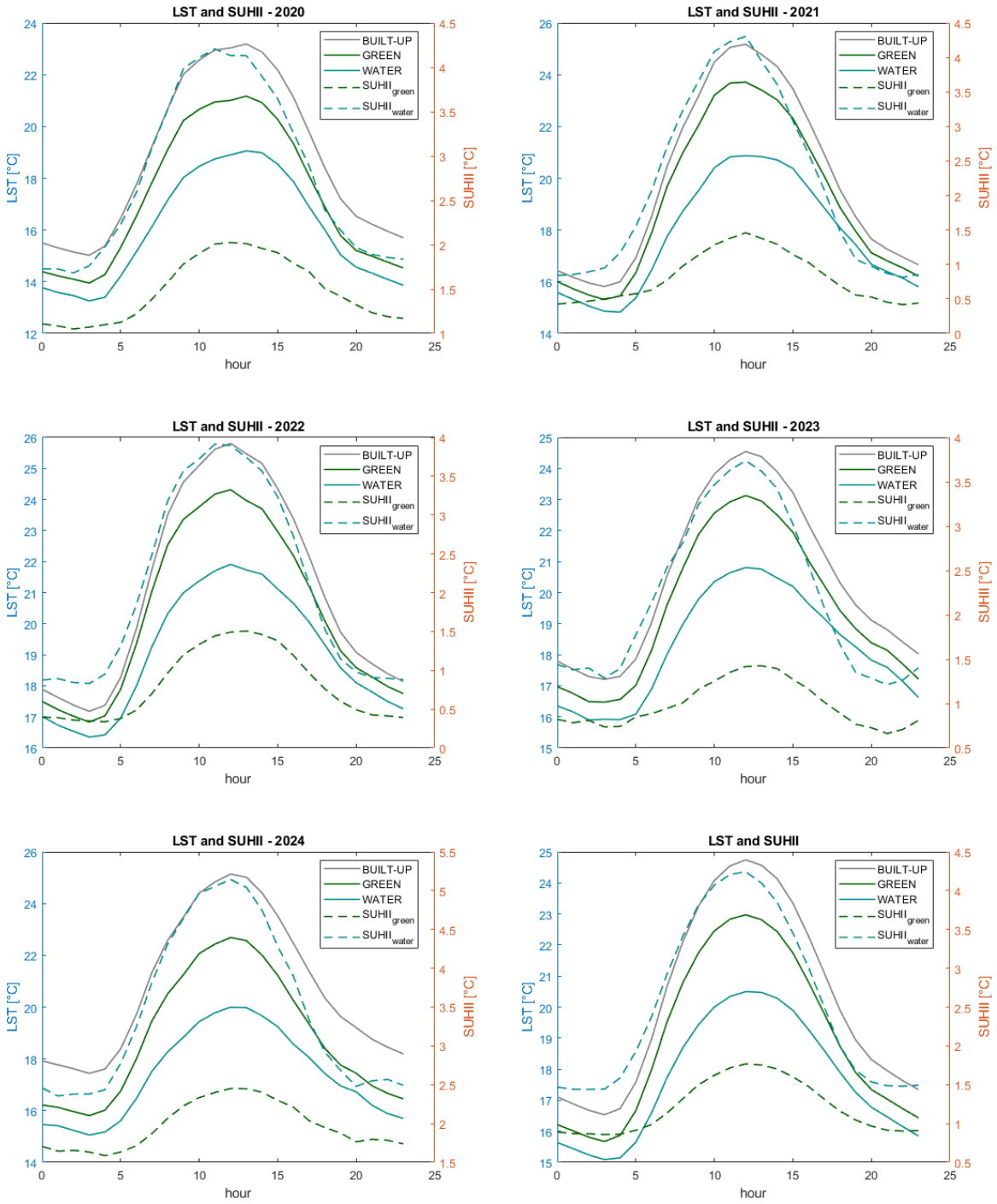

Figure 5.34. Hourly average Land Surface Temperature (LST) for different basin types ($Green$, $Built–up$, and $Water$), together with the Surface Urban Heat Island Intensity ($SUHII$) relative to green areas and water bodies, for the summers of 2020–2024 and for the overall mean.

5.3.3 Overview on a peri-urban area of Amsterdam: Schiphol

The primary study area is the city center of Amsterdam, bounded by the semi-circular Singelgracht canal. In this section, the $SWEB$ model was applied to the Schiphol area, which lies outside the main urban domain but is of particular interest for investigating the SUHI effect. Here, a KNMI AWS is settled, providing direct measurements of air temperature, wind speed, incoming solar radiation, and precipitation. These data are used as input to the $SWEB$ model. This is an airport zone, free from residential buildings and characterized by a higher presence of open and green spaces. The area mainly consists of grass-covered and paved surfaces, such as runways and airport infrastructures. Differences between Amsterdam city centre (FT) and Schiphol (KNMI 240) are evident in both meteorological conditions and surface temperature.

- Air temperature is generally lower at Schiphol, particularly during night-time hours (Figure 5.35, dotted line).

- Wind speed at 2 m is substantially higher at Schiphol, with daytime mean values around 5 m s^{-1} and peaks reaching up to 10 m s^{-1}. In contrast, such values are never reached in the Amsterdam city center due to the presence of numerous roughness elements (Figure 5.36).

- The roughness lengths are much higher in urban areas than in the open airport surroundings, increasing surface friction and reducing wind speed. These higher wind speeds are primarily attributable to the lower surface roughness at Schiphol compared to the dense urban fabric of central Amsterdam (Figure 5.36).

- As a consequence, LST is significantly lower in the Schiphol area, as shown in Figures 5.35 and 5.37.

The faster the wind speed, the lower the soil resistance to heat flux exchanges, so the resulting LST tends to be lower. In this study, the $SWEB$ model considers one soil resistance formula. It makes sense when wind speed is quite low and constant. The model indicates an LST value approximately 4 °C lower than that observed at the city center (Flux Tower). The modelled LST is consistent with satellite observations, as a temperature difference of about 4 °C between the Amsterdam city centre and the Schiphol area is also evident in Landsat8 imagery (Figure 5.37).

This pattern represents a clear manifestation of the Surface Urban Heat Island effect, with peri-urban areas exhibiting consistently lower *LST* values than the urban centre.

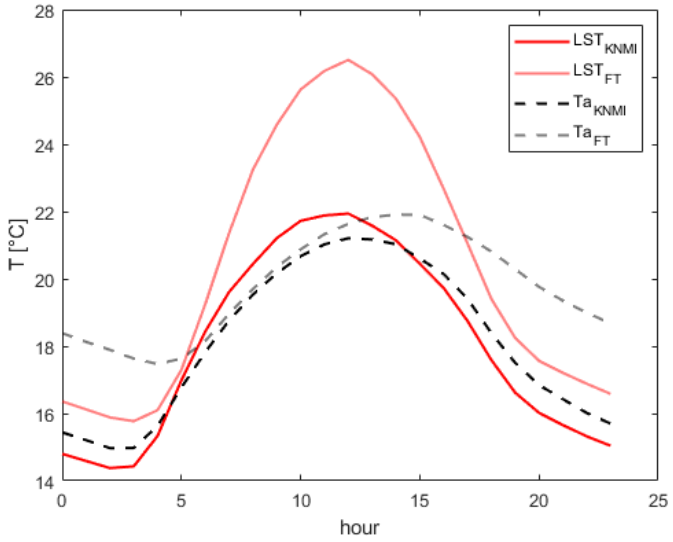

Figure 5.35. Average summer daily air and surface temperatures at the Flux Tower, located in the center of Amsterdam, and at the KNMI station no. 240 in Schiphol, situated in the peri-urban area of Amsterdam. Air temperature (T_a) values are measured, while *LST* values are obtained from the *SWEB* model.

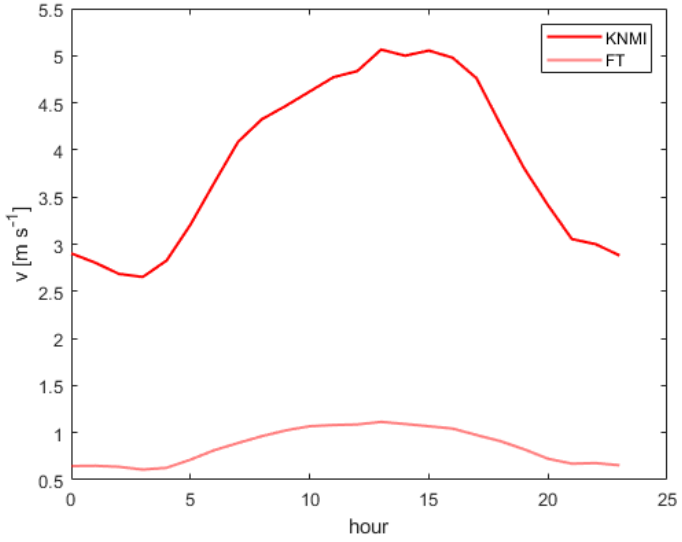

Figure 5.36. Average summer wind speed at 2 m a.g.l. recorded/evaluated at FT, located in the center of Amsterdam, and at the KNMI station no. 240 in Schiphol, situated in the peri-urban area of Amsterdam.

As depicted in Figure 5.37, the Schiphol Airport area exhibits systematically

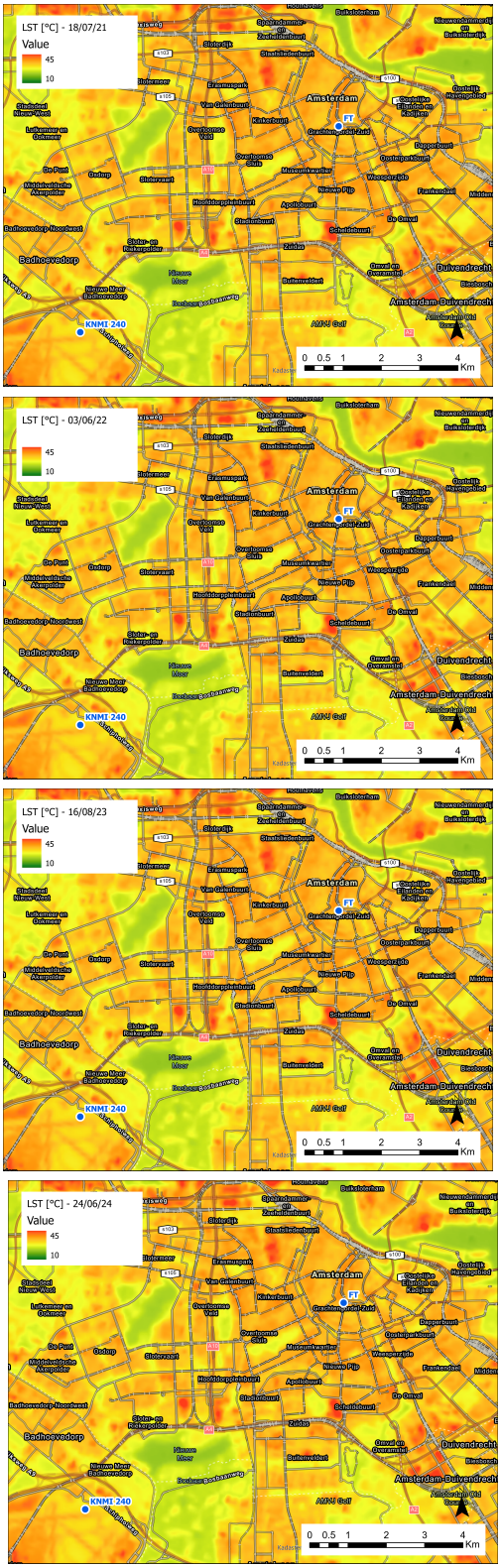

Figure 5.37. Landsat 8 map of Amsterdam at 11:00 UTC for 4 representative days. The two reference points shown are the Flux Tower (**FT**), located in the city center, and the KNMI station no. 240 at Schiphol (**KNMI 240**), situated in the peri-urban area of Amsterdam.

lower *LST* than central Amsterdam, as indicated by both model simulations at the FT and KNMI-240 locations and satellite observations. This difference is partly influenced by the location of the KNMI station, which is situated on a vegetated surface. Nevertheless, satellite-derived *LST* clearly shows higher temperatures over the paved surfaces and road infrastructure within the airport area, highlighting the role of impervious surfaces in enhancing surface heating. These results confirm that, despite lower air temperatures and higher near-surface wind speeds, *LST* remains primarily controlled by land cover characteristics. A detailed zoom of the area is shown in Figure 5.38.

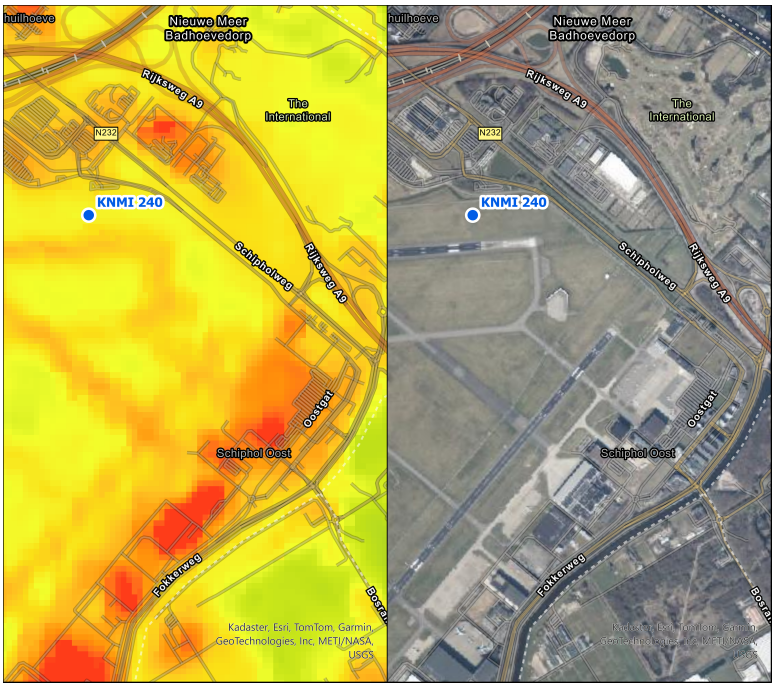

Figure 5.38. Zoomed view of the Schiphol Airport area. Left: *LST* map from Landsat8 (24/06/2024, 11:00 a.m.). Legend is the same as Figure 5.37.

5.3.4 Bowen ratio and heat fluxes partitioning

At the surface, the available solar energy is partitioned into latent heat LE and sensible heat H with rest of energy storage at ground (Equation 4.6). Energy balance equation could be written using Bowen ratio β.

$$\beta = \frac{H}{LE} \tag{5.4}$$

The metric β expresses the proportion of energy converted into sensible heat, and thus temperature increase, relative to latent heat. Blue-green spaces are typically characterized by a low Bowen ratio (β = 0.1–1), whereas urban areas exhibit higher values (β = 2–5). The Bowen ratio is often used to estimate latent or sensible heat fluxes when one of the two is missing, particularly in simplified atmospheric boundary-layer analyses **[5.7]**. Bowen ratio β is often linked to Surface Energy Partitioning Index ($SEPI$), that refers to how the available energy at the Earth's surface is divided or partitioned primarily into latent heat flux, sensible heat flux, other residual fluxes and energy storage. This partitioning controls processes such as evaporation, transpiration, and heating of the air near the surface, influencing climate and weather patterns **[5.8]**.

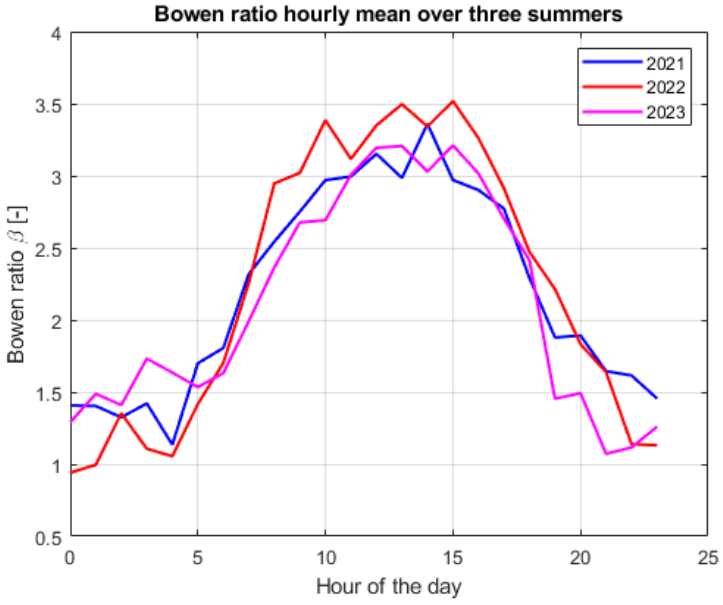

Figure 5.39. Bowen ratio β hourly mean over summers 2021 - 2022 - 2023.

Through the eddy covariance flux tower, Bowen ratio (β) measurements were available for Amsterdam. In particular, the β records for the summers of 2021, 2022, and 2023 were analysed. Figure 5.39 shows the hourly mean Bowen ratio

over these three summer periods. During nighttime, β values are generally below 1, while around midday they can reach up to 3.5.

During precipitation events, β tends to decrease, with average values lower than 1 regardless of the hour of the day. However, several outliers were recorded during rainy or highly cloudy days, as the signal is often corrupted under such conditions. For instance, in summer 2023, the mean Bowen ratio was $\beta = 0.93$, but 117 out of 208 data points (corresponding to precipitation hours) were identified as not valid. During HW events, β is higher than usual conditions [**5.9**]. As shown in Figure 5.39, summer 2022, during which an intense HW event occurred in Europe [**5.10**], experienced higher values compared to the other two seasons.

Sensible and latent heat are model outputs, and the records available from the flux tower allowed us to validate them during model tuning. Given the net radiation data, all energy fluxes are partitioned as shown in the schemes in Figure 5.40.

Starting from the energy storage equation 4.6, the equation simplifies to:

$$R_n = H + LE + \text{residual} \tag{5.5}$$

More than 60% of net radiation—defined as the difference between incoming and outgoing shortwave (SW) and longwave (LW) radiation is converted into sensible heat H, while only a small fraction contributes to latent heat LE. The terms that close the equation is not measured but determined as residual. The residual term accounts for the liquid rainfall contribution (LR, when precipitation occurs), the anthropogenic heat flux (AHF, taken from literature), and the rate of change of surface energy storage dS over time dt.

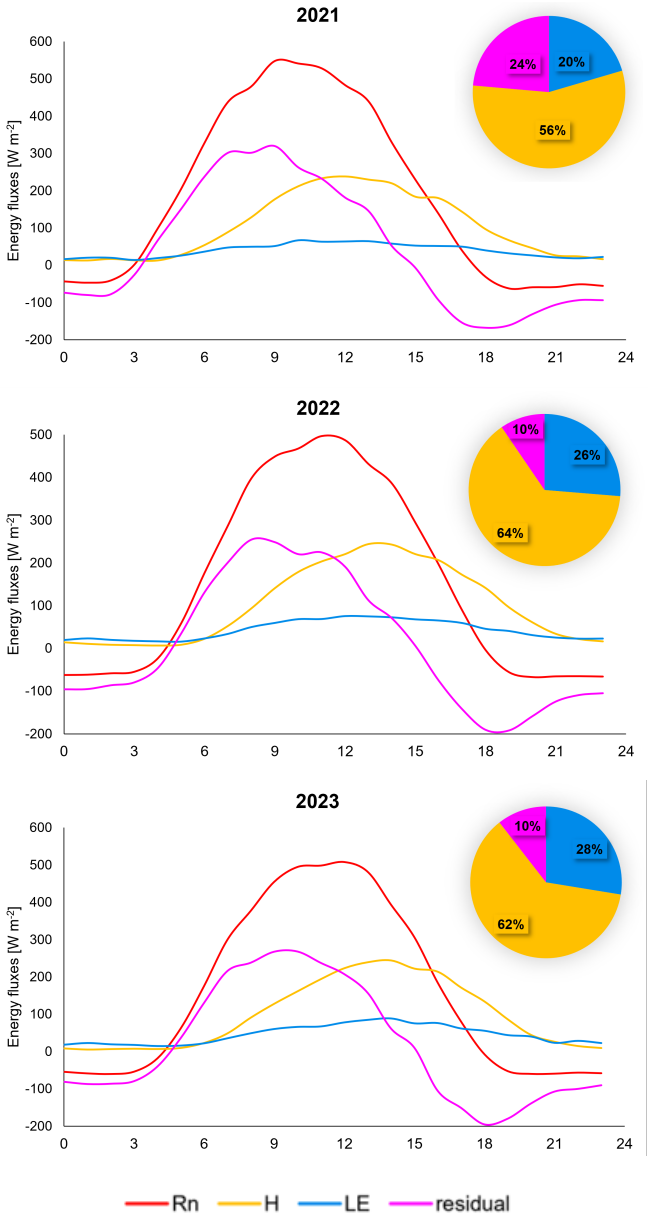

Figure 5.40. Hourly Net Radiation (R_n), Sensible Heat (H), and Latent Heat (LE) measured at the Flux Tower and averaged over the summer periods of 2021, 2022, and 2023. The "residual" represents the term required to close the Surface Energy Balance and includes the anthropogenic heat flux (AHF), the liquid rainfall term (LR, for rainy days), and the rate of change in surface energy storage ($\frac{dS}{dt}$).

5.3.5 Heat Waves events

Start	End	n°days
05/08/20	17/08/20	13
10/08/22	16/08/22	7
10/06/23	20/06/23	12
11/08/24	16/08/24	6

Table 5.9. Heat Waves days occurred in Amsterdam during period 2020-2024.

When heat waves (HW), defined as anomalously high temperatures persisting for at least six consecutive days, occurred, the LST recorded by the flux tower radiometer also showed values above the seasonal average. For example, in mid-June 2023, both daytime and nighttime LST were higher than the mean values for that summer (Figure 5.41). Similarly, in Summer 2022, a year known for frequent heat waves across northwestern Europe, LST tended to be higher in August, with some notable peaks already in July. Even though only one heat wave event occurred in the summer of 2022, this year recorded the largest difference between the actual temperature and the 30-year 90th percentile reference value (23.25 °C). This anomaly reached up to +13.57 °C (Figure 5.42).

Summer 2022, was a very hot summer, characterized by frequent heat events and temperature anomalies especially in North-West Europe (Section 4.4). As reported in Section 5.3.4, in Summer 2022, the recorded sensible heat flux was higher compared to the other year, H represented more than 64% of the available energy (i.e. net radiation), and Bowen ratio peak was about $\beta = 3.5$. Sensible heat flux release, the surface urban heat island (SUHI), and heat waves (HWs) are closely interconnected phenomena and jointly contribute to increased thermal stress.

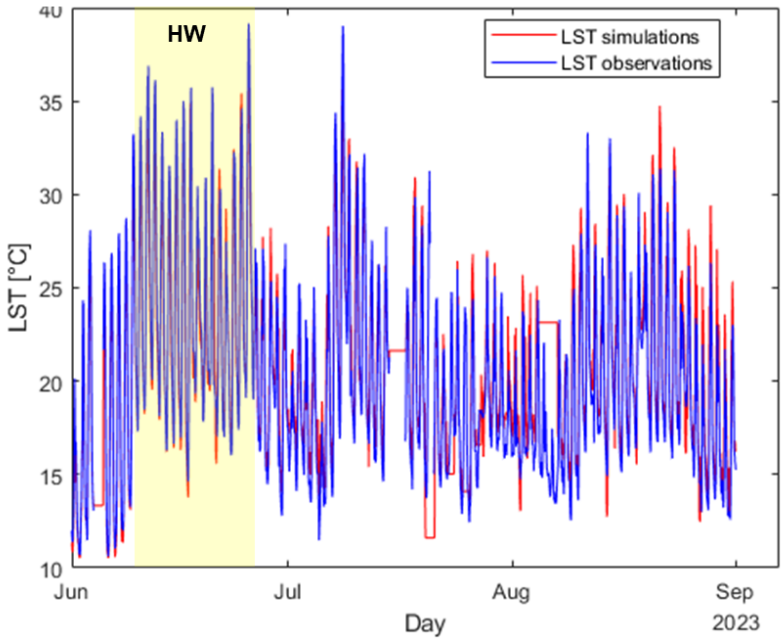

Figure 5.41. *LST* simulations from *SWEB* model (red) and observation (blue) obtained from satellite images, with focus on June *HW* event.

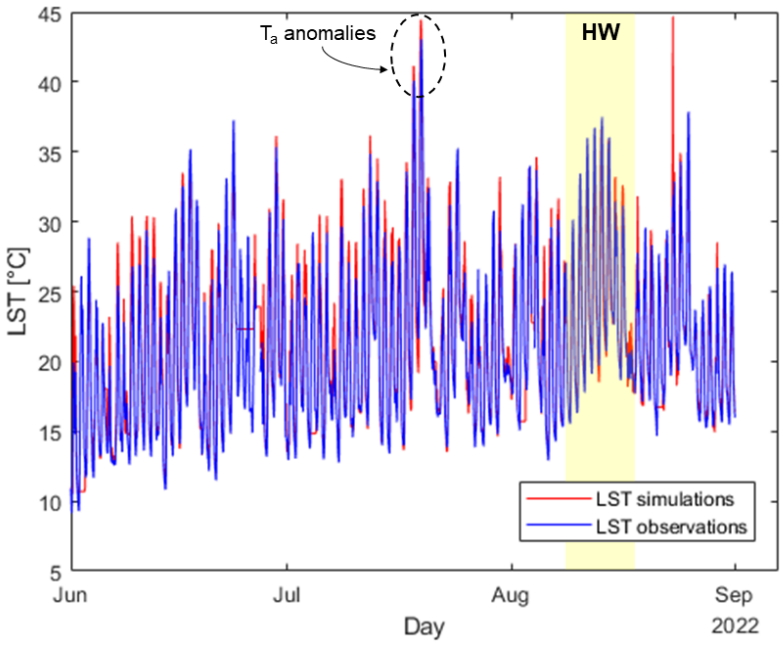

Figure 5.42. *LST* simulations from *SWEB* model (red) and observation (blue) obtained from satellite images, with focus on August *HW* events and July air temperature anomaly.

5.3.6 Conclusion

The analysis carried out for Amsterdam demonstrates the robustness and flexibility of the $SWEB$ model in reproducing both temporal and spatial variability of LST, as well as its capability to capture key urban climate processes.

The combined calibration approach, integrating Flux Tower observations and satellite data, proved particularly effective. The model shows a low bias when compared with in situ measurements (+0.18°C) and a limited RMSE (1.23°C), confirming its reliability at the local scale. A moderate discrepancy is observed with satellite-derived LST (bias $\sim$ +1.45°C; RMSE $\sim$ 3.53°C), which is nonetheless acceptable considering spatial resolution mismatches and retrieval uncertainties.

A key result is the strong dependence of LST on land cover. Average summer values show that built-up areas reach about 29.7°C, compared to 27.0°C for green areas and 26.6°C for water bodies. This confirms a clear thermal hierarchy, further supported by the positive relationship between built-up fraction and LST, highlighting urbanization as a primary driver of surface heating.

The Surface Urban Heat Island Intensity varies significantly depending on the reference surface. Peak daytime values (11:00–14:00) reach approximately $SUHII_w = +4.2$°C when comparing urban areas to water bodies, and about $SUHII_g = +1.8$°C when compared to green areas, demonstrating the much stronger cooling effect of water.

The comparison between the Amsterdam city centre and the peri-urban Schiphol area further highlights the importance of land cover and surface properties. Despite similar atmospheric forcing, LST in the city centre is on average about 4°C higher than in the peri-urban area, mainly due to higher imperviousness and reduced wind ventilation in the urban fabric.

Energy flux analysis provides additional insight into the physical mechanisms behind these patterns. The dominance of sensible heat flux (over 60% of net radiation) and relatively high Bowen ratio values confirm that urban surfaces tend to convert most of the available energy into heating rather than evapotranspiration. This imbalance becomes even more pronounced during heat waves, when sensible heat flux and Bowen ratio increase. The coupling between heat waves and urban climate is particularly evident. For instance, during the 2022 summer, characterized by extreme conditions across Europe, sensible heat flux exceeded 64% of net radiation, and Bowen ratio peaks reached $\beta \sim 3.5$. These conditions led to higher-than-average LST, with clear amplification of thermal stress during heat wave events.

Overall, these findings highlight that urban overheating is strongly controlled by land cover, energy partitioning, and extreme climate events. From a mitigation perspective, results suggest that increasing green areas alone may not be sufficient. Instead, strategies should prioritize surfaces with high evaporative potential, such as water bodies and well-irrigated or tree-covered areas, to effectively reduce LST and improve urban thermal comfort under both current and future climate conditions.

The next section (Section 5.4) focuses on the comparison between the two study cities.

5.4 Milano - Amsterdam comparison

5.4.1 Case study setup differences

Even tough the models and the aims of these two study cases are the same, some differences occur in the model settings and the final results. The more consistent difference are summarized in the Table 5.10.

	MIL	**AMS**
Space resolution	500 x 500 m^2	100 x 100 m^2
Domain area	18.1 km^2	1.98 km^2
Time resolution	1 day	1 hour
Observation period	2010-2022	2020-2024
Analyzed seasons	four seasons	summer
Soil type	Green, Urban	Green, Built-up, Water
Heat Fluxes records	no	yes

Table 5.10. Main differences between Milano **MIL** and Amsterdam **AMS** study cases.

Table 5.11 summarizes the results obtained from the $SWEB$ model application.

	MIL	**AMS**
T_a	25.99	20.63
LST	35.37	23.99
LST_b	36.02	24.55
LST_g	32.36	22.83
LST_w	-	20.34
$SUHII_g$	+3.66	+1.72
$SUHII_w$	-	+4.21

Table 5.11. Summer T_a[°C] and average results of Milano **MIL** [2010-2022] and Amsterdam **AMS** [2020-2024] study cases of summer LST[°C] summer $SUHII$[°C]

The urban and average LST values, as well as the $SUHII$, are considerably higher in Milan. This can be explained by several factors:

- **Weather conditions.** The air temperature (T_a), one of the main drivers of LST, is generally higher in Milano due to its different climatic region.
- **Precipitation.** Amsterdam experiences more frequent rainfall events, whereas Milano is characterized by occasional heavy storms but also long periods of drought.

- **Land cover.** The city centre of Amsterdam contains more green and blue spaces than Milano, and their presence contributes significantly to LST mitigation.

- **Urban morphology.** Milano is characterized by taller buildings, such as towers, skyscrapers, and high-rise housing, while Amsterdam's city centre is dominated by low-rise houses. Overall, Amsterdam is less dense and has more open urban spaces.

- **Climate.** Milano has a humid subtropical/temperate continental (Cfa, Köppen-Geiger classification) climate, while Amsterdam is characterized by a temperate oceanic climate (Cfb, Köppen-Geiger classification). Climate in Milano is continental, with more extreme events and stagnant, while in Amsterdam it is coastal, ventilated and thermally stable. In Milano, the heat storage is greater nighttime and the effect of SUHI is higher, especially during heat waves. In Amsterdam, the wind constrains the heat storage into the soil.

5.4.2 Built-up effect

For each grid cell in both study areas, Milano and Amsterdam, an indicator was assigned to represent the percentage of impervious, paved, or urbanized surface. This indicator corresponds to the Built-up Fraction (Bf) for Amsterdam and to $(1 - VF)$, the complement of the Vegetated Fraction, for Milano. In both case studies, a clear positive relationship is observed between impervious surface coverage and Land Surface Temperature: the higher B_f, the higher the mean LST. The model successfully reproduces this pattern, accurately capturing the observed increasing trend. For Amsterdam, the regression slope is +3.62°C, meaning an increase of approximately +0.36°C for every 10% increase in impervious surface.

For Milano, the regression slope is +2.33 °C, meaning an increase of approximately +0.23 °C for every 10% increase in impervious surface. The trend is clear: as surface imperviousness increases, the average LST also rises. However, the variability is higher in this case due to the complexity of the environment, with an R^2 value of 0.4.

In Amsterdam, the built-up effect on LST is partly distorted by the specific urban setting. Since water surfaces exhibit temperatures that are, on average, about 4∘C lower than surrounding land surfaces during the hottest hours of summer days, the observed LST contrasts cannot be attributed only to soil sealing

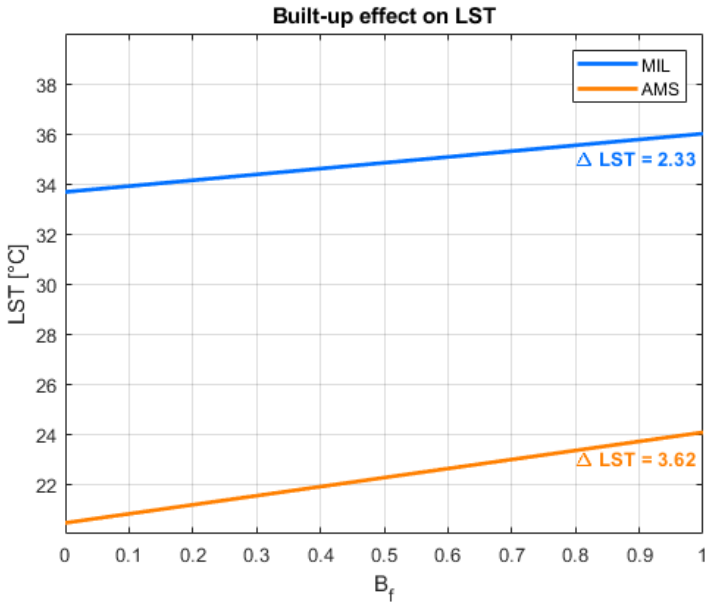

Figure 5.43. Linear trend LST vs B_f for Milano summer 2010-2022 (**MIL**) and Amsterdam summer 2020-2024 (**AMS**), according $SWEB$ model output.

or urban densification. Rather, they reflect the broader surface configuration of the area, namely the relative presence of water versus emerged land.

5.4.3 Indicators

To ensure a consistent comparison between the two study cases, Milano and Amsterdam, only the summers for which LST data were available for both cities were analyzed, namely the 2020–2022 period. Subsequently, a set of indicators was defined and evaluated over the same time span for both urban areas.

LST is a key variable for assessing urban thermal discomfort and detecting the Surface Urban Heat Island ($SUHI$) effect [**5.2**]. Nevertheless, additional stress indicators are needed to evaluate urban thermal discomfort and to provide a more comprehensive overview of climatic conditions in urban environments. In this section, the focus is on a set of indices evaluated over the same reference period (summer 2020–2022), during daytime, when results for both cities are available, in order to ensure a consistent comparison.

Climate index Precipitation values are often incorporated into vegetation-related indices [**5.11**]. In particular, I assessed the number of dry days per season and the number of days with heavy precipitation events ($P > 10$ mm). Palmer Drought Severity Index DSI [**5.12**] quantifies long-term drought conditions by assessing soil moisture anomalies relative to local climatic norms.

	MIL	AMS
2010	24.56	
2011	24.41	
2012	29.66	
2013	26.18	
2014	25.65	
2015	28.45	
2016	28.64	
2017	25.89	
2018	26.47	
2019	23.74	
2020	23.87	20.75
2021	24.03	20.04
2022	26.28	21.36
2023		20.79
2024		20.21

Table 5.12. Average summer air temperature T_a[°C] recorded in Milano (**MIL**) and Amsterdam (**AMS**).

	MIL	AMS
2010	34.46	
2011	33.51	
2012	39.69	
2013	36.47	
2014	33.45	
2015	37.81	
2016	38.05	
2017	36.02	
2018	35.69	
2019	33.06	
2020	31.85	22.33
2021	34.37	24.48
2022	34.52	25.10
2023		23.81
2024		24.20

Table 5.13. Average summer daily LST[°C] in Milano (**MIL**) and Amsterdam (**AMS**).

Wind Speed Regarding wind speed, both cities recorded similar values. Although the Netherlands are usually windier than the floodplain areas of northern Italy, the results of this study indicate that wind speeds decrease significantly within city centres due to the high concentration of buildings and other roughness elements. Consequently, when considering the central areas of Amsterdam

and Milano, their wind regimes can be regarded as unexpectedly comparable, i.e. around $1 - 2\text{ms}^{-1}$.

The wind speed data for Amsterdam refer to measurements obtained from AWS stations, rather than those recorded at the FT.

For both study areas, a wind speed sensitivity analysis was carried out. Sensible and latent heat fluxes are influenced by wind speed, and according to the energy balance model, higher values of u can lead to lower LST. However, wind speed can vary rapidly, whereas changes in LST occur more gradually. Therefore, for the hourly simulations performed with the *SWEB* model, a smoothed wind speed value averaged over approximately four hours was used.

Canopy Stress Assuming three different reference temperatures (25 °C, 30 °C, and 35 °C) as hypothetical wilting points for vegetation species, I estimated the number of days of the season during which the land surface temperature in green areas (LST_g) exceeds these thresholds, in order to define a *Canopy Stress Days Index*. It is calculated as the number of consecutive days when LST_g exceeds the assumed Wilting Point Temperature (T_{WP}).

Health risk An important index for health risk is the count of heat wave (HW) events during a season. According the WMO, an HW occurs when at least six consecutive days with maximum temperature is higher than the 90°percentile of the reference thirty-year period, in this study 1991-2020. To assess the HW frequency, the 90°percentile of the maximum temperature for 1991-2020 period was evaluated for the two European cities. SUHI amplifies the intensity and duration of HW [**5.13**]. Heat waves are driven by large-scale climatic conditions, while the urban heat island effect locally amplifies their intensity and duration, leading to higher thermal stress and increased health risks in urban areas compared to surrounding rural regions.

Index	Definition	Meaning	Category
I1	$P_{\text{day}} > 10\,\text{mm}$	Number of heavy-precipitation days	
I2	$P_{\text{day}} = 0$	Number of dry days	Climate
I3	WS_d	Daily wind speed at 2 m a.g.l.	
I4	$LST_g > 25°\text{C}$	Days with green LST above 25°C	
I5	$LST_g > 30°\text{C}$	Days with green LST above 30°C	Canopy stress
I6	$LST_g > 35°\text{C}$	Days with green LST above 35°C	
I7	HW	Number of heat-wave events	Health risk

Table 5.14. Indices list with grouped categories

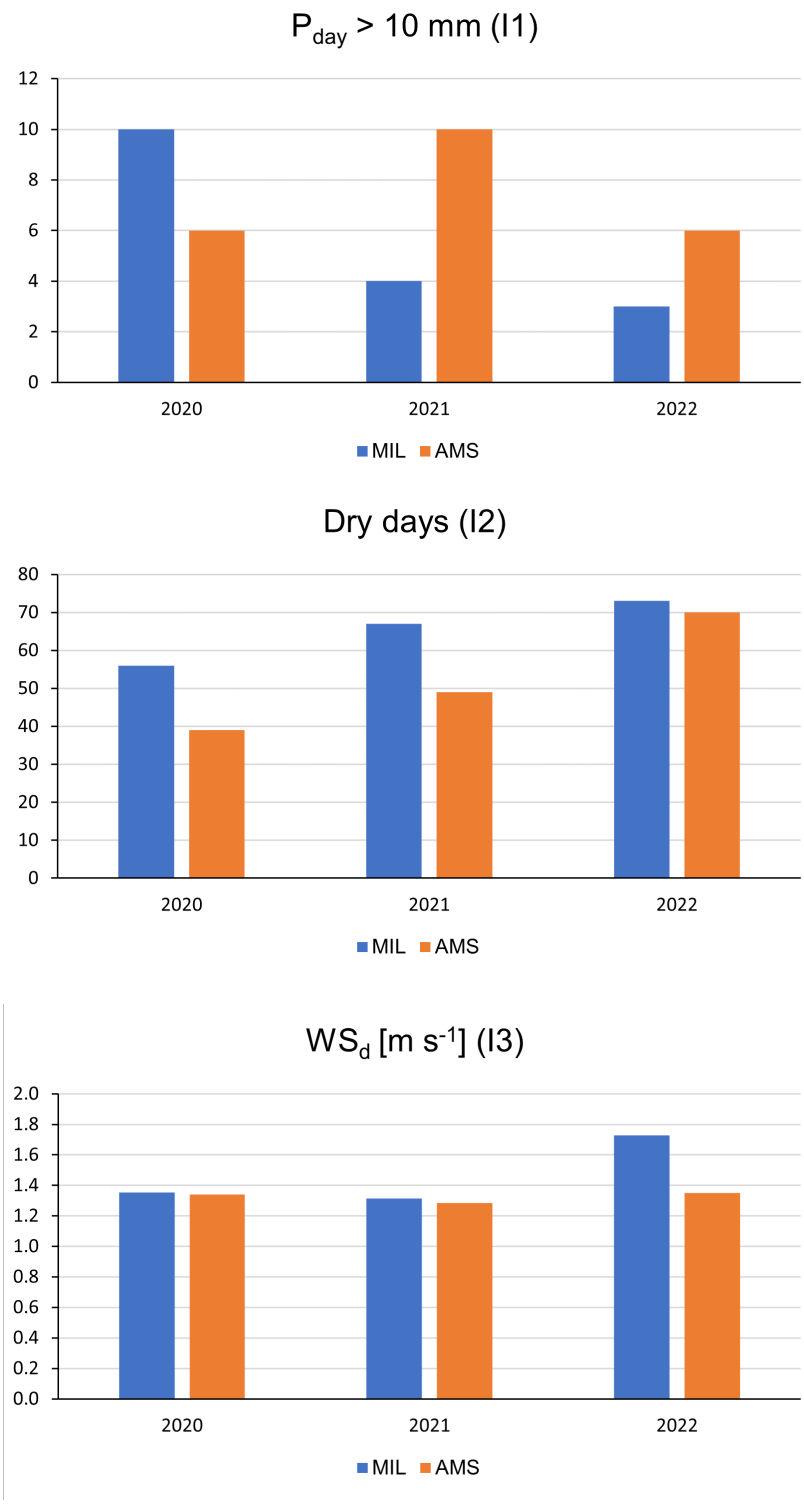

Figure 5.44. Climate indices graphs for Milano (**MIL**) and Amsterdam (**AMS**) for summer 2020-2022.

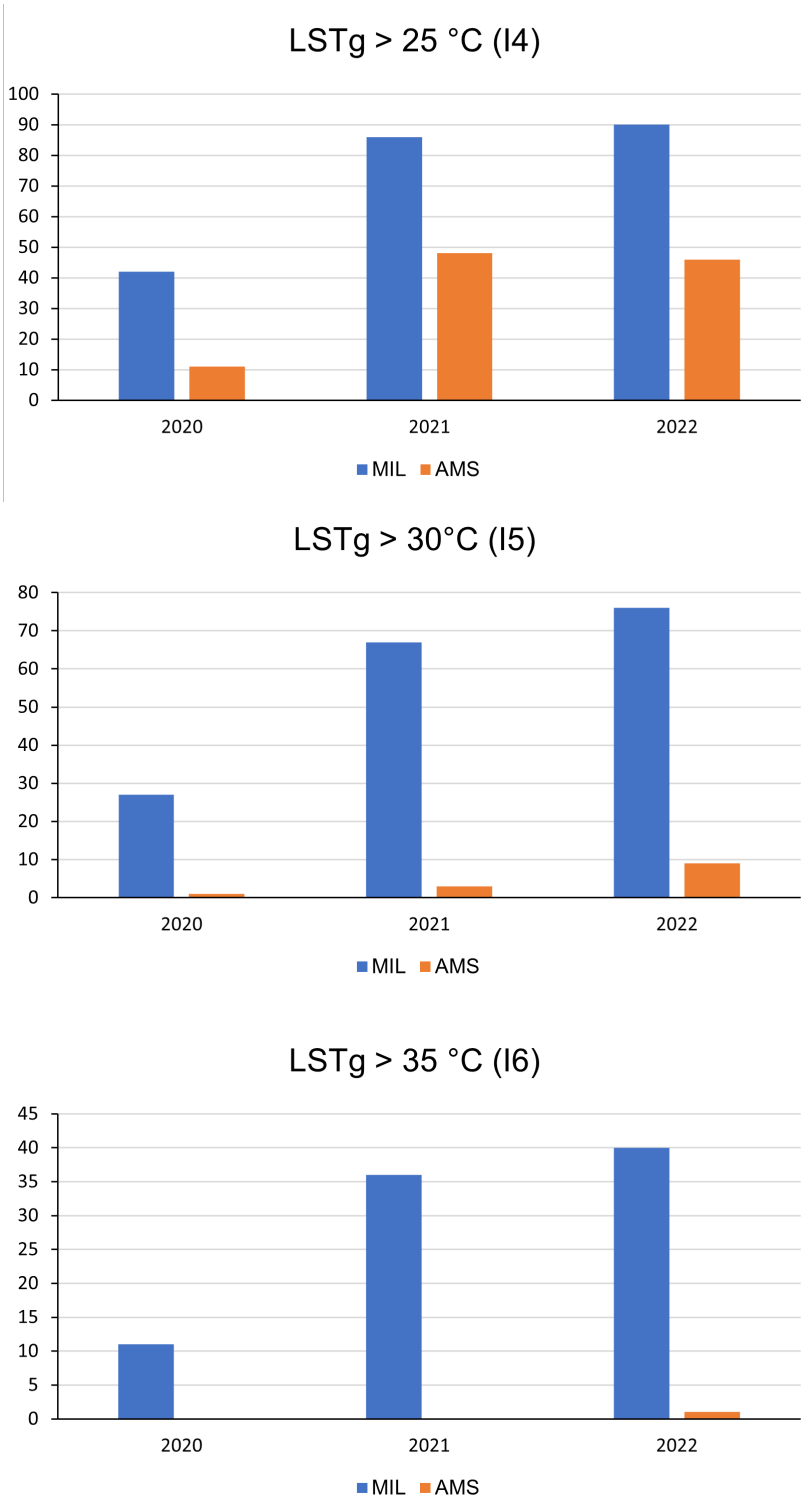

Figure 5.45. Canopy stress indices graphs for Milano (**MIL**) and Amsterdam (**AMS**) for summer 2020-2022.

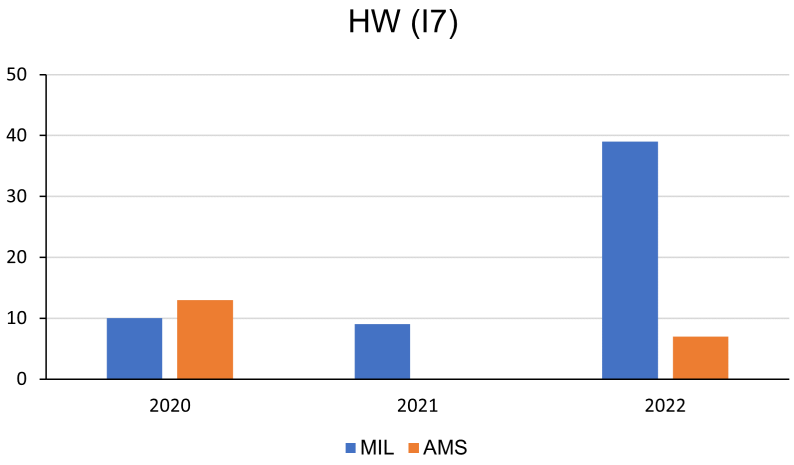

Figure 5.46. Health stress index graph for Milano (**MIL)** and Amsterdam (**AMS**) for summer 2020-2022.

Index	Summer 2020		Summer 2021		Summer 2022	
	MIL	**AMS**	**MIL**	**AMS**	**MIL**	**AMS**
I1	10	6	4	10	3	6
I2	56	39	67	49	73	70
I3	1.35	1.34	1.31	1.28	1.73	1.35
I4	42	11	86	48	90	46
I5	27	1	67	3	76	9
I6	11	0	36	0	40	1
I7	10	13	9	-	39	7

Table 5.15. Indicators for Milano (**MIL**) e Amsterdam (**AMS**) for summer 2020-2022.

5.4.4 Conclusion

A direct comparison between Milano and Amsterdam over the common reference period (summer 2020–2022) further clarifies the climatic drivers underlying the observed differences. Summer daily air temperatures in Milano are consistently higher than in Amsterdam, with even stronger contrasts observed in LST:

- Mean summer air temperature in Milano exceeds that of Amsterdam by approximately 4 °C (Table 5.12);
- Milano experiences 3–5 fewer heavy precipitation days and approximately 13 additional dry days per summer (Figure 5.44);
- Wind speeds are comparable in both cities, with mean values around 1.4 m s^{-1} (Figure 5.44);
- Over green areas, Milano exhibits higher thermal stress, with LST_g exceeding 25 °C for most of the summer and reaching 35 °C for approximately 29 days per season—conditions that are far less frequent in central Amsterdam (Figure 5.45);
- Heatwave events are both more frequent and more persistent in Milano. The extreme summer of 2022 [**5.10**] resulted in approximately 40 heatwave days in the city (Figure 5.46).

The built-up effect is clearly observed in both cities, confirming that impervious surfaces are a primary driver of surface heating. In Amsterdam, LST increases by about +0.36°C for every 10% increase in built-up fraction (slope +3.62°C), while in Milano the increase is slightly lower, about +0.23°C per 10% (slope +2.33°C), although with higher variability ($R^2 = 0.4$). This suggests that, while the physical mechanism is consistent, the Milano case is influenced by additional factors such as heterogeneous urban morphology.

The comparison over the common period 2020–2022 further emphasizes these differences. During these summers, Milano consistently exhibits higher LST values (e.g., 34.52°C in 2022) compared to Amsterdam (about 25.10°C), with a gap of nearly 10°C. This large difference translates into significantly higher thermal stress conditions.

Wind speed, surprisingly, is comparable in both city centres, with values around 1–2 ms^{-1}, despite the generally windier climate of the Netherlands. This highlights the strong role of urban roughness in reducing ventilation and suggests that, at the neighborhood scale, morphology can override regional climatic differences.

Finally, heat wave analysis highlights a strong disparity in intensity and duration. In 2022, Milano experienced an extreme event lasting 39 consecutive days, compared to only 7 days in Amsterdam. This confirms that continental climates not only reach higher temperatures but also sustain extreme conditions for longer periods. The combination of prolonged heat waves, high LST, and elevated sensible heat fluxes significantly amplifies thermal discomfort and health risks in Milano.

Overall, this comparative analysis suggests that urban overheating is not only a function of urbanization but also strongly modulated by regional climate and water availability. While both cities show similar physical relationships (e.g., LST vs imperviousness), the magnitude of impacts differs substantially.

A key implication is that mitigation strategies cannot be directly transferred between cities. In Milano, priority should be given to reducing heat extremes and enhancing evapotranspiration under water-limited conditions, whereas in Amsterdam, the presence of water bodies already provides substantial cooling, and strategies may focus more on urban design and ventilation.

More broadly, the results emphasize that effective urban climate adaptation requires a context-specific approach, integrating land cover, climate regime, and extreme event dynamics.

References

[**5.1**] S. Morgese, W. Zhang, F. Casale, and D. Bocchiola. "A Hydrological–Energy Balance Model to Assess Land Surface Temperature at the Urban Scale: The Case Study of Milano, Italy". In: *Meteorological Applications* 32.3 (2025). DOI: 10.1002/met.70069.

[**5.2**] S. Peng, S. Piao, P. Ciais, P. Friedlingstein, C. Ottle, F. M. Bréon, H. Nan, L. Zhou, and R.B. Myneni. "Response to comment on "Surface urban heat island across 419 global big cities"". In: *Environmental Science and Technology* 46.12 (2012), pp. 6889–6890. DOI: 10.1021/es301811b.

[**5.3**] A. Milojevic, B.G. Armstrong, A. Gasparrini, S.I. Bohnenstengel, B. Barratt, and P. Wilkinson. "Methods to Estimate Acclimatization to Urban Heat Island Effects on Heat- and Cold-Related Mortality". In: *Environ Health Perspect* 124.7 (2016), pp. 1016–1022. DOI: 10.1289/ehp.1510109.

[**5.4**] B. Brunetti and CNR-ISAC. *Climate Monitoring for Italy*. https://www.isac.cnr.it/climstor/climate_news.html. Istituto di Scienze dell'Atmosfera e del Clima (CNR-ISAC). Accessed: Oct 2025.

[**5.5**] L. Ferrarin, L. Stucchi, and D. Bocchiola. "Statistical downscaling of GCMs wind speed data for trend analysis of future scenarios: a case study in the Lombardy region". In: *Theoretical and Applied Climatology* (2024). DOI: 10.1007/s00704-024-04921-x.

[**5.6**] A. Soncini, D. Bocchiola, R. S. Azzoni, and G. Diolaiuti. "A methodology for monitoring and modeling of high altitude Alpine catchments". In: *Progress in Physical Geography* 41.4 (2017), pp. 393–420. DOI: 10.1177/0309133317710832.

[**5.7**] A. Porporato. "Atmospheric boundary-layer dynamics with constant Bowen ratio". In: *Boundary-Layer Meteorology* 132.2 (2009), pp. 227–240. DOI: 10.1007/s10546-009-9400-8.

[**5.8**] J. Yin, S. Calabrese, E. Daly, and A. Porporato. "The Energy Side of Budyko: Surface-Energy Partitioning From Hydrological Observations". In: *Geophysical Research Letters* 46.13 (2019), pp. 7456–7463. DOI: 10.1029/2019GL083373.

[**5.9**] A. Barrios-Barocio, O. Peralta, C.A. Ochoa-Moya, E. Luyando, and M. Espinosa-Fuentes. "Heat wave: a new characterization in terms of energy". In: *Frontiers in Environmental Science* 12 (2024), pp. 1–9. DOI: 10.3389/fenvs.2024.1474608.

[**5.10**] Copernicus Climate Change Service (C3S). *ESOTC 2022 – Extreme Heat*. Accessed: Oct 2025. 2023. URL: https://climate.copernicus.eu/esotc/2022/extreme-heat.

[**5.11**] S. Morgese, F. Casale, E. Movedi, R. Confalonieri, and D. Bocchiola. "Modelling the effects of potential climate change on the dynamics of multi-species mountain pastures: A case study in Gran Paradiso National Park, Italy". In: *Agricultural Systems* 217.March (2024), p. 103942. DOI: 10.1016/j.agsy.2024.103942.

[**5.12**] W. Zhengrong, Y. Yuting, Z. Cicheng, G. Hui, and H. Ying. "Historical and future Palmer Drought Severity Index with improved hydrological modeling". In: *Journal of Hydrology* 610 (2022), p. 127941. DOI: 10.1016/j.jhydrol.2022.127941.

[**5.13**] J. Tan, Y. Zheng, X. Tang, C. Guo, L. Li, G. Song, X. Zhen, D. Yuan, A. J. Kalkstein, F. Li, and H. Chen. "The urban heat island and its impact on heat waves and human health in Shanghai". In: *International Journal of Biometeorology* 54.1 (2010), pp. 75–84. DOI: 10.1007/s00484-009-0256-x.

Chapter 6

Discussion

This study demonstrates the applicability of a coupled surface energy and water balance framework to characterize urban thermal dynamics across two contrasting European cities, Milano and Amsterdam. The $SWEB$ model was built to recreate the LST patterns and it was calibrated using satellite-derived land surface temperature (LST) and, where available, flux tower observations, allowing for a consistent evaluation of Surface Urban Heat Island (SUHI) processes across different climatic and urban contexts. For Milano, the model was implemented at a spatial resolution of 500 m $\times$ 500 m with a daily temporal scale, whereas for Amsterdam it operated at a finer spatial resolution of 100 m $\times$ 100 m and an hourly temporal scale. The analysis for Milan covered a 13-year observation period (2010-2022), whereas the Amsterdam case study spanned 5 years (2020-2024). Although the Amsterdam analysis covers a shorter temporal window, it benefits from a richer and more diverse observational dataset, including direct flux measurements.

Even if coarse, the adopted resolution is sufficient to capture first-order spatial contrasts in LST driven by land cover composition. This is supported by previous remote-sensing studies over Milano, which consistently report higher summer LST over built-up areas relative to vegetated surfaces [**6.1**, **6.2**, **6.3**].

Independent observational studies have reported strong intra-urban thermal contrasts in Amsterdam, with surface temperatures in the historic city center exceeding those of adjacent water bodies by 9–10 °C [**6.4**]. The simulated LST patterns obtained in this study are consistent with these findings, lending further support to the validity of the modelling framework. Ongoing work within the 4TU.Heritage project [**6.5**, **6.6**, **6.7**] is expected to deliver higher-resolution and temporally dynamic estimates of anthropogenic heat fluxes, which could be integrated into future extensions of the $SWEB$ model.

By design, $SWEB$ represents a simplified one-dimensional scheme that accounts exclusively for vertical exchanges of energy and water. Consequently, small-scale processes such as urban canyon effects, radiative trapping, the sky view factor, and detailed building–atmosphere interactions [**6.8**] are not explicitly resolved. While these mechanisms are relevant at the microscale, the adopted spatial resolutions strike a deliberate balance between physical realism, spatial coverage, and computational feasibility. This compromise enables the investigation of extended temporal periods and large spatial domains, which is essential for long-term climate impact assessments and the integration of CMIP6 climate projections.

Some uncertainties and limitations remain in this research, the most evident ones being that (i) LST data, used for model tuning, may present some inaccuracies ($\pm$ 1°C) due to the influence of urban infrastructures, (ii) soil properties are taken here as constant, because only the urban surface and an active soil layer (W_{max}) were considered, without accounting for variations in depth, textures, etc.., (iii) anthropogenic heat fluxes are not directly measured, and for Milano (iv) longwave radiation is not considered, as only global radiation is taken into account, and (v) the temporal resolution is somewhat coarse to mimic daily thermal cycles.

There are uncertainties associated with satellite-derived LST. MODIS products, used for calibration over Milano, are subject to uncertainties of approximately $\pm$1 °C, exacerbated by urban surface heterogeneity and the coarse spatial resolution ($\sim$1 km). The temporal averaging further limits the representation of short-term thermal extremes. Higher-resolution sensors such as Landsat 8 ($\sim$31 m) offer improved spatial detail but suffer from limited temporal coverage and increased retrieval complexity, restricting their applicability for long-term analyses. These limitations highlight the necessity of combining remote sensing with in situ measurements, including flux towers and potentially citizen science observations, to enhance the reliability and contextual relevance of urban climate assessments.

Anthropogenic Heat Flux (AHF) constitutes a major source of uncertainty in urban energy balance modelling. In the Milano case study, anthropogenic heat release [**6.9**, **6.10**, **6.11**] and other fine-scale urban effects were not explicitly parameterized. This choice reflects both the large spatial extent of the study domain and the pronounced heterogeneity of the urban fabric, as well as the lack of spatially distributed and temporally resolved datasets describing anthropogenic heat emissions. Under these constraints, any direct parameterization of AHF

would have introduced additional uncertainty without a clear gain in model robustness. In contrast, the Amsterdam case study benefits from a smaller spatial extent and a more homogeneous urban structure, allowing for the inclusion of a constant AHF based on values reported in the literature and stratified according to the Local Climate Zone (LCZ) classification provided by the WUDAPT project [**6.12**]. Previous studies indicate that summertime anthropogenic heat contributions in Amsterdam typically remain below 20 W m^{-2} [**6.13**], rendering their influence secondary relative to radiative and turbulent fluxes. Under these conditions, the assumption of a constant AHF represents a reasonable approximation.

For Milano, model does not consider the diurnal variation of air temperature, air humidity, wind speed and gustiness, so not diurnal variation of LST and temporal evolution of atmospheric comfort for humans [**6.14**]. The model neglects lateral (advective) fluxes between adjacent grid cells, assuming that vertical exchanges dominate over horizontal ones at the adopted spatial resolutions (100–500 m). At these scales, radiative and turbulent vertical fluxes are expected to be significantly larger than horizontal advective contributions, justifying the assumption of no interaction between cells. Moreover, the objective of this study is not to develop a full urban climate model, but rather to estimate LST based on surface energy and water budgets. In this context, the exclusion of advective fluxes does not significantly affect model performance, as confirmed by the good agreement between simulated and observed LST. It is also important to note that advective heat and moisture transport are highly localized and transient processes, which are difficult to capture at the spatial and temporal scales considered here. Their inclusion would be more appropriate in high-resolution studies (e.g., CFD-based analyses) focusing on microscale urban processes.

Beyond its forward application, the model was also successfully employed in an inverse configuration, using observed LST to estimate near-surface air temperature (T_a). The resulting T_a fields show good agreement with measurements from automatic weather stations, confirming the internal consistency of the approach. As expected, spatial contrasts in T_a between green and built-up areas are systematically smaller than those observed for LST, reflecting the weaker coupling of air temperature to surface properties compared to the direct radiative and thermodynamic response of the surface itself.

During summer conditions, solar radiation emerges as the dominant driver of the surface energy balance. This behavior is clearly supported by flux tower observations in Amsterdam, while in Milano additional contributions must be

considered. In particular, higher traffic density and the widespread use of air-conditioning systems during heatwaves introduce non-negligible anthropogenic heat inputs, which are indirectly reflected in observed thermal patterns. These processes have also manifested at the urban scale through recurrent summer power outages caused by peak electricity demand, highlighting the strong coupling between urban climate, energy consumption, and infrastructure vulnerability.

The $SWEB$ model is not intended to replace high-resolution, computationally intensive tools such as ENVI-met [**6.15**, **6.16**], MeteoBlue [**6.17**, **6.18**], or TERRA-URB [**6.19**]. Rather, it serves as a complementary framework specifically suited to large-scale, long-term applications. Model stability and robustness were ensured through the use of multi-year daily and hourly forcing data, encompassing 724 grid cells over Milano and 763 grid cells over the Amsterdam city center. While not designed for microscale analyses, $SWEB$ effectively captures domain-wide thermal responses to variations in meteorological forcing and land-cover characteristics, including changes in vegetation fraction (VF or G_f).

Across both cities, precipitation and air temperature emerge as the primary drivers of LST variability in time: reduced precipitation and elevated air temperatures systematically lead to higher surface temperatures. Wind speed also modulates LST, though its influence is more complex and site-specific. In both Milano and central Amsterdam, wind speeds generally remain below 4 m s^{-1}, a regime in which a single soil resistance formulation is appropriate. Sensitivity analyses indicate that using temporally averaged wind speed improves agreement between simulated and observed LST, particularly in Amsterdam. At higher wind speeds, like Schiphol area, soil resistance becomes increasingly sensitive to wind variability, enhancing turbulent heat exchange and reducing surface temperatures [**6.20**].

The $SWEB$ model for Milano was also applied to simulate future scenarios. The model uses precipitation and air temperature projections from the GCMs CESM, CMCC, HADGEM, and MIROC, under the socio-economic pathways SSP1-2.6 and SSP5-8.5. In general, the assessment of LST patterns is largely based on remote-sensing data. However, relatively few studies have addressed future LST projections, and the evolution of LST under climate change scenarios remains insufficiently investigated. Existing research is mainly limited to linear regression approaches that relate land-use characteristics to LST variations under projected climate change conditions [**6.21**, **6.22**]. SUHI variation in Milano is influenced even to other factors, like groundwater table depth [**6.23**]. Anomalies up to +5 °C on the groundwater table are predicted by 2100. This $SWEB$ model,

under the worst-case scenario (SSP5–8.5) conditions, projects a LST increased by 3.98 °C, accompanied by a riduced difference between *Built-up* areas and *Green* areas' LST ($SUHII = +0.51$ °C).

Overall, the results highlight the central role of water availability in regulating urban thermal conditions. Future urban planning strategies should therefore explicitly integrate water-sensitive and nature-based solutions, including urban water bodies, decentralized micro-reservoirs, and vegetation with high transpiration capacity. While such interventions can substantially enhance urban cooling, their ecological, infrastructural, and governance implications must be carefully evaluated to ensure long-term sustainability in dense urban environments.

At the urban scale, the implementation of tree-based mitigation strategies is often constrained by limited soil volumes available for root development. In cities such as Milano, the urban form was not originally designed to accommodate large tree systems, as built surfaces frequently extend close to the ground, leaving minimal space for rooting. Indeed, alternative strategies should be considered, including the use of shallow-rooted plant species (e.g., 20–30 cm depth) adapted to local conditions, and the integration of blue infrastructures such as water bodies. However, the latter requires careful design and management, including expert assessment to mitigate potential issues such as insect proliferation.

Future developments of this research may follow these directions: (i) *finer resolution*, by increasing both spatial and temporal scales to better capture small-scale urban patterns and diurnal variability, particularly for Milan; (ii) *climate scenarios*, by exploring future LST conditions in Amsterdam based on IPCC projections; and (iii) *scenario analysis*, by assessing the model response to changes in urban configuration, such as the expansion of green and blue infrastructure and modifications of soil properties.

References

[**6.1**] L. Mariani, S.G. Parisi, G. Cola, R. Lafortezza, G. Colangelo, and G. Sanesi. "Science of the Total Environment Climatological analysis of the mitigating effect of vegetation on the urban heat island of Milan , Italy". In: *Science of the Total Environment, The* 569-570 (2016), pp. 762–773. DOI: 10.1016/j.scitotenv.2016.06.111.

[**6.2**] G. Frustaci, S. Pilati, C. Lavecchia, and E. Montoli. "High-Resolution Gridded Air Temperature Data for the Urban Environment: The Milan Data Set". In: *Forecasting* 4.1 (2022), pp. 238–261. DOI: 10.3390/forecast4010014.

[**6.3**] M. Puche, A. Vavassori, and M.A. Brovelli. "Insights into the Effect of Urban Morphology and Land Cover on Land Surface and Air Temperatures in the Metropolitan City of Milan (Italy) Using Satellite Imagery and In Situ Measurements". In: *Remote Sensing* 15.3 (2023). DOI: 10.3390/rs15030733.

[**6.4**] F. Van Der Hoeven and A. Wandl. "Amsterwarm: Mapping the landuse, health and energy-efficiency implications of the Amsterdam urban heat island". In: *Building Services Engineering Research and Technology* 36.1 (2015), pp. 67–88. DOI: 10.1177/0143624414541451.

[**6.5**] W. van der Meer, F. Zantinge, and G. J. Steeneveld. "Urban fluxes for free: Estimating urban turbulent surface fluxes from crowdsourced meteorological canyon layer observations". In: *City and Environment Interactions* 27.May (2025), p. 100201. DOI: 10.1016/j.cacint.2025.100201.

[**6.6**] A.D. Rocha, S. Vulova, M. Förster, B. Gioli, B. Matthews, C. Helfter, F. Meier, G. Steeneveld, J.F. Barlow, L. Järvi, N. Chrysoulakis, G. Nicolini, and B. Kleinschmit. "Unprivileged groups are less served by green cooling services in major European urban areas". In: *Nature Cities* 1.6 (2024), pp. 424–435. DOI: 10.1038/s44284-024-00077-x.

[**6.7**] X. Chen, J. Werf, A. Droste, and M. Coenders-gerrits. "Barriers of urban hydro-meteorological simulation : a review". In: *Hydrology and Earth System Sciences* 29.January (15 2025), pp. 3447–3480. DOI: 10.5194/hess-29-3447-2025.

[**6.8**] M. Nunez and T.R. Oke. "The Energy Balance of an Urban Canyon". In: *Journal of Applied Meteorology and Climatology* 16 (1977), pp. 11–19.

[**6.9**] A. Buyantuyev and J. Wu. "Urban heat islands and landscape heterogeneity: Linking spatiotemporal variations in surface temperatures to land-cover and socioeconomic patterns". In: *Landscape Ecology* 25.1 (2010), pp. 17–33. DOI: 10.1007/s10980-009-9402-4.

[**6.10**] Y. Liu, G. Shintaro, D. Zhuang, and W. Kuang. "Urban surface heat fluxes infrared remote sensing inversion and their relationship with land use types". In: *Journal of Geographical Sciences* 22.4 (2012), pp. 699–715. DOI: 10.1007/s11442-012-0957-7.

[**6.11**] C. Yuan, A.S. Adelia, S. Mei, W. He, X.X. Li, and L. Norford. "Mitigating intensity of urban heat island by better understanding on urban morphology and anthropogenic heat dispersion". In: *Building and Environment* 176.April (2020), p. 106876. DOI: 10.1016/j.buildenv.2020.106876.

[**6.12**] B. Bechtel, P.J. Alexander, C. Beck, J. Böhner, O. Brousse, J. Ching, M. Demuzere, C. Fonte, T. Gál, J. Hidalgo, P. Hoffmann, A. Middel, G. Mills, C. Ren, L. See, P. Sismanidis, M.L. Verdonck, G. Xu, and Y. Xu. "Generating WUDAPT Level 0 data – Current status of production and evaluation". In: *Urban Climate* 27 (2019), pp. 24–45. DOI: 10.1016/j.uclim.2018.10.001.

[**6.13**] G. Steeneveld, S. van der Horst, and B. Heusinkveld. "Observing the surface radiation and energy balance, carbon dioxide and methane fluxes over the city centre of Amsterdam". In: *EGU general assembly conference abstracts*. 2020, p. 1547.

[**6.14**] R.G. Steadman. "A universal scale of apparent temperature". In: *Journal of Applied Meteorology and Climatology* 23.12 (1984), pp. 1674–1687.

[**6.15**] M. Bruse. "ENVI-met 3.0: updated model overview". In: *University of Bochum. Retrieved from: www. envi-met. com* 3 (2004).

[**6.16**] Stella Tsoka, A Tsikaloudaki, and T Theodosiou. "Analyzing the ENVI-met microclimate model's performance and assessing cool materials and urban vegetation applications–A review". In: *Sustainable cities and society* 43 (2018), pp. 55–76.

[**6.17**] meteoblue. *meteoblue Climate Data Store*. https://content.meteoblue.com/en. Accessed: Nov 2025. 2025.

[**6.18**] N. Bader, N. Zurfluh, J. Shin, and S. Schlögl. *Enhance the meteoblue City Climate Model by Climate Projections to assess Urban Climate Hazard*. Tech. rep. Copernicus Meetings, 2024.

[**6.19**] D. Cinquegrana, M. Montesarchio, A.L. Zollo, and E. Bucchignani. "Evaluation of the Urban Canopy Scheme TERRA-URB in the ICON Model at Hectometric Scale over the Naples Metropolitan Area". In: *Atmosphere* 15.9 (2024). DOI: 10.3390/atmos15091119.

[**6.20**] Cang Tong, Xiangli Li, Lin Duanmu, and Haichao Wang. "Prediction of the temperature profiles for shallow ground in cold region and cold winter hot summer region of China". In: *Energy and Buildings* 242 (2021), p. 110946. DOI: 10.1016/j.enbuild.2021.110946.

[**6.21**] L. Tian, Y. Tao, M. Li, C. Qian, T. Li, Y. Wu, and F. Ren. "Prediction of Land Surface Temperature Considering Future Land Use Change Effects under Climate Change Scenarios in Nanjing City, China". In: *Remote Sensing* 15.11 (2023). DOI: 10.3390/rs15112914.

[**6.22**] B. Halder, J. Bandyopadhyay, and P. Banik. "Evaluation of the Climate Change Impact on Urban Heat Island Based on Land Surface Temperature and Geospatial Indicators". In: *International Journal of Environmental Research* 15.5 (2021), pp. 819–835. ISSN: 2008-2304. DOI: 10.1007/s41742-021-00356-8.

[**6.23**] A. Previati, L. Gallia, and G. Crosta. "Impact of urbanization and climate change on underground temperatures: a modelling study in Milan (Italy)". In: *Philosophical Transactions of the Royal Society A: Mathematical, Physical and Engineering Sciences* 383.2308 (Nov. 2025). DOI: 10.1098/rsta.2025.0038.

Chapter 7

Conclusion

This PhD thesis presents a proposed energy and water budget approach, exploited via the $SWEB$ model, used jointly with remote sensing and ground-based data for the assessment of Land Surface Temperature and the evaluation of the Surface Urban Heat Island effect in the cities of Milano (Italy) and Amsterdam (Netherlands), considering also the potential mitigation effects of green and blue spaces. The results confirm a linear relationship between LST and Green presence (G_f or VF), offering policy-makers valuable insights to increase green areas in urban settings as a strategy for mitigating Surface Urban Heat Island effect.

The physically based $SWEB$ model seems an effective tool for interpreting climatic data and soil characteristics, allowing an accurate enough assessment of seasonal mean LST. The spatial resolution (500 m $\times$ 500 m for Milano and 100 m x 100 m for Amsterdam) allows the analysis of long time series and the provision of meaningful average data, highlighting how increased vegetation cover can significantly reduce the mean LST in urban contexts.

By accurately identifying the warmest areas, the model provides crucial insights for addressing the challenges posed by climate change. This $SWEB$ model's versatility in quickly generating new outputs, by modifying climatic inputs or land use, makes it suitable for use in diverse urban settings. This study provides scientific evidence that green areas can sensibly reduce LST. For Milano, it was estimated that an increase of $\Delta VF = +10\%$ may correspond to a decrease of $\Delta LST = -0.23$°C. In Amsterdam, $Built-Up$ areas exhibit, on average, LST that are +1.72 °C higher than those observed over $Green$ areas and +4.21 °C higher than over $Water$ bodies, considering green and blue spaces located within the Singelgracht boundary. In $Water$-covered areas, the energy available from net radiation is predominantly converted into latent heat rather than sensible heat, thereby limiting the exchange of heat between the surface

and the overlying air. Latent heat refers to the energy consumed by evaporation processes, which occur over wet surfaces, such as water bodies by definition, and through vegetation transpiration, whereby a large fraction of the available net radiation is dissipated as latent heat rather than being converted into sensible heat, resulting in a reduced heat exchange between the surface and the atmosphere.

Especially during summer, LST differences between urban and rural areas become more pronounced. In the Amsterdam case study, LST values assessed at Schiphol Airport area are up to -4.5 °C lower than those recorded in the city centre. Similarly, the higher forested peripheral area of western Milano (Milano West) exhibits surface temperatures approximately 3.80 °C lower than the urban core (Milano Centre). Nevertheless, substantial and meaningful LST variations also occur within the urban fabric itself, highlighting the importance of assessing the actual cooling potential of urban blue–green spaces. This is particularly relevant given that truly rural conditions cannot be realistically replicated in dense urban environments.

It is important to account for heat waves, as pronounced increases in air temperature, especially when persisting over several consecutive days, lead to corresponding rises in LST . During the summers of 2012, 2015, and 2022 in Milano, mean LST values were about 4 °C higher than the average LST observed over the 2010–2022 period (i.e. 35 °C), with the most critical conditions occurring in fully urbanized areas. In Amsterdam, for instance, during the summer of 2022, mean daily LST values reached approximately 25 °C, representing an increase of about 1.7 °C compared to the 2020–2024 average. Moreover, T_a anomalies are strongly reflected in LST responses, with T_a anomalies of +15 °C corresponding to LST anomalies of up to +20 °C.

Milano future projections results indicate that future urban thermal conditions will be strongly modulated by climate-driven changes in water availability rather than temperature increases alone. Projections for the Milano metropolitan area reveal contrasting responses of LST and $SUHII$ under different climate scenarios: while the low-emission scenario (SSP1–2.6) suggests a reduction in LST despite persistently high $SUHII$, the high-emission scenario (SSP5–8.5) points to a substantial increase in LST accompanied by a weakened urban–rural thermal contrast. This counterintuitive behavior reflects the critical role of soil moisture and latent heat fluxes, as prolonged droughts and heatwaves reduce the cooling capacity of vegetated surfaces, causing them to thermally resemble built-up areas.

The findings consistently highlight water availability as a key control on urban surface temperatures. Enhanced precipitation and evapotranspiration lead

to lower LST values, whereas reduced rainfall limits latent heat fluxes and amplifies surface warming. Evidence from the Amsterdam case study further supports this conclusion, showing that urban water bodies can substantially mitigate local heating, with LST values around 4 °C lower than surrounding impervious surfaces. These results underscore the importance of integrating water-sensitive and nature-based solutions into future urban planning. Strategies that promote the retention and redistribution of precipitation, such as urban water bodies, decentralized micro-reservoirs, and irrigation-supporting infrastructures, can enhance the cooling efficiency of green areas. At the same time, urban greening should prioritize native and functionally appropriate vegetation with high transpiration capacity. However, the potential ecological and practical limitations of such interventions must be carefully considered to ensure their long-term sustainability and effectiveness within dense urban environments.

The Amsterdam case study suggests that the presence of water bodies can significantly reduce LST at the local scale. In the absence of sufficient water availability, natural soil tends to behave similarly to urban surfaces in terms of heat release, leading to an overall increase in LST.

7.0.1 Contribution to climate change and sustainable development solutions

Within the framework of European climate policies, the EU Mission "Climate-Neutral and Smart Cities", part of the European Green Deal, supports 102 cities in achieving climate neutrality by 2030, including Milano and Amsterdam. In this context, the present study investigates the urban climate of these two cities through the implementation of a physically based model to assess LST variability at the urban scale. The analysis further evaluates the mitigation potential of green and blue infrastructures, using Milan and Amsterdam as representative case studies. Although the Mission primarily focuses on the reduction of greenhouse gas emissions, it explicitly acknowledges the role of urban adaptation to the impacts of climate change. In this context, the phenomenon of the Surface Urban Heat Island (SUHI) represents one of the most significant impacts in urban areas, affecting human well-being, energy consumption, and public health. The actions promoted by the Mission cities, including the implementation of Nature-Based Solutions, the expansion of green surfaces, the regeneration of urban spaces, and the promotion of climate-resilient materials and infrastructures, directly contribute to the mitigation of SUHI. Therefore, reducing SUHI intensity can be considered a cross-cutting objective that supports the achievement of

urban climate neutrality as envisioned by the Mission.

Figure 7.1. Reference to the Sustainable Development Goals addressed in this study, with a focus on SDG 11 (Sustainable Cities and Communities) and SDG 13 (Climate Action) of the United Nations 2030 Agenda.

The aim of this research is to assess the mitigation effects generated by urban green areas. An increasing number of cities are adopting guidelines for the implementation of Nature-Based Solutions (NBS), such as Sustainable Urban Drainage Systems (SUDS), with the goal of fostering sustainability, enhancing environmental quality, and reducing the prevalence of impervious surfaces and gray infrastructures, which have expanded significantly as a result of rapid urbanization. This study does not seek to design new NBS or propose landscape-oriented solutions. Instead, it aims to evaluate, from an engineering perspective, the role of urban greenery and its capacity to mitigate the increase in LST driven by ongoing global warming. The proposed methodology relies on a combined water–energy model, which is particularly suited to providing a deeper understanding of complex energy-driven phenomena such as the Surface Urban Heat Island. In this regard, water–energy Nexus approaches are increasingly being recognized and applied.

These pieces of information seem useful in supporting policy makers in the development of targeted strategies for SUHI mitigation. Potential measures include the expansion and optimization of existing green infrastructure, the integration of urban water bodies and water-sensitive design solutions to enhance evaporative cooling, the adaptation of building regulations to improve energy efficiency and thermal performance, and the implementation of nature-based solutions tailored to local climatic and hydrological conditions.

List of Acronyms

- *ARPA* - Agenzia Regionale per la Protezione dell'Ambiente
- *AWS* - Automatic Weather Station
- *CMIP6* - Coupled Model Intercomparison Project Phase 6
- *GCM* - Global Circulation Model
- *GHG* - Greenhouse Gas
- *HW* - Heat Wave
- *INAF* - National Institute of Astrophysics
- *IPCC* - Intergovernmental Panel on Climate Change
- *KNMI* - Koninklijk Nederlands Meteorologisch Instituut
- *LCZ* - Local Climate Zone
- *LGN* - Landelijk Grondgebruik Nederland
- *PDOK* - Publieke Dienstverlening Op de Kaart
- *RCP* - Representative Concentration Pathway
- *SEB* - Surface Energy Balance
- *SSP* - Shared Socioeconomic Pathway
- *SUHI* - Surface Urban Heat Island
- *SWEB* - Surface Water Energy Balance
- *VF* - Vegetation Fraction
- *WMO* - World Meteorological Organization
- *WUDAPT* - World Urban Database and Access Portal Tools

List of Symbols

- α - Albedo
- β - Bowen ratio
- ε - Emissivity
- λ - Latent heat of vaporization
- ρ - Density
- θ - Soil moisture
- θ_{FC} - Field Capacity
- θ_{sat} - Maximum saturated soil moisture
- θ_{WP} - Wilting Point
- AHF - Anthropogenic Heat Flux
- B_f - Built-up fraction
- c - Specific heat
- C_H - Bulk exchange coefficient for sensible heat
- C_{LE} - Bulk exchange coefficient for latent heat
- ET - Actual Evapotranspiration
- G - Soil heat flux
- G_f - Green fraction (equivalent to VF)
- H - Sensible heat flux
- k - Soil permeability

- K - Saturated permeability
- LAI - Leaf Area Index
- LR - Liquid Rainfall term
- LST - Land Surface Temperature
- LW - Long Wave radiation
- P - Liquid Precipitation
- Q_g - Groundwater flow discharge
- Q_s - Sub-superficial flow discharge
- r_a - Aerodynamic resistance
- r_s - Surface resistance
- R_g - Global solar radiation
- R_n - Net radiation
- rs_{min} - Minimum stomatal resistance
- S - Energy storage
- $SUHII$ - Surface Urban Heat Island Intensity
- SW - Short Wave radiation
- T_a - Air Temperature assessed at 2 m above ground level
- v - Near-surface wind velocity
- VF - Vegetation Fraction (equivalent to G_f)
- W - Soil water storage
- W_f - Water fraction
- W_{max} - Max potential soil water storage
- w - Rainfall rate

Appendix

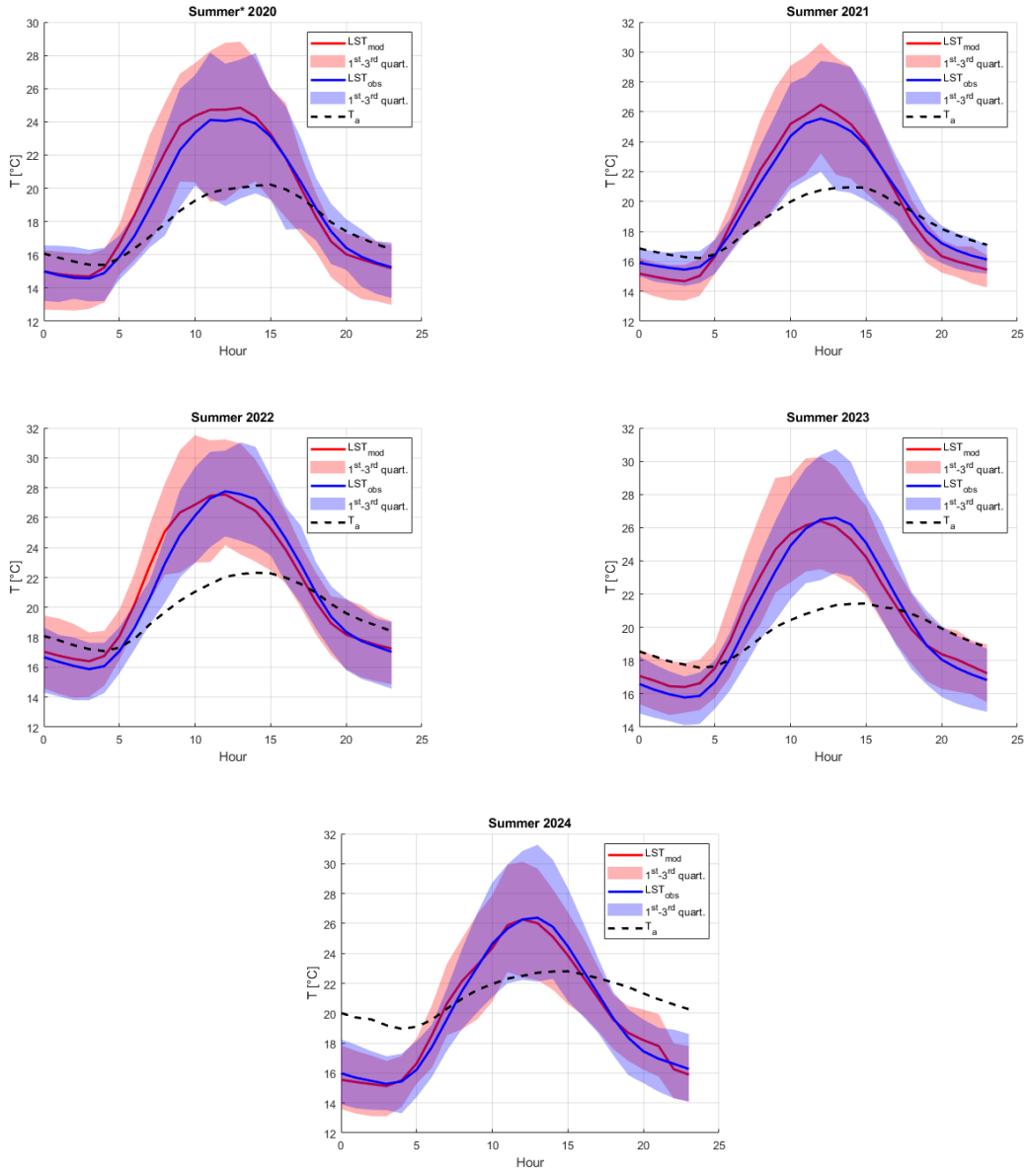

Figure 7.2. Mean hourly variation of modeled *LST* from the SWE balance model (***mod***) versus observed *LST* at FT (***obs***) during the summers of 2020–2024, including the respective 1st and 3rd quantiles, and compared with air temperature T_a. *Summer 2020 refers to June-July 2020

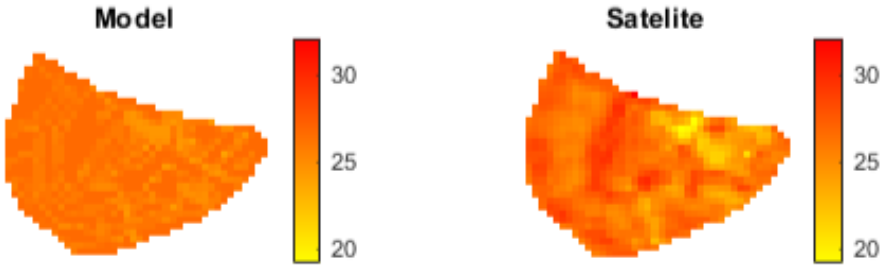

(a) 07/06/2021

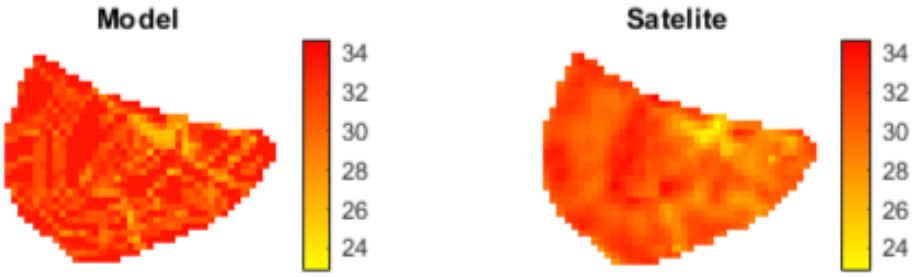

(b) 16/06/2021

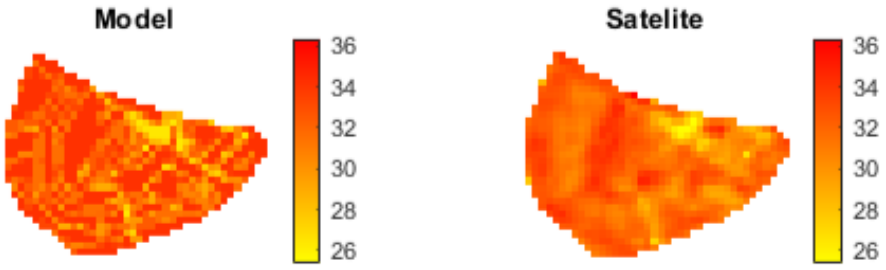

(c) 13/08/2022

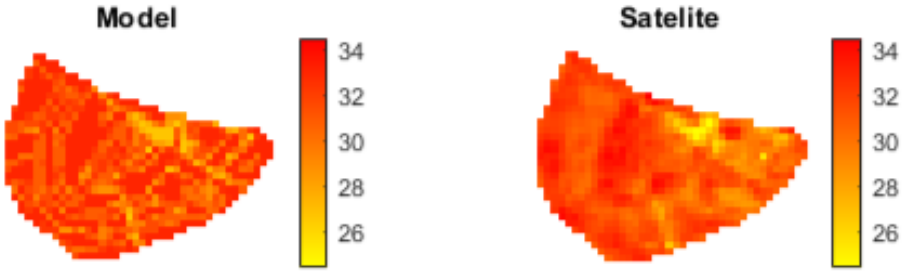

(d) 14/08/2022

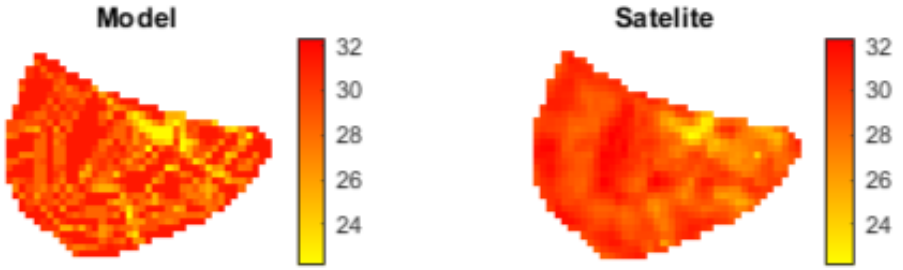

(e) 16/07/2023

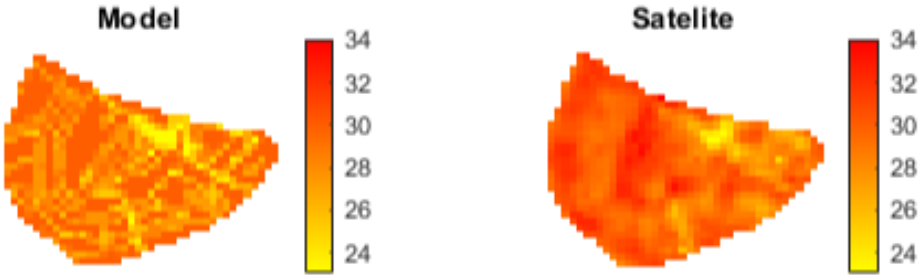

(f) 07/07/2023

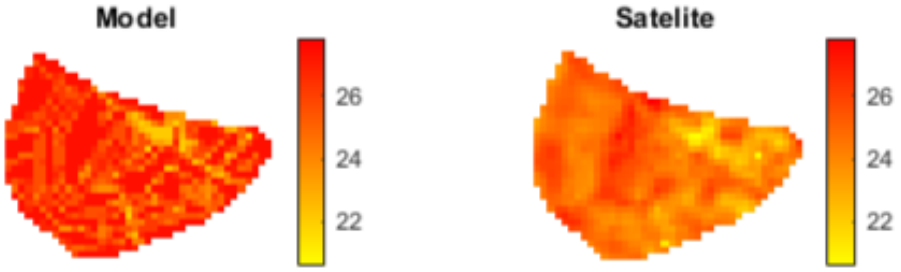

(g) 10/08/2024

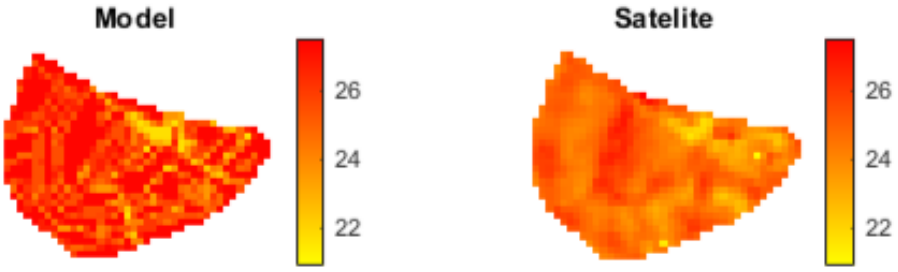

(h) 19/08/2024

Figure 7.3. Comparison of LST[°C] maps for Amsterdam: Surface Water-Energy balance model outputs *"Model"* versus Landsat-8 satellite observations *"Satellite"* for the available dates.

List of Figures

List of Tables